2022

Rational Design of Metal-Organic Frameworks (MOFs)-based Functional Materials Towards Better Air Quality

Zan Zhu
Virgnia Commonwealth University

Rational Design of Metal-Organic Frameworks (MOFs)-based Functional Materials Towards Better Air Quality

A dissertation submitted in partial fulfillment of the requirements for the degree of Doctor of Philosophy at Virginia Commonwealth University

By

Zan Zhu

M.S., Optical Engineering, Beijing University of Technology, China, 2016

B.S., Material Science, Huazhong University Science and Technology, China, 2013

Advisor: Wei-Ning Wang

Associate Professor, Department of Mechanical and Nuclear Engineering

Virginia Commonwealth University

Richmond, Virginia

May 2022

Acknowledgment

Firstly, I would like to express my deepest gratitude to my supervisor, Prof. Wei-Ning Wang, who has always provided me with constructing advice, continued support, and kind help during my Ph.D. study. Prof. Wang not only teaches me the knowledge of academic research but also shares valuable life experiences with me. His professionalism, positive attitude and motivation, self-discipline, and enthusiasm profoundly affected me, which helped me become a better version of myself. I also really appreciate Prof. Wang's wife and family, who make me not so helpless in a foreign country. Without you, I would not be where I am today.

My sincere thanks also go to my dissertation committee members: Prof. Sheng-Chieh Chen, Prof. Ravi Hadimani, Prof. Ram Gupta, and Prof. Ping Xu. My Ph.D. program will not go smoothly without your expertise, insightful comments, and guidance. I also want to thank Prof. Dmitry Pestov and Prof. Carl Mayer for their technical support in material characterization in the VCU facility center. I also thank my graduate program director Prof. Karla Mossi for her continued help and support.

I would also like to thank Dr. Xiang He and his wife, Xianghua Jin, who helped me in my research and life during my Ph.D. study. I also want to thank Hao Tu, Jianping Chen, Yu Zhang, Yuanhang Yang, Jie Zhang, Dr. Peng Wang, Hao Chen, Xiaofei Li, Chenchao Fang, Jingtao You, Mingyao Mou, Dr. Liang Bao, Dr. Junlin Ren, Dr. Xiao Han, Dr. Dawei Wang, and Prof. Shun Duan. Talking to you guys relieved my pressure over the past few years.

Lastly, I am deeply thankful to my beloved girlfriend, Yixing Zheng, my father, Huaiyu Zhu, and my mother, Zhuanghua Zuo, for being with me throughout. Your love, support, understanding, and encouragement are always invaluable treasures in my life.

Tables of Contents

List of Figures

List of Schemes

List of Tables

Abstract

RATIONAL DESIGN OF METAL-ORGANIC FRAMEWORK (MOF)-BASED FUNCTIONAL MATERIALS TOWARDS BETTER AIR QUALITY

By Zan Zhu

A dissertation submitted in partial fulfillment of the requirements for the degree of Doctor of Philosophy at Virginia Commonwealth University

Virginia Commonwealth University, 2022

Advisor: Dr. Wei-Ning Wang

Associate Professor, Department of Mechanical and Nuclear Engineering

Air pollution is a major threat to environmental safety and public health. Volatile organic compounds (VOCs), particulate matter (PM), and airborne microorganisms are three typical air pollutants. Conventional strategies to prevent and mitigate air pollution have been employed, which, however, are generally passive. For instance, VOC sensing through solid-state devices is a conventional approach, which, however, is not capable of capturing and removing VOCs. On the other hand, air filters and face masks are useful equipment to protect people from inhaling PM and airborne microorganisms. But most commercial filters can only capture them on the surfaces, which may cause secondary contamination under high airflow rates. This is particularly true for airborne pathogens, such as bacteria, fungi, and viruses, which can survive on the filter

surface for hours or even days, creating a potential risk of biosafety issues. Therefore, it is highly desired to develop advanced materials to solve the above air issues actively.

Metal-organic frameworks (MOFs), a novel porous crystalline material, have received considerable attention over the past decades because of their exceptional physical and chemical properties, including high porosity, huge specific surface area, structure robustness, and chemistry flexibility and diversity. These intriguing properties make MOFs an excellent candidate to combat the above air contamination. Numerous attempts have been reported to improve the performance of MOFs. However, the challenges remain in MOF design and its applications because of the complex interactions between MOFs and target pollutants.

The objective of this dissertation is to rationally design MOFs-based functional materials for efficient air quality control. This dissertation also aims to explore the quantitative interactions between the target air pollutants and the MOF-based materials by using advanced instruments, which generate new knowledge and understanding for future materials designed for better air quality. The dissertation is divided into two major parts: VOC (H_2S as a model) detection and airborne bacterial inactivation. In Chapters 2 and 3, a novel bimetallic MOF (*i.e.*, Al/Fe-MIL-53-NH_2) was developed to significantly improve its sensing performance towards a representative VOC of H_2S molecules based on the fluorescence "turn-on" effect. Beyond the improved performance of MOF-based materials, fundamental understandings of interactions between H_2S and MOF-based materials were also discussed. More specifically, the mechanisms of H_2S detection were successfully unraveled, where nitro-MOFs (e.g., Al-MIL-53-NO_2) were used to achieve quantitative fluorescence sensing. The new insights based on the investigations in this dissertation are completely different from what has been reported in previous studies. The results

showed that it is the free BDC-NH_2 (2-aminobenzene-1,4-dicarboxylic acid) in the solution rather than the formation of Al-MIL-53-NH_2 that caused the fluorescence enhancement.

In Chapters 4 and 5, novel antimicrobial materials have been designed by coating a quaternary ammonium compound (QAC) polymer, that is poly[2-(dimethyl decyl ammonium) ethyl methacrylate] (PQDMAEMA), onto the surface of various MOF-based materials (*e.g.*, UiO-66-NH_2 (zirconium-based), g-C_3N_4/MIL-125-NH_2 (titanium-based)) to form active composites for airborne bacterial inactivation. These rationally designed MOF composites demonstrated great antibacterial activities where electrostatic contact-killing and photogenerated reactive oxygen species (ROS) are utilized for efficient disinfection. In-depth investigations on the biointerface were carried out with several advanced techniques, such as the Zeta-potential analyzer, fluorescence laser confocal microscope (CLSM), and atomic force microscope (AFM). The results showed that the adhesion of bacterial cells towards the photocatalyst surface leads to significantly enhanced photocatalytic bactericidal efficiencies.

The work from this dissertation is expected to broaden the applications of MOF-based materials and advance the understanding of the interactions between MOFs and pollutants from the molecular level, which should have a significant impact on the rational design of MOF-based materials for air quality control and improvement.

Chapter 1. Introduction

1.1 Air Pollutants and Current Strategies

Air is the most critical supply for the vast majority of living species on the planet, and air quality directly affects human health.[1-5] The industrial revolution was indeed a great success in terms of technology, society, and the distribution of numerous services, but it also contributed to a significant increase in air pollution that poses a threat to human health.[6, 7] The American Health Effects Institute has reported that air pollution was the fifth leading risk factor for mortality worldwide in 2019.[8] There are approximately 9 million deaths worldwide every year due to anthropogenic air pollution, making it one of the most significant public health risks in the world.[6, 7]

Air pollution has various health effects. Individuals who are particularly susceptible to air pollution can suffer adverse health effects even on days with low levels of air pollution.[9] The short-term effects of air pollution include Chronic Obstructive Pulmonary Disease (COPD), coughing, shortness of breath, wheezing, asthma, respiratory disease, and an increased rate of hospitalizations (a sign of morbidity).[10] Among the long-term health effects of air pollution are chronic disease, pulmonary insufficiency, cardiovascular disease, and cardiovascular mortality.[11] For instance, a Swedish cohort study has found that long-term exposure to air pollution increases the risk of diabetes.[12] Furthermore, air pollution leads to a wide range of potentially harmful health effects in early human development, including respiratory, cardiovascular, mental, and perinatal conditions, which may result in infant mortality or chronic disease in adulthood.[13]

This dissertation mainly investigates three typical air pollutants: volatile organic compounds (VOCs), particulate matter (PM), and airborne microorganisms. These air pollutants can result in environmental contamination, adverse health effects, and even detrimental consequences. In section 1.1, details of VOCs, PM, and airborne microorganisms will be firstly

reviewed. Then, the current strategies to address the above air pollutants and their limitations will also be discussed.

1.1.1 Volatile Organic Compounds (VOCs)

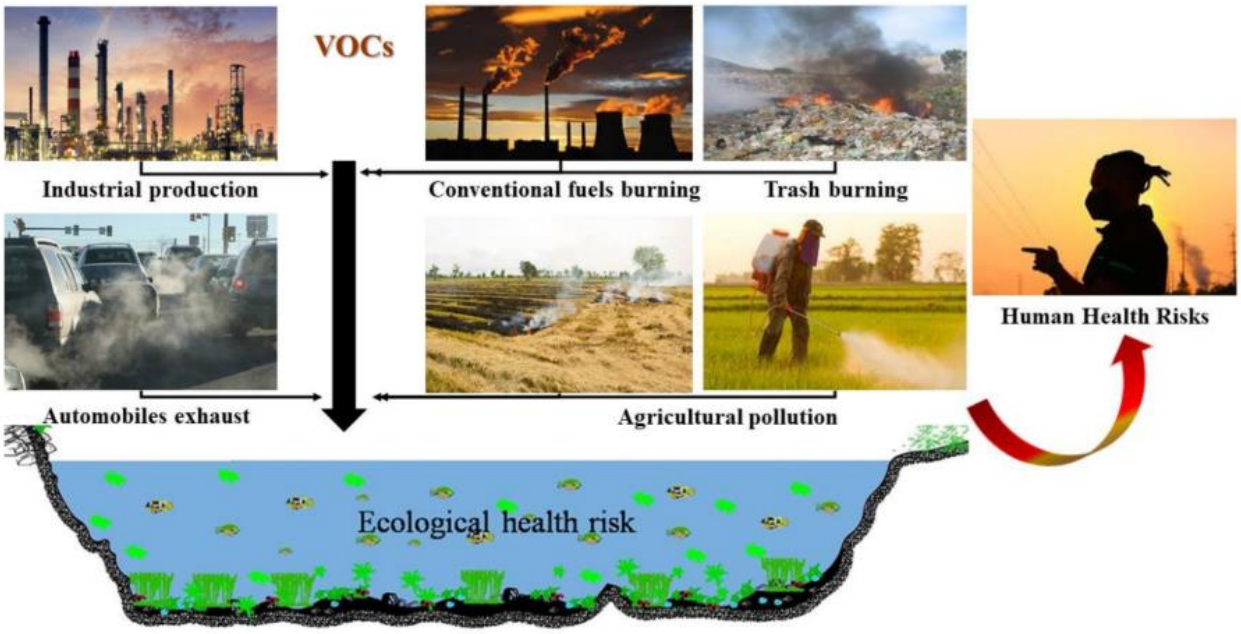

Figure 1.1 Sources of VOC occurrence. Reproduced from Ref.[14] with permission from MDPI.

VOCs are organic chemical compounds found in a wide variety of products that, under normal circumstances, evaporate readily and render themselves a hazard to the environment.[14] These VOCs can be generated either generated naturally or anthropogenically. Natural sources comprise VOC emissions from plants, forest fires occurring from natural causes, and anaerobic moors processes.[15, 16] A significant number of VOCs are produced by anthropogenic activities, including those of domestic and industrial use: agriculture, the use of fertilizers, pesticides, sewage treatment, chlorination, traffic, the burning of hydrocarbon fuels, the storage and distribution of petroleum, textile cleaning, printing, pharmaceuticals, etc. (see **Figure 1.1**).[14] The most common VOCs include benzene, toluene, hydrogen sulfide, formaldehyde, and polycyclic

aromatic hydrocarbons.[8] In the International Agency for Research on Cancer (IARC) classification system, several VOCs are considered to be known carcinogens (Group 1), including benzene, formaldehyde, and partial polycyclic aromatic hydrocarbons.[17-19] Hydrogen sulfide (H_2S), known as the odor of rotten eggs, is another characteristic VOC toxic gas. H_2S may have adverse health effects depending on how much H_2S is breathed in and how long it is breathed. It is possible to suffer eye and respiratory irritation under conditions of acute exposure at concentrations below 50 parts per million (ppm); however, exposure at or above 500 ppm is lethal.[20] A wide range of symptoms can be observed, from mild headaches and eye irritation to severe ones, including unconsciousness and death.[20] Therefore, it is crucial to reduce and avoid exposure to the VOCs.

Typical treatment methods to combat VOCs include physical/chemical adsorption, catalytic degradation, bioremediation, and thermal oxidation.[8, 21-24] All these emerging advanced strategies are developed to reduce the concentrations of VOCs. But it is more important to be aware of when the VOC adsorption is necessary.[8] Thus, the detection of VOCs has become an increasingly important area for chemical sensors.[25-27] Over the past few decades, numerous VOC sensors and detection materials have been developed and employed.[28-30] These sensors are mainly based on semiconducting metal-oxide, electrochemical, optical, and sensor arrays.[31-33] Although they can achieve good detectability and rapid response times, limitations and challenges still exist in performance on sensitivity and selectively. This is particularly true when the surrounding VOC concentration is at a low level, which is mainly due to the poor understanding of the interactions between materials and target VOC molecules.[34] Therefore, to develop a high-performance VOC sensor operated under the low-concentration VOC

environment, rational design of materials regarding the fundamental interactions between materials and target VOC gas must be considered from the molecular or the atomic level.

1.1.2 Particulate Matter (PM)

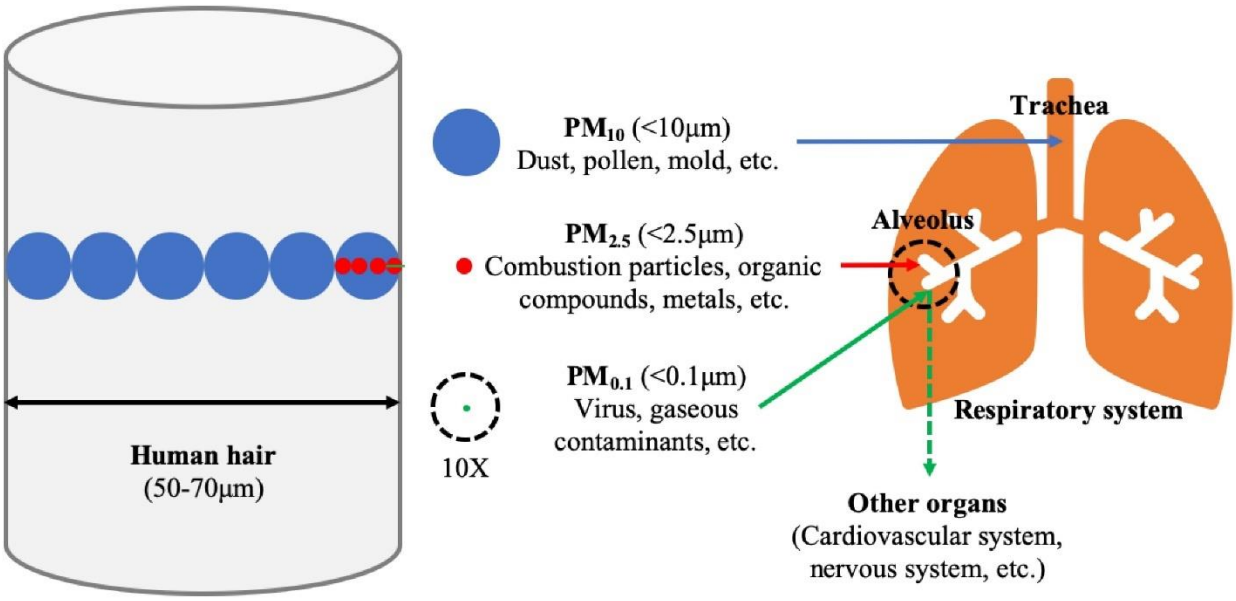

Figure 1.2 The size, main composition, and deposition site in the lung of the PM. Reproduced from Ref.[35] with permission from Frontiers Media.

PM is a mixture of solid particles and liquid droplets found in the air. PM usually originates from industrial pollution, vehicular emissions, soil dust, coal combustion, and biomass burning.[36-40] Traditionally, PM has been classified based on its size or aerodynamic diameter, with PM10, PM2.5, and PM0.1 usually referring to materials smaller than 10 mm, 2.5 mm, and 0.1 mm respectively, as shown in **Figure 1.2**.[41-47] PM, especially PM2.5, has a devastating impact on human health, particularly when it penetrates the human lungs and bronchi; the negative effect of PM on health increases with decreasing PM size.[41-47] Numerous studies have linked PM pollution exposure to a variety of problems, including premature death in people with heart or lung disease, nonfatal heart attacks, irregular heartbeat, aggravated asthma, decreased

lung function, and increased respiratory symptoms, such as irritation of airways, coughing or difficulty breathing. [41-44]

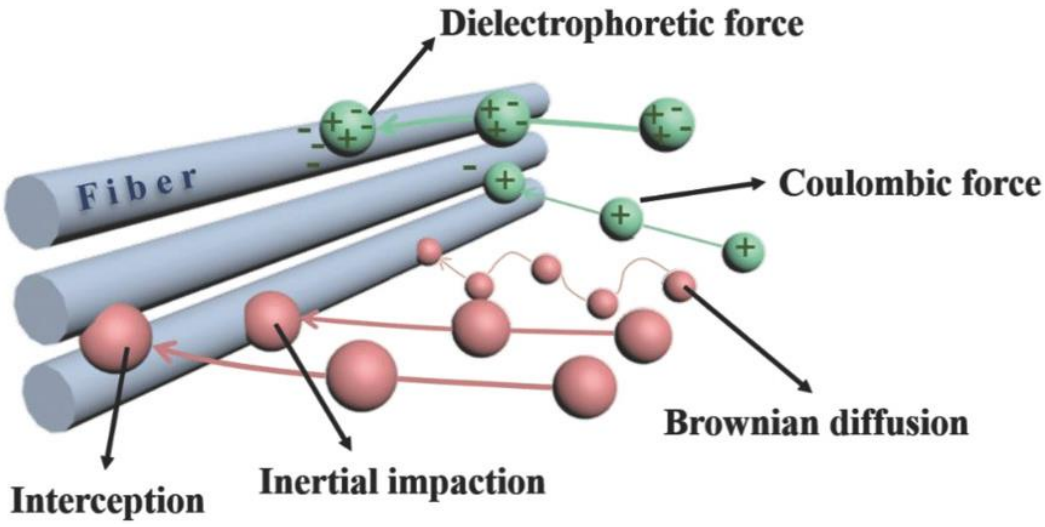

Figure 1.3 The mechanism of PM capture. Reproduced from Ref.[48] with permission from Wiley-VCH.

Source control and air filtration are two effective strategies to combat PM. Source control requires a great deal of time to understand the mechanism of PM formation and sophisticated control over the emission of PM.[48] Air purification is more efficient and timelier in controlling and improving air quality.[48-50] Typically, two types of filtration materials are used: porous membranes and fibrous filters.[48, 51] Porous membranes are usually fabricated by creating pores in solid substrates with good mechanical properties. Large pore-sized membranes can generally intercept larger particles, but these are often ineffective for smaller particles, such as PM2.5.

It should be noted that although the filtration efficiency of the membrane is satisfactory toward large particles, the pressure drop across the membrane is exceptionally high due to its low porosity (<30%).[51] On the other hand, fibrous filters can capture PM via physical barriers and surface adhesion.[52] Usually, these materials are constructed using multiple layers to enhance

their filtration efficiency. Most traditional air filters are fabricated to block the PM particles passively. The PM capture by these conventional air filters is governed by the well-known "single fiber" theory, where inertial impaction, interception, Brownian motion, and gravitational settling play a combined role in trapping these particles, as shown in **Figure 1.3**.[48] The main disadvantage of these materials is their compromise between air-pressure drop and filtration efficiency.[53] For air filter devices such as face masks, respirators, and purifiers, the pressure drop is directly related to the wearer's conform and energy consumption.[54-57] It is always desired to develop high-performance air filter materials and devices with lower pressure drops. Therefore, PM must be captured more proactively. Several proactive strategies have been reported to enhance air filtration performance, such as introducing chemical and electrical forces (see **Figure 1.3**).[58] Continuous efforts in rational design and development of advanced air filter materials and devices are still in high demand.

1.1.3 Airborne Microorganisms

Airborne microorganisms are unique components of PM that are widespread in bio-contaminated air.[59] Typical infectious airborne microorganisms include bacteria, viruses, and fungi. Inhalation of these airborne microorganisms can cause various adverse health effects on the human body, such as gastroenteritis, abdominal cramps, diarrhea, vomiting, septicemia, endocarditis, meningitis, osteomyelitis, asthma, chronic bronchitis, and decreased lung function.[60-63] Typical transmission routes of airborne pathogenic microorganisms are demonstrated in **Figure 1.4**, which include (i) outdoor airborne pathogenic microorganisms that are introduced through ventilation;[64] (ii) infected individuals' breathing, talking, coughing, or sneezing;[65] and (iii) contaminated surfaces.[66, 67]

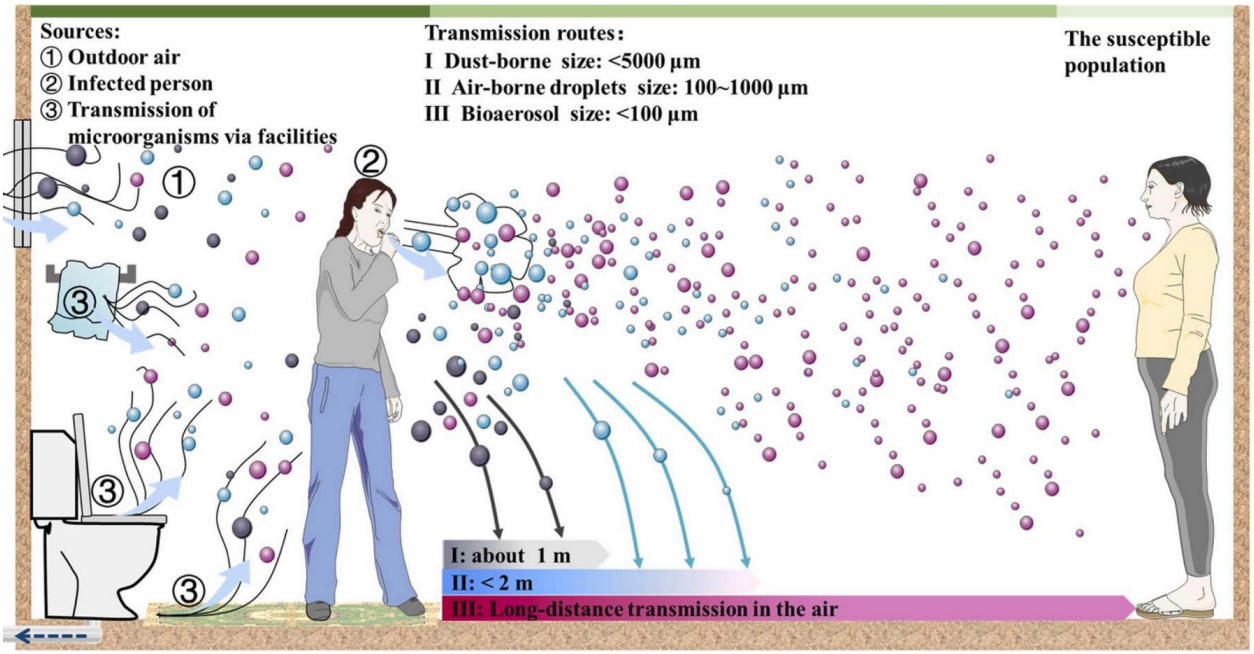

Figure 1.4 Schematic diagram of indoor airborne transmission of pathogenic microorganisms. Reproduced from Ref.[68] with permission from Elsevier.

Like PM prevention strategies, wearing face masks, respirators, and installing heating, ventilating, and air condition (HVAC) air filters are major approaches to protect people from airborne microorganisms. However, these methods are passive because most commercial air filters can only block the transmission of airborne microorganisms but not be able to kill them *in-situ*, i.e., on the mask surface. Certain microorganisms being captured by air filters can still survive for hours and even days, significantly increasing the possibility of secondary infection through surface contact transmission.[69, 70] Therefore, there is an urgent demand to develop antimicrobial air filters to kill airborne microorganisms actively.

1.2 Fundamentals of Metal-Organic Frameworks (MOFs)

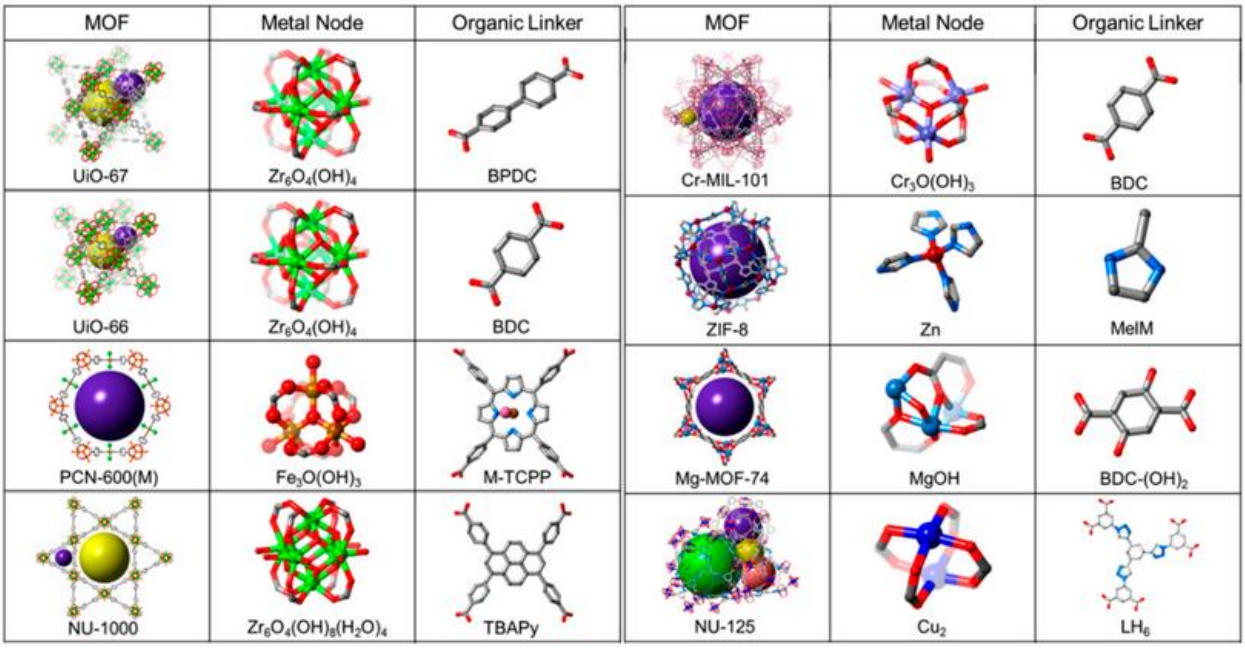

Figure 1.5 Representations of MOF structures and the corresponding node and linker constituents. Reproduced from Ref.[71] with permission from the American Chemistry Society.

MOFs are a class of highly porous crystalline materials, which are constructed by metal nodes (metal ions or clusters) and organic linkers.[72-75] By altering MOF connection or changing the metals and ligands species, almost unlimited MOFs can be designed.[76, 77] Over the past few decades, MOF structures have increased dramatically. According to the Cambridge Crystallographic Data Centre (CCDC), over 70000 new MOFs have been designed by 2016.[77] Some representative MOF structures and the corresponding metal modes and organic linkers are listed in **Figure 1.5**.

The reasons MOFs have attracted significant attention and emerged as one of the fascinating advanced materials for both academia and industry are their intriguing properties. Firstly, MOFs have a huge specific surface area and pore volume, making them initially widely used in gas-related applications, such as gas adsorption, gas filtration, and separation. DUT-49

(Dresden University of Technology) MOF, constructed by a carbazole derived and metallic ions of copper, were prepared by Stoeck *et al*.[78] Because of its extremely large specific surface area of 5476 m^2g^{-1} and pore volume of 2.91 cm^3g^{-1}, DUT-49 shows exceptionally high excess methane storage capacity of 308 mg g^{-1} (298 K, 110 bar). Zhang *et al*. coated a series of MOFs, including MIL-125-NH_2, UiO-66-NH_2, and ZIF-67, onto the commercial air filters to form MOFilters. All these MOFilters showed satisfactory adsorption performance towards the characteristic VOC molecules of toluene. Remarkably, the MIL-125-NH_2 filter offers the highest toluene removal efficiency of >80% at the face velocity of 5 cm s^{-1} because of its large surface area and polar interactions between toluene molecules.[79]

MOFs can be easily tailored in both composition and structure by adjusting the well-designed organic and inorganic building blocks and changing the synthetic conditions. Their properties can also be altered to display large surface area and porosity, high intensity, and desirable chemical activity.[80] For instance, the gas sorption capacity, selectivity, and isosteric heat of adsorption can be tuned by incorporating a second metal ion in the parent MOFs.[81] A series of bimetallic MOFs, including Cu-TMA(Fe), Cu-TMA(Co), Cu-TMA(Mg), Cu-TMA(Al), and Cu-TPA(Fe) (TMA: trimesic acid; TPA: terephthalic acid), were prepared with the assistance of microdroplet-based spray by He. *et al.*[81] The results showed that metal sites with larger electronegativity have a higher impact on the properties of the adsorbed CO_2, such as C=O bond length and O=C=O bond angle, leading to more asymmetric geometry and polarization of the adsorbed CO_2 molecules.[81]

Beyond modification within the MOF structures, MOFs can serve as an excellent platform to combine with other active species to form MOF composites, which endorse MOFs with additional functions and enhanced performance. For example, Zhang *et al.* coated a layer of

polydimethylsiloxane (PDMS) on the surface of MOF materials (*e.g.*, MOF-5, HKUST-1) to form the MOF/PDMS composites by a facile vapor deposition technique. The coated PDMS significantly changed the parent MOFs from hydrophilic to hydrophobic without sacrificing surface area, thus enhancing their moisture or water resistance.[82]

1.3 MOF-based Materials for Air Quality Control and Improvement

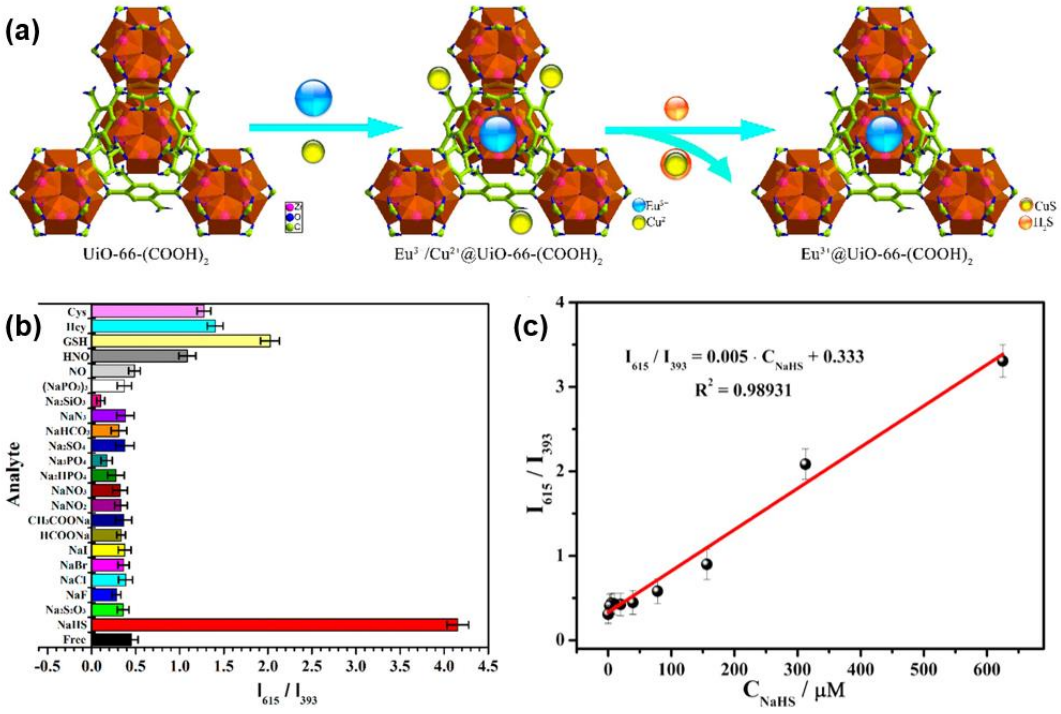

Figure 1.6 (a) Synthetic scheme of representative the crystalline structure of UiO-66-$(COOH)_2$, Eu^{3+}/Cu^{2+}@UiO-66-$(COOH)_2$, and Eu^{3+}@UiO-66-$(COOH)_2$; (b) Ratios of fluorescence intensity (I_{615}/I_{393}) of Eu^{3+}/Cu^{2+}@UiO-66-$(COOH)_2$ toward various analytes (5 mM) after 30 s of analyte addition; (c) Concentration dependence of the fluorescence intensity ratio (I_{615}/I_{393}). Reproduced from Ref.[30] with permission from the American Chemistry Society.

As reviewed in section 1.2, MOFs have unique and intriguing properties such as large specific surface area, adjustable pore size, ordered microporous structure, diverse pore size, and framework structure. Furthermore, functionalization inside, outside, at, and around MOFs is always possible when cautious during the modification, which significantly enriches the diversity

of MOFs. These excellent properties make MOF materials an extremely competitive candidate to address air pollution issues in Section 1.1, including VOC sensing, PM removal, and airborne microorganism inactivation.

The sensing of H_2S is a long-time challenging work. A fluorescence "turn-on" strategy is usually used to achieve quantitative H_2S detection, where fluorescence enhancements were observed upon contact with H_2S.[83] Zhang *et al*. developed a nano MOF UiO-66-$(COOH)_2$ modified with Eu^{3+} and Cu^{2+} ions (see **Figure 1.6a**). The nano MOF Eu^{3+}/Cu^{2+}@UiO-66-$(COOH)_2$ displays the characteristic Eu^{3+} sharp emissions and the broad ligand-centered (LC) emission simultaneously. Because H_2S can enormously increase the fluorescence of Eu^{3+} and quench the overall LC emission through its superior affinity for Cu^{2+} ions, the MOF Eu^{3+}/Cu^{2+}@UiO-66-$(COOH)_2$ exhibits highly sensitive turn-on sensing of H_2S over other environmentally and biologically relevant species under physiological conditions (see **Figure 1.6b and c**). Similar fluorescence "turn-on" effects were also observed on the nitro-functionalized MOF sensors. The electron-withdrawing $–NO_2$ groups in the initial non-luminescent MOFs were reduced to electron-donating $–NH_2$ groups in the sensing process. Several groups have reported that such nitro-MOFs are Al-MIL-NO_2, UiO-66-NO_2, and UiO-66-$(NO_2)_2$.[28, 84, 85]

MOFs have also been widely reported to remove PM and airborne microorganisms. Bian *et al*. used the electrospinning technique to fabricate MOF-based nanofibrous filters, which shows a high filtration efficiency of PM, especially for the particle size down to 15 nm.[36] As shown in **Figure 1.7(a-f)**, the ZIF-67 nanocrystals were distributed uniformly in the polyacrylonitrile (PAN) nanofibers.[36] The as-synthesized MOF/PAN filters can achieve PM filtration efficiency of 99.1% but with one-sixth of the pressure drop compared to the

commercial air filters. The significantly improved PM filtration performance is caused by the ZIF-67 nanocrystals with active surfaces, leading to the enhanced effects of Brownian diffusion and electrostatic interaction.[36]

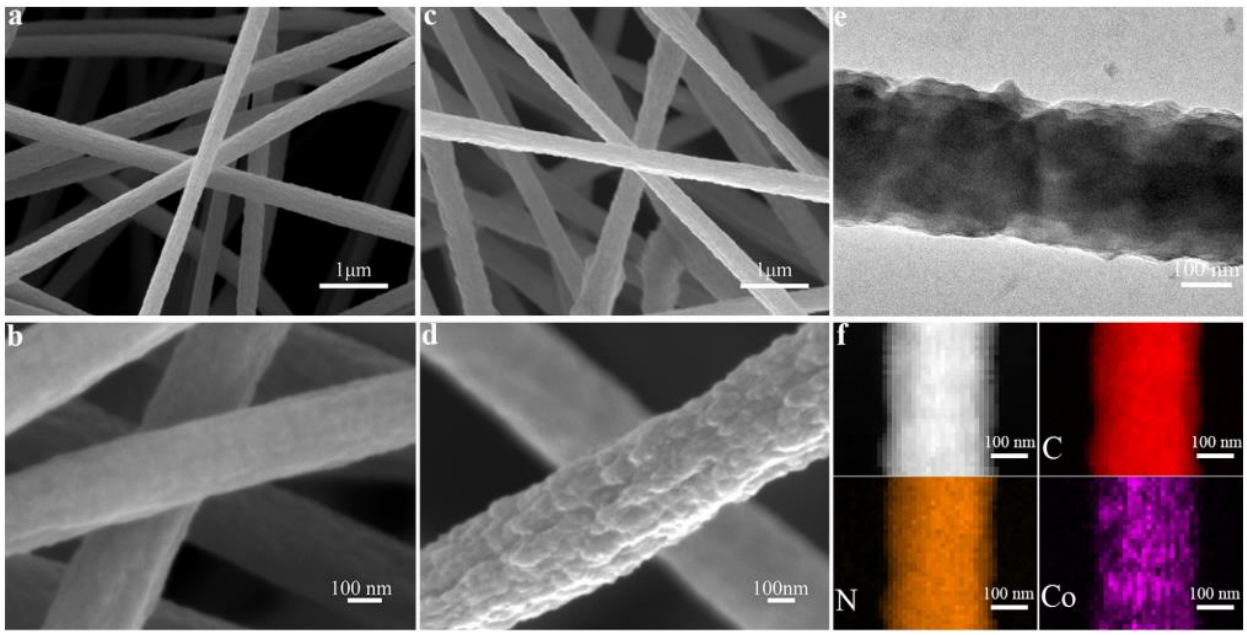

Figure 1.7 Microscopic images of nanofiber filters: (a-b) Pure PAN filter. (c-d) ZIF-67@PAN filter. (e) Bright-field TEM images of ZIF-67@PAN filter. (f) TEM-EDS elemental mapping of ZIF-67@PAN filter. Reproduced from Ref.[36] with permission from Elsevier.

Furthermore, a series of MOFs, including ZIF-8, ZIF-11, MIL-100(Fe), MIL-125-NH_2 (Ti), and UiO-66-NH_2(Zr), has been coated on the commercial air filters (*e.g.*, N95 respirator) to disinfect the airborne pathogenic bacteria *E. coli*, as shown in **Figure 1.8**.[1] Due to the photocatalytic properties of MOFs, O_2 could be readily activated by photoinduced Zn^+ intermediate catalytic centers within porous MOF to produce $\bullet O_2^-$ via electron transfer. The formed reactive oxygen species (ROS) like $\bullet O_2^-$ and H_2O_2 are detrimental to bacterial cells. Notably, the air filters made from ZIF-8 showed remarkable performance for PM filtration and

bacterial disinfection, with 97% PM removal efficiency and >99.99% photocatalytic killing efficiency against airborne bacteria in 30 min.[1]

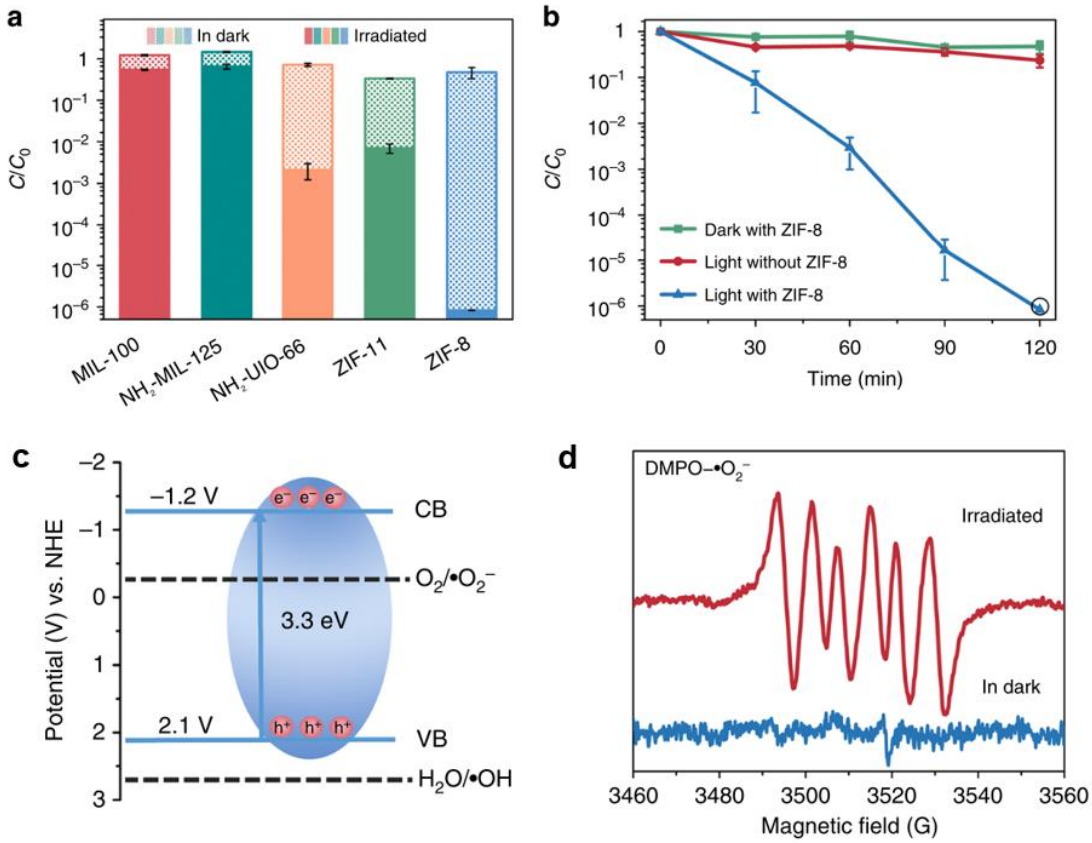

Figure 1.8 Photocatalytic disinfection of MOFs. (a) Disinfection performance of various MOFs; (b) Disinfection kinetics of ZIF-8 towards *E. coli*; (c) Band-structure analysis of ZIF-8; (d) Electron paramagnetic resonance (EPR) spectra O_2−. Reproduced from Ref. [1] with permission from Springer Nature.

1.4 Objectives and Arrangement of the Dissertation

Numerous attempts have been reported to improve the performance of MOFs and MOF-based materials to address air quality issues. However, the challenges remain in MOF design and its applications because of the complex interactions between MOFs and target pollutants. This dissertation aims to design MOFs-based functional materials for efficient air quality control rationally. This dissertation also aims to explore the quantitative interactions between the target

air pollutants and the MOF-based materials by using advanced instruments, which generate new knowledge and understanding for future materials designed for better air quality. The dissertation is divided into two major parts: VOC (H_2S as a model) detection and airborne bacterial inactivation. In Chapters 2 and 3, a novel bimetallic MOF (*i.e.*, Al/Fe-MIL-53-NH_2) was developed to significantly improve its sensing performance towards a representative VOC of H_2S molecules based on the fluorescence "turn-on" effect. Beyond the improved performance of MOF-based materials, fundamental understandings of interactions between H_2S and MOF-based materials were also discussed. More specifically, the mechanisms of H_2S detection were successfully unraveled, where nitro-MOFs (e.g., Al-MIL-53-NO_2) were used to achieve quantitative fluorescence sensing. The new insights based on the investigations in this dissertation are completely different from what has been reported in previous studies. The results showed that it is the free BDC-NH_2 (2-aminobenzene-1,4-dicarboxylic acid) in the solution rather than the formation of Al-MIL-53-NH_2 that caused the fluorescence enhancement.

In Chapters 4 and 5, novel antimicrobial materials have been designed by coating a quaternary ammonium compound (QAC) polymer, that is poly[2-(dimethyl decyl ammonium) ethyl methacrylate] (PQDMAEMA), onto the surface of various MOF-based materials (*e.g.*, UiO-66-NH_2, g-C_3N_4/MIL-125-NH_2) to form active composites for airborne bacterial inactivation. These rationally designed MOF composites demonstrated great antibacterial activities where electrostatic contact-killing and photogenerated reactive oxygen species (ROS) are utilized for efficient disinfection. In-depth investigations on the biointerface were carried out with the aid of several advanced techniques, such as the Zeta-potential analyzer, fluorescence laser confocal microscope (CLSM), and atomic force microscope (AFM). The results showed

that the adhesion of bacterial cells towards the photocatalyst surface leads to significantly enhanced photocatalytic bactericidal efficiencies.

The work from this dissertation is expected to broaden the applications of MOF-based materials and advance the understanding of the interactions between MOFs and pollutants from the molecular level, which should have a significant impact on the rational design of MOF-based materials for air quality control and improvement.

Chapter 2. Development of a Novel Bimetallic Metal-Organic Framework (MOF) for H_2S Detection.

Journal of Solid State Chemistry. 288:121434 (2020)

DOI: 10.1016/j.jssc.2020.121434

Abstract

A novel bimetallic MOF (i.e., Fe_xAl_{1-x}-MIL) with fluorescence quenching in the probe, was constructed to detect H_2S based on a “turn-on” effect in an aqueous system. Interestingly, a trace amount of Al^{3+} replaced by Fe^{3+} in the parent MOF Al-MIL-53-NH_2 causes significant fluorescence quenching in the bimetallic MOF, which is attributed to the strong ligand to metal charge transfer between unpaired electrons in Fe^{3+} and π-conjugated BDC-NH_2 ligands. After H_2S treatment, a fluorescence augmentation was observed, with a good linear relationship between H_2S concentration (0-38.46 μM) and fluorescence intensity, indicating that $Fe_{0.05}Al_{0.95}$-MIL could be used for quantitative H_2S detection. Particularly, Fe^{3+} in the bimetallic MOF seized by S^{2-} facilitated the partial degradation and subsequent release of BDC-NH_2 ligands, which were determined to be real fluorophores that contributed to the fluorescence enhancement. This study offers new insights into the luminescent bimetallic MOF design and would expand its application in chemical sensing.

2.1 Introduction

Hydrogen sulfide (H_2S) is a characteristic volatile organic compound (VOC). A fluorescence-based sensing technique is one of the most promising analytical methods for H_2S detection due to its high sensitivity, desirable selectivity, short response time, and readily visible imaging.[86-91] In particular, a fluorescence-based "turn-on" strategy is always preferred to avoid false responses and unexpected signal-to-noise ratios (S/N), considering the detection usually occurs in a dark background.[92] The typical reactions based on the fluorescence "turn-on" effect can be categorized as follows: (1) nitro/azide reduction;[93] (2) coordination of H_2S with auxochromic groups;[25] and (3) transitional metal (e.g., Cu^{2+}, Ag^{+}) replacement.[94]

Up to the present time, various luminescent probes have been developed for H_2S detection. Among these fluorescent probes, metal-organic frameworks (MOFs), a class of porous crystalline polymers built from metal ions/clusters and organic ligands, have gained considerable attention because of their versatile and tunable optical properties.[73, 95-98] To realize the "turn-on" effect, ligand functionalization of luminescent MOFs is a widely used approach. The brief description of the "turn-on" process is as follows. First, before H_2S detection, the MOFs should be in the "turn-off" mode, which can be achieved by adding organic ligands containing azide or nitro groups. These strong electron-withdrawing groups can trap the most absorbed exciting energy and cause a quickly running internal singlet-triplet conversion, thus limiting the fluorescence emission.[28, 84, 99] Once treated by H_2S, these azide and nitro groups will be reduced to electron-donating amine groups, leading to less internal energy dissipation, and therefore, a fluorescence enhancement is observed. Another interesting approach is to introduce specific transitional metal ions (e.g., Cu^{2+}, Ag^{+}) that have high affinity with S^{2-} to the lanthanide-based (e.g., Eu, Tb) MOFs through a "one-pot" wet chemistry route or post-modification.[30, 92, 100]

Likewise, the fluorescence "turn-on" effect would also show up after silver/copper sulfide precipitation. However, most reported probes based on the above methods showed undesirable performance towards H_2S detection at a lower concentration (0-100 μM), which is mainly caused by the incomplete quenching in materials before H_2S treatment and insignificant resulting fluorophores released after being exposed to H_2S.

Recently, bimetallic MOFs have emerged as an option to create multiple functionalities by mixing two different metal ions as nodes in their framework.[101, 102] Since the fluorescent properties of MOFs are determined by the energy transfer between metal ions and ligands, the secondary incorporated metal ions in the parent MOF would provide more versatilities during the sensing process, making bimetallic MOFs a great platform for chemical detection. Some lanthanide-based MOFs discussed above were reported to contain different transitional metal ions (e.g., Cu^{2+}, Ag^{+}) in the material,[30, 92, 100] which makes them appear like "bimetallic MOFs". Nevertheless, these doped metal ions were simply bonded to ligands without replacing the original metal nodes in the framework, which makes the quenching effects in parent MOFs less effective. Therefore, complicated post-modification and a relatively large amount of quenching materials are often needed to keep MOFs from emitting fluorescence. Furthermore, the high expense of lanthanide elements or rare-earth elements also restricts their further development and practical application. Given bimetallic MOFs containing the secondary substitutional metal ions as constructing nodes were rarely reported for H_2S detection, an efficient fluorescence quencher in parent MOF but with the ability to induce the "turn-on" effect is in urgent demand.

We herein report a novel bimetallic MOF, i.e., $Fe_{0.05}Al_{0.95}$-MIL for H_2S detection in an aqueous system. Within this bimetallic MOF, two cost-effective and earth-abundant transitional metals (Fe^{3+} and Al^{3+}) were used as constructing nodes, while 2-aminobenzene-1,4-dicarboxylic

acid (BDC-NH_2) was applied as a bridging ligand. The parent MOF, Al-MIL-53-NH_2, is the support matrix as it produces strong blue fluorescence with the existence of -NH_2 group.[103] Fe^{3+} is a strong fluorescence quencher used in many luminescent MOF probes.[104, 105] Because of partial Fe substation with Al ions in the Al-MIL-53-NH_2 framework, a strong ligand to metal charge transfer (LMCT) was generated between Fe^{3+} ions and BDC-NH_2 ligands, which made the quenching effect extremely efficient within the bimetallic MOF (e.g., $Fe_{0.05}Al_{0.95}$-MIL). After being exposed to H_2S treatment (0-38.46 μM), a "turn-on" effect was observed and a good linear relationship was also obtained between fluorescence intensity and H_2S concentration, indicating the bimetallic MOF could be used for selective and quantitative H_2S detection. To unravel the mechanism of fluorescence enhancement, systematic characterizations and analyses were conducted on both remained undissolved particles and supernatants. The results showed that during the H_2S sensing process, Fe^{3+} in the bimetallic MOF was "pulled out" and seized by S^{2-} to form Fe_2S_3, which was subsequently converted to FeS and S. Then the FeS would be further oxidized to Fe^{3+} and SO_4^{2-} in the presence of air. Additionally, the $Fe_{0.05}Al_{0.95}$-MIL was proved to be partially decomposed after H_2S treatment, and the released BDC-NH_2 ligands were determined to be real fluorophores that contributed to the fluorescence enhancement. We believe that the outcome of this work could shed light on the rational design of fluorescence-based bimetallic MOFs for chemical sensing.

2.2 Materials and Methods

Chemicals Aluminum chloride hexahydrate ($AlCl_3 \cdot 6H_2O$, 99%), Ion chloride hexahydrate ($FeCl_3 \cdot 6H_2O$, 99%), and 2-amino-1,4-dicarboxylic acid ($C_8H_7NO_4$, BDC-NH_2, 99%) were purchased from Sigma-Aldrich. Acetone (C_3H_6O, 99.5%), N, N-dimethylformamide ($HCON(CH_3)_2$, DMF) were obtained from VWR Corporation. Ethanol (C_2H_5OH, 190 proof) was

purchased from Gold Shield. Deionized (DI) water was used to prepare solutions. All chemicals were used without further purification.

Synthesis of Al-MIL-53-NH_2 Al-MIL-53-NH_2 was synthesized based on a previous report.[106] A mixture of $AlCl_3 \cdot 6H_2O$ (1.45g), NH_2-BDC (1.1g), and 50 ml DI water was heated using a 100 ml Teflon-lined steel autoclave at 150 °C for 5 hours. The obtained precipitates were washed with DMF three times and subsequently activated. The activation was conducted by immersing as-synthesized crude materials in 60 ml DMF at 155 °C for 12 hours. The above activation procedure was repeated a second time. Finally, the pale-yellow particles were dried at 155 °C in the air for 24 hours.

Table 2.1 Precursor Compositions for Fe_xAl_{1-x}-MIL

Samples	**DI (ml)**	**$FeCl_3 \cdot 6H_2O$ (g)**	**$AlCl_3 \cdot 6H_2O$ (g)**	**Fe:Al Mole Ratio**	**BDC-NH_2 (g)**
$Fe_{0.05}Al_{0.95}$-MIL	50	0.081	1.37	0.05:0.95	1.1
$Fe_{0.1}Al_{0.9}$-MIL	50	0.162	1.30	0.1:0.9	1.1
$Fe_{0.2}Al_{0.8}$-MIL	50	0.324	1.16	0.2:0.8	1.1

Synthesis of Fe_xAl_{1-x}-MIL (x = 0.05, 0.1, and 0.2) In a typical procedure, mixtures of $AlCl_3 \cdot 6H_2O$, $FeCl_3 \cdot 6H_2O$, and NH_2-BDC with different ratios were suspended in 50 ml DI water and then heated using a 100 ml Teflon lined steel autoclave at 150 °C for 5 hours. Detailed precursor compositions are listed in **Table 2.1**. The obtained particles were washed with DMF three times and subsequently activated. The as-synthesized materials were kept in 60 ml DMF at 155 °C for 12 hours. The above activation procedure was repeated a second time. Finally, the orange particles were dried at 155 °C in the air for 24 hours. In this study, the activated bimetallic MOFs are labeled as Fe_xAl_{1-x}-MIL with the Fe/Al molar ratios indicated by the

precursors' molar ratio in the subscript. It should be noted that this value does not represent the actual Fe/Al molar ratio in the final product. The precise experimental Fe/Al ratios were determined by EDX (energy-dispersive X-ray spectroscopy), which are discussed in the next section.

Synthesis of Fe-MIL-53-NH_2 Fe-MIL-53-NH_2 was synthesized according to a previous study.[107] A mixture of $FeCl_3 \cdot 6H_2O$ (1.35 g), NH_2-BDC (0.9 g), and 50 ml DI water was placed in the 100 ml Teflon-sealed steel autoclave and heated in an oven at 150 °C for 48 hours. The precipitates were washed with DI water, DMF, and acetone, respectively. Then the as-synthesized crude materials were activated in 15 ml ethanol at 150 °C for 48 hours. The above activation procedure was repeated a second time. The resulting dark brown solids were recovered by centrifuge and dried in air at 150 °C.

Materials Characterization The structure of as-synthesized materials was analyzed by powder X-ray diffraction (PXRD) using PANalytical X'Pert Pro MPD. Element mapping was conducted using an SEM (scanning electron microscope, Su-70, Hitachi) equipped with energy-dispersive X-ray spectroscopy (EDX). Vibration analysis of functional groups was carried out with a Fourier transform infrared (FT-IR) spectrometer (Nicolet iS50, Thermo Scientific). The optical absorption spectra were obtained from the UV-Vis measurements using an Evolution UV-220 spectrophotometer. The fluorescence properties of the samples were characterized by a fluorescence spectrometer (PTI QuantaMaster-400). The quantum yields (QY) were determined as the integrated intensity of the luminescence signal divided by that of absorption. The absorption integrated intensity was measured by subtracting the luminescence signal from the blank reference sample in an integrating sphere. X-ray photoelectron spectroscopy (XPS, Thermo Scientific ESCALAB 250) was used to investigate the chemical state of the elements on

the surface of the samples.

H_2S Fluorescence Sensing Measurements NaHS was used as the H_2S source and dissolved in DI water to form a transparent solution.[108] In this study, "H_2S treated" or "H_2S treatment" means that the samples are suspended in NaHS solution with a specific concentration. In a typical experiment, 0.7 mg bimetallic MOF was suspended in a cuvette containing 3 ml DI water. A varying volume (0-140 μL) of NaHS (1.0 mM) solution was then added into the above MOF suspension and the spectrum was taken within 90 seconds. The corresponding supernatant and suspended undissolved particles were separated by centrifugation at 12000 rpm for 5 minutes. Another fluorescence measurement of the re-collected particles that were resuspended into 3.0 ml DI water was conducted for comparison. For the fluorescence measurements, the excitation wavelength was fixed at 330 nm and the emission spectra were recorded in the range from 380 nm to 580 nm. Both the emission and excitation slits were set to be 2 nm.

2.3 Results and Discussions

A "one-pot" hydrothermal method was utilized for the synthesis of bimetallic MOFs, where the substitution of Fe atoms in the Al-MIL-53-NH_2 framework was achieved by adjusting the mole ratio of Fe to Al from 0.05 to 0.2 in the precursor. As shown in **Figure 2.1(a-e)**, with increasing Fe/Al ratios, the color of Fe_xAl_{1-x}-MIL gradually turned from yellow to the dark brown, indicating the successful substitution of Fe^{3+} with partial Al^{3+} inside the framework. The element composition within $Fe_{0.05}Al_{0.95}$-MIL was also confirmed by EDX analysis. The results showed that altering the Fe/Al ratio from 0.05 to 0.2 led to the Fe/Al ratio in products changing from 0.048 to 0.181, which indicates that the percentage of Fe in Fe_xAl_{1-x}-MIL can be tuned by simply changing the starting Fe concentration in the precursor. Moreover, elemental mapping of $Fe_{0.05}Al_{0.95}$-MIL (**Figure 2.1(f-i)**) confirms the uniform distribution of Fe within the Al-MIL-53-

NH_2 matrix.

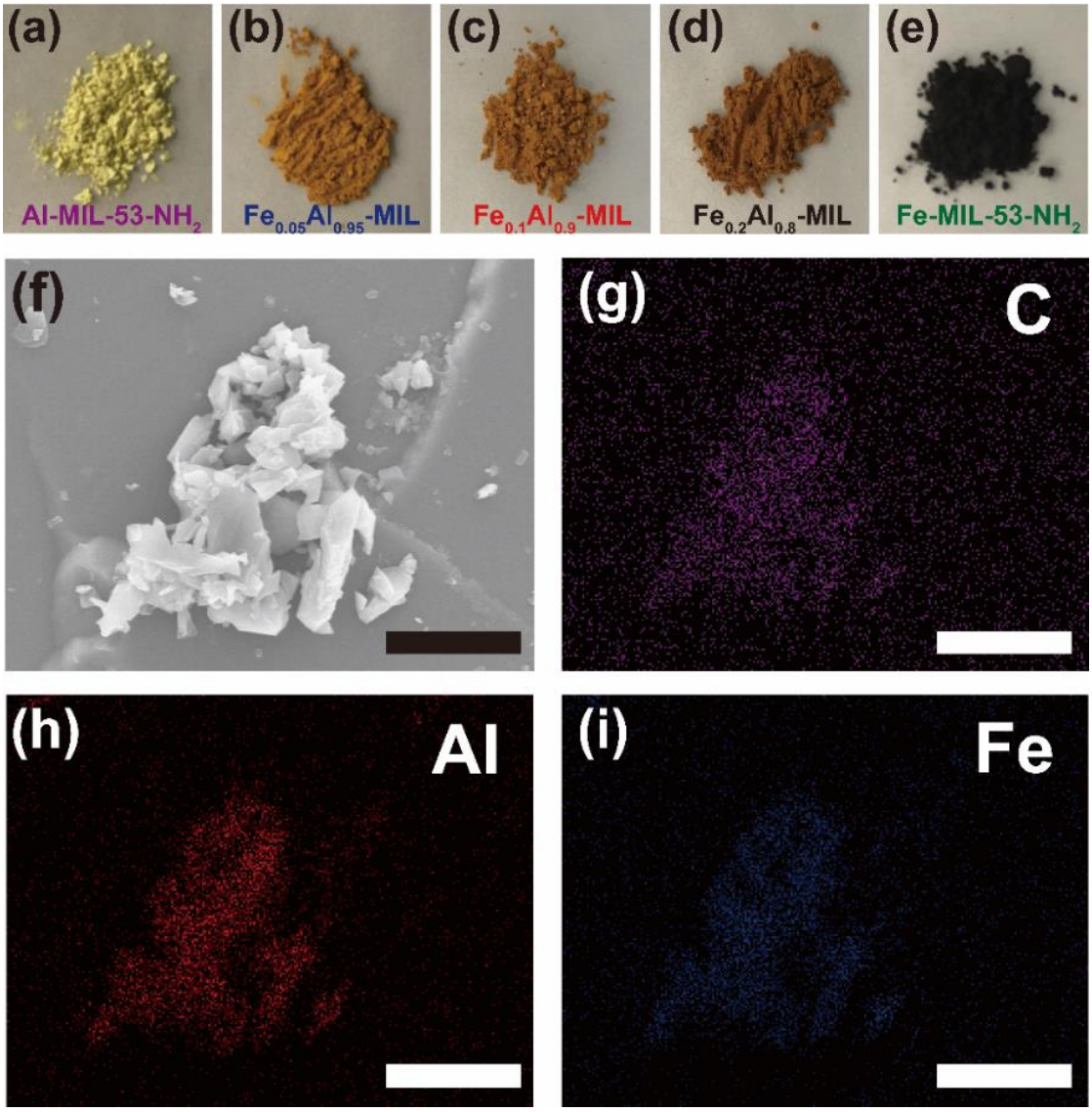

Figure 2.1 Digital images of Al-MIL-53-NH_2 (a), Fe_xAl_{1-x}-MIL (x = 0.05, 0.1, and 0.2) (b-d), and Fe-MIL-53-NH_2 (e); SEM image (f) and elemental mapping (g-i) of $Fe_{0.05}Al_{0.95}$-MIL (f). Scale bar: 10 μm.

In addition to the investigations on the morphology and chemical composition, structure analysis was conducted by PXRD. As shown in **Figure 2.2a**, all the Fe_xAl_{1-x}-MIL (x = 0.05, 0.1, and 0.2) and Al-MIL-53-NH_2 exhibited the same PXRD patterns, indicating these as-synthesized bimetallic MOFs maintained a structure similar to that of Al-MIL-53-NH_2. Specifically, the

framework of Fe_xAl_{1-x}-MIL is built from AlO_6 octahedra connected via trans-bridging OH ions and carboxylate moieties from BDC-NH_2 linkers but with different amounts of Fe substitution of Al in pure parent Al-MIL-53-NH_2, as shown in **Figure 2.2b**.[109, 110] It should be noted that no phases of Fe-MIL-53-NH_2 were observed in the PXRD patterns of Fe_xAl_{1-x}-MIL, which demonstrated that the as-prepared bimetallic MOFs are indeed MOFs with different metallic nodes rather than a mixture of monometallic MOFs.[111] Furthermore, we conducted a high-resolution PXRD scan for peak (110) from 12.0° to 12.8° (**Figure 2.2c**). Interestingly, the position of peak (110) shifts from 12.46° to a lower angle of 12.29° with increased Fe concentration in the products (**Figure 2.2d**). This can be explained based on the well-known Bragg's law:

$$d = \frac{n\lambda}{2\sin\theta} \tag{2.1}$$

where d is the interplanar spacing of (110); n is the positive integer (1); λ is the X-ray wavelength (λ = 1.5406 Å); θ is the Bragg angle. A smaller Bragg angle of Fe_xAl_{1-x}-MIL corresponds to a larger (110) interplanar spacing (**Figure 2.2d**), namely, the lattice of the framework expands with more Fe substitution of Al in the Al-MIL-53-NH_2 matrix. This phenomenon is likely caused by the replacement of the larger atomic radii of Fe (156 pm) with Al (118 pm).[112]

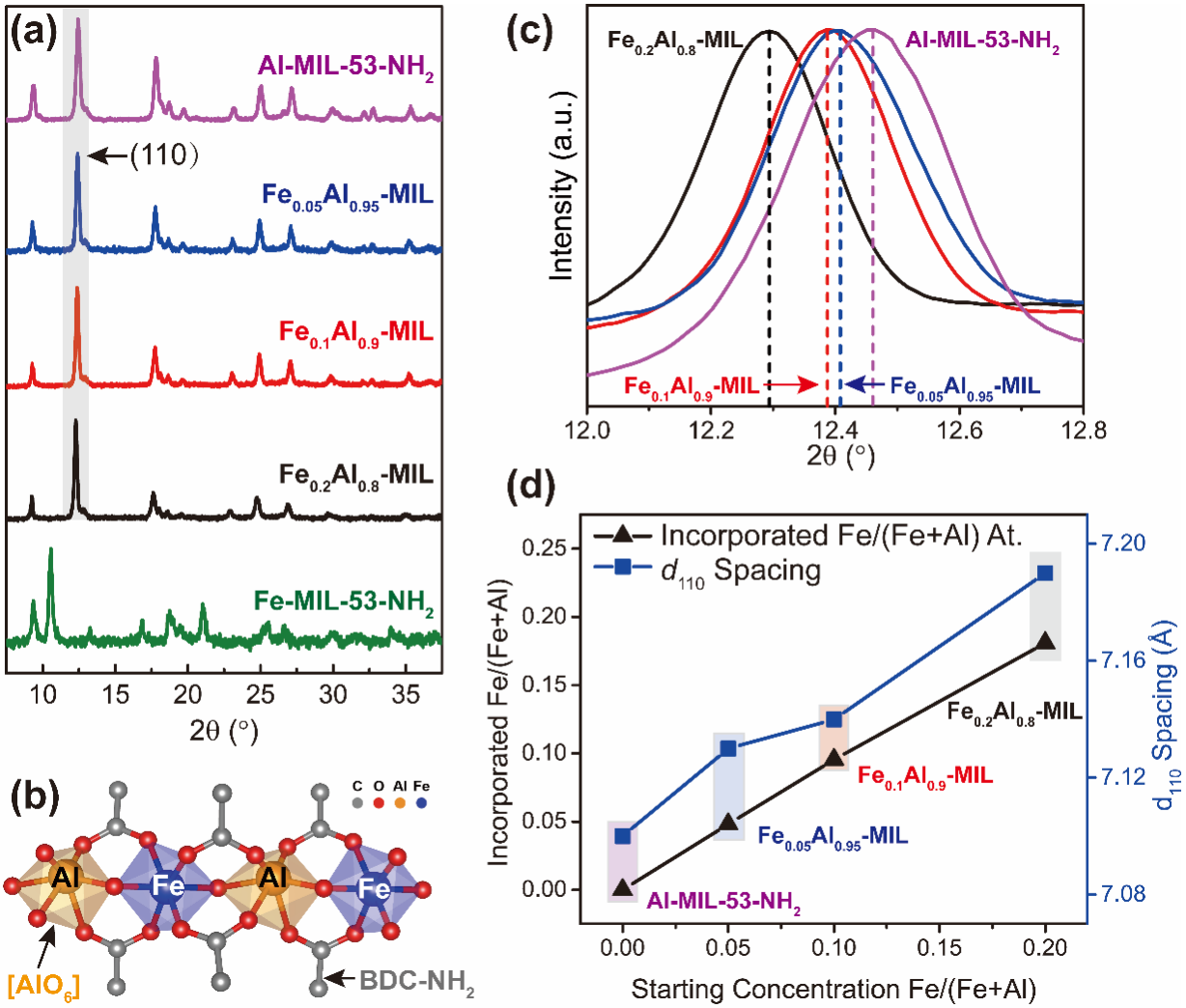

Figure 2.2 (a) PXRD patterns of Al-MIL-53-NH_2, Fe_xAl_{1-x}-MIL, and Fe-MIL-53-NH_2; (b) Fe_xAl_{1-x}-MIL with a ball and stick representation of a site-isolated Fe within the MIL-53-NH_2 octahedra [AlO_6] chain; (c) High-resolution PXRD scan at (110) peak of Al-MIL-53-NH_2 and Fe_xAl_{1-x}-MIL; (d) d_{110} spacings and incorporated Fe concentrations in products versus Fe concentration in precursors.

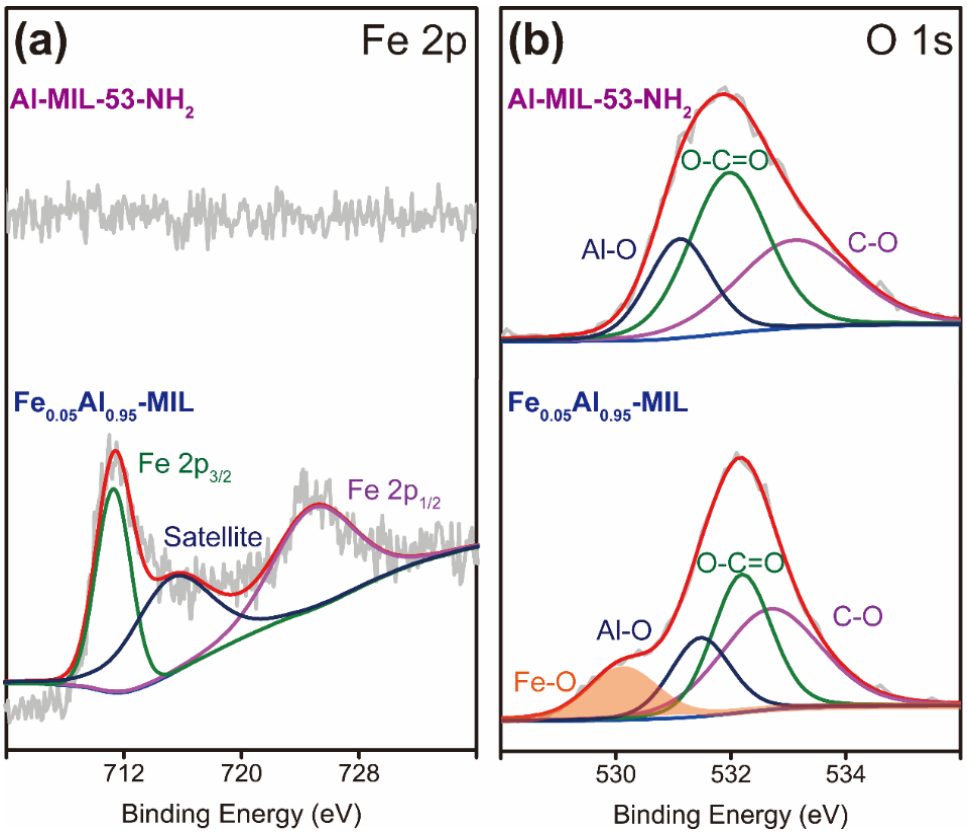

Figure 2.3 Fe 2p (a) and O 1s (b) XPS spectra of Al-MIL-53-NH_2 and $Fe_{0.05}Al_{0.95}$-MIL.

Further evidence of Fe substitution within the Al-MIL-53-NH_2 matrix was studied using an XPS. Herein, we select $Fe_{0.05}Al_{0.95}$-MIL as a representative bimetallic MOF. To analyze the effects on the coordination environment caused by Fe substitution, high-resolution XPS spectra of Fe 2p and O 1s were obtained, as shown in **Figure 2.3**. Clearly, no Fe signal was captured in Al-MIL-53-NH_2 while prominent Fe^{3+} peaks (Fe $2p_{3/2}$ at 724.9 eV and Fe $2p_{1/2}$ at 711.3 eV) were observed in $Fe_{0.05}Al_{0.95}$-MIL, demonstrating successful substitution of Fe in Al-MIL-53-NH_2.[111] **Figure 2.3b** shows the high-resolution XPS spectra of O 1s for both Al-MIL-53-NH_2 and $Fe_{0.05}Al_{0.95}$-MIL. The peaks at 531.4 eV, 532.2 eV, and 532.7 eV for both samples are attributed to the Al-O, O-C=O, and C-O bonds, respectively.[113, 114] In particular, the peak at 530.1 eV in the orange shadow was observed in $Fe_{0.05}Al_{0.95}$-MIL (**Figure 2.3b**), which was ascribed to the

existence of a newly constructed Fe-O bond.[115] Such well-founded evidence of Fe in the O 1s spectrum of $Fe_{0.05}Al_{0.95}$-MIL suggests that Fe ions have been successfully incorporated into the framework, which is consistent with the results shown in **Figure 2.1**.

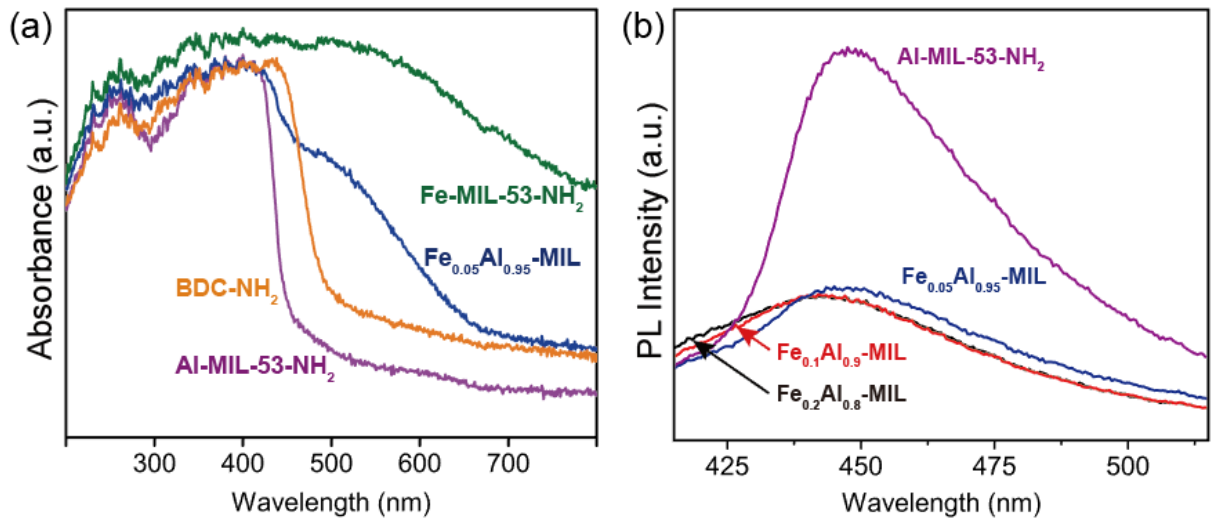

Figure 2.4 (a) UV-vis spectra of $BDC\text{-}NH_2$, Al-MIL-53-NH_2, $Fe_{0.05}Al_{0.95}$-MIL, and Fe-MIL-53-NH_2; (b) PL spectra of Al-MIL-53-NH_2 and Fe_xAl_{1-x}-MIL. Excitation wavelength: 330 nm.

To elucidate the behavior of Fe ions within the bimetallic MOF, the optical responses of $BDC\text{-}NH_2$, Al-MIL-53-NH_2, $Fe_{0.05}Al_{0.95}$-MIL, and Fe-MIL-53-NH_2 were examined by UV-vis spectroscopy. As displayed in **Figure 2.4a**, the MOFs (e.g., Al-MIL-53-NH_2, $Fe_{0.05}Al_{0.95}$-MIL, and Fe-MIL-53-NH_2) share similar absorption spectra with the bridging linker $BDC\text{-}NH_2$ within the UV region, where one intense peak at 280 nm is ascribed to the $\pi \rightarrow \pi^*$ electronic transitions of the aromatic ring and the other peak in the range of 300-420 nm is originated from the introducing NH_2 groups from $BDC\text{-}NH_2$.[116, 117] For Fe-MIL-53-NH_2, the wide band over the entire visible region is due to the spin-allowed *d-d* transition of Fe^{3+} ($^6A_{1g} \rightarrow {}^6A_{1g} + {}^4E_g(G)$),[118, 119] which is also observed in bimetallic MOF $Fe_{0.05}Al_{0.95}$-MIL. In general, the Al-MIL-53-NH_2 has no absorption in the visible region, while Fe-MIL-53-NH_2 shows strong visible light absorption. The UV-vis spectra of $Fe_{0.05}Al_{0.95}$-MIL showed features of both components, and the

absorption in the visible region becomes stronger with increasing Fe contents in the bimetallic MOF, which further supports the successful incorporation of Fe in the bimetallic MOF. Not surprisingly, this increased light absorbance in the visible region with increasing Fe concentration in the Fe_xAl_{1-x}-MIL, is also reflected by color variation changing from light yellow to dark brown. (**Figure 2.1(a-e)**)

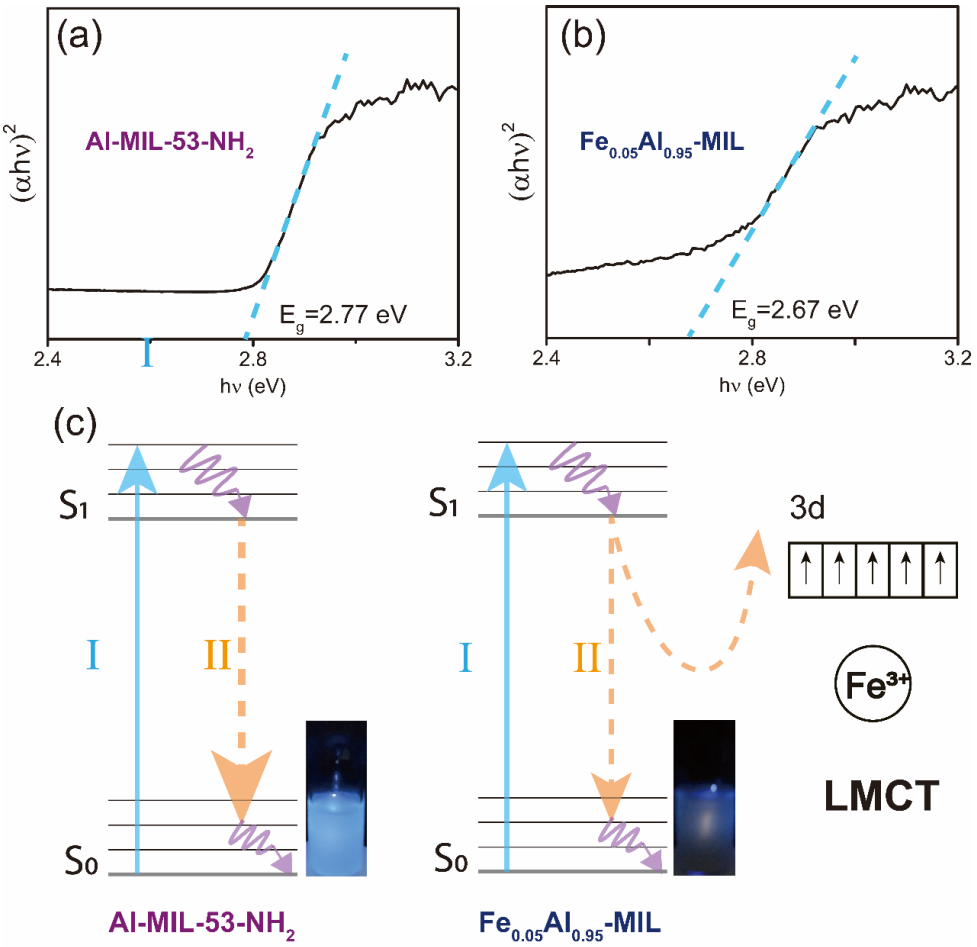

Figure 2.5 Tauc plots of bulk Al-MIL-53-NH_2 (a) and $Fe_{0.05}Al_{0.95}$-MIL (b); (c) schematic illustration of energy transfer within the $Fe_{0.05}Al_{0.95}$-MIL. Inset digital images are Al-MIL-53-NH_2 and $Fe_{0.05}Al_{0.95}$-MIL suspensions under UV light (330 nm).

The variation of fluorescence due to the presence of Fe in the bimetallic MOF was investigated by a PL spectrometer. As shown in **Figure 2.4**, the parent MOF Al-MIL-53-NH_2 demonstrated a characteristic blue emission with a maximum peak at 449 nm under the

excitation at 330 nm. For the parent MOF Al-MIL-53-NH_2, the luminescence in the framework is centered on the linker BDC-NH_2 since both BDC-NH_2 and Al-MIL-53-NH_2 have similar emission spectra under UV light irradiation. Within the bimetallic MOF $Fe_{0.05}Al_{0.95}$-MIL, these fluorescence emitting -NH_2 groups were confirmed intact by FT-IR characterization**.** However, the fluorescence intensities of Fe_xAl_{1-x}-MIL were reduced significantly, as shown in **Figure 2.4b**. As a transition metal, Al ions within the MOF would induce ligand to metal charge transfer, which is not favorable for fluorescence generation. Yet, Al-MIL-53-NH_2 with a quantum yield of 14.7% is still observed compared to $Fe_{0.05}Al_{0.95}$-MIL (QY undetectable). This quenching effect brought upon by the Fe incorporation can be explained as follows. For the light absorption (**I**) process, both Al-MIL-53-NH_2 and $Fe_{0.05}Al_{0.95}$-MIL have nearly the same absorbance values as that of BDC-NH_2 under irradiation, as shown in **Figure 2.4a,** which demonstrates that the absorption process in the MOF occurs on the linker. In addition, the band gaps (E_g) for Al-MIL-53-NH_2 and $Fe_{0.05}Al_{0.95}$-MIL were determined to be 2.77 eV and 2.67 eV (**Figure 2.5**), respectively, further indicating that the partial replacement of Al ions with Fe in MOF has negligible effects on the absorption process. As shown in **Figure 2.5c**, in the emission process (**II**), the spin-allowed transition between the excited singlet state ($\mathbf{S_1}$) to the ground singlet state ($\mathbf{S_0}$) is responsible for the fluorescence emission. Since Fe ions contain unpaired electrons within the matrix of the Al-MIL-53-NH_2, the electrons from the photon-excited organic linker BDC-NH_2 will be transferred into the partially filled d-orbitals of Fe ions. With such strong LMCT competence with linker-based (BDC-NH_2) emission, the fluorescence of as-synthesized Fe_xAl_{1-x}-MIL bimetallic MOF would decrease and even be quenched. Given that increasing incorporated Fe concentration (x = 0.1 and 0.2) does not contribute to further fluorescence quenching (**Figure 2.4**), we selected $Fe_{0.05}Al_{0.95}$-MIL for the following H_2S sensing applications.

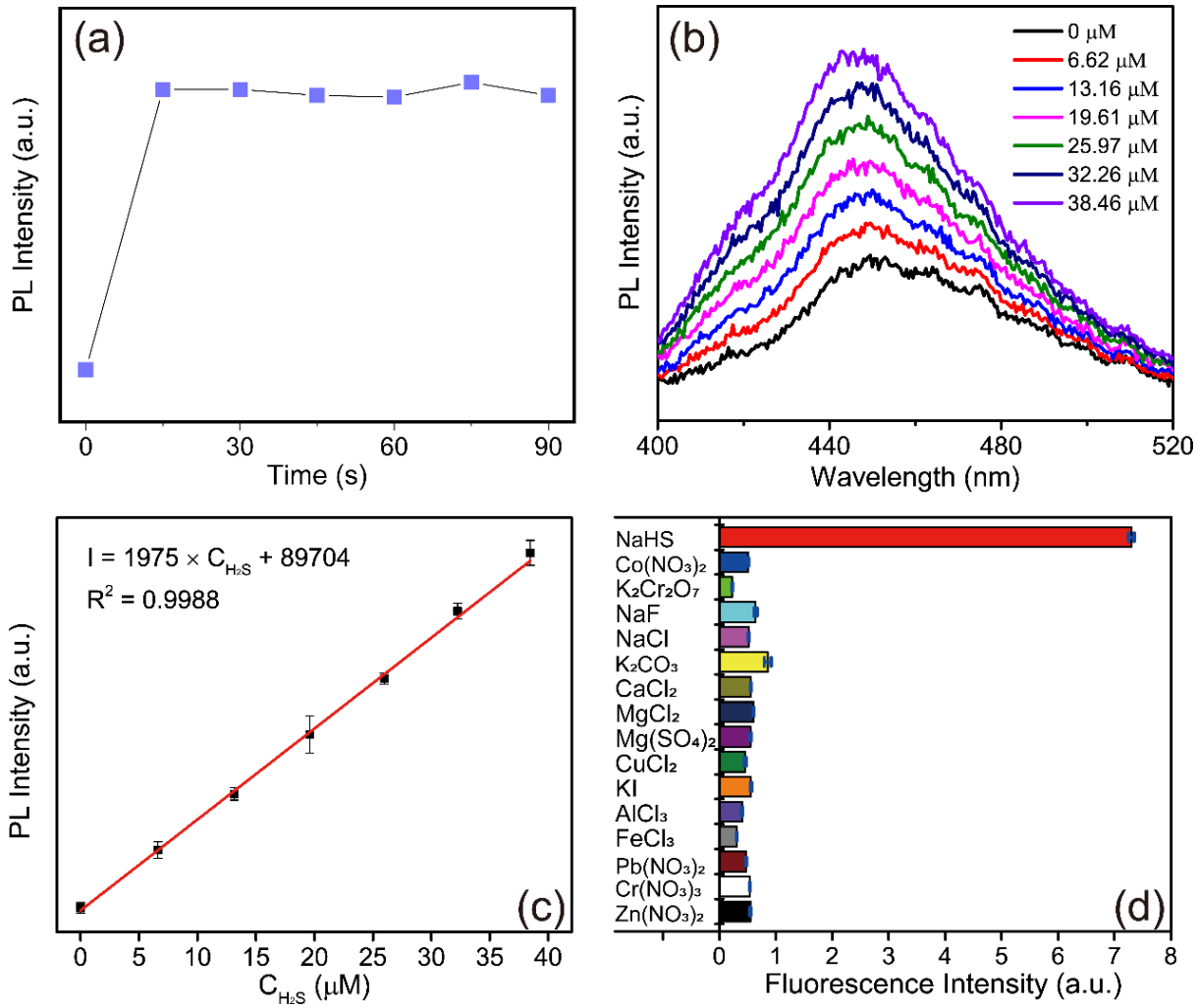

Figure 2.6 (a) Fluorescence intensity of $Fe_{0.05}Al_{0.95}$-MIL towards addition of 20 μL NaHS (1.0 mM) after 0-90 s; (b) fluorescence spectra of $Fe_{0.05}Al_{0.95}$-MIL with the increasing concentrations of NaHS (0-38.46 μM) (c) Linear relationship (0-38.46 μM) of the emission intensity of $Fe_{0.05}Al_{0.95}$-MIL enhanced by H_2S; (d) Fluorescence intensity of $Fe_{0.05}Al_{0.95}$-MIL at 449 nm toward various analytes (1 mM).

The performance of $Fe_{0.05}Al_{0.95}$-MIL towards H_2S detection in an aqueous system was investigated by the addition of different volumes of NaHS solution (1.0 mM) in a 3.0 ml $Fe_{0.05}Al_{0.95}$-MIL suspension. The fluorescence intensity of $Fe_{0.05}Al_{0.95}$-MIL suspension was immediately enhanced after the addition of 20 μL NaHS (1.0 mM); the intensity stabilized within 90 seconds (**Figure 2.6a**), which is faster than most previously reported H_2S probes.[28, 84, 120]

Additionally, the effect of pH on the $Fe_{0.05}Al_{0.95}$-MIL towards H_2S was studied and the fluorescence intensity remained unchanged when the pH ranged from 3 to 9. As depicted in **Figure 2.6(b,c)**, a very strong linear relationship (R^2 = 0.9988) was obtained between the fluorescence intensity of $Fe_{0.05}Al_{0.95}$-MIL and H_2S concentrations (0-38.46 μM). The limit of detection (LOD = 3σ/S) was also determined to be 4.69 μM. The above results indicate that the $Fe_{0.05}Al_{0.95}$-MIL can be used for quantitative H_2S detection in an aqueous system. Selective sensing of $Fe_{0.05}Al_{0.95}$-MIL on H_2S in water has been validated by observing parallel relations using a variety of common interfering substances. As shown in **Figure 2.6d**, the H_2S analyte showed a significant "turn-on" response, while no additional effects were observed with all selected interferents. Since the $Fe_{0.05}Al_{0.95}$-MIL is already in the "turn-off" mode, typical strong fluorescence quenchers such as transition metal ions ($CuCl_2$, $FeCl_3$, $AlCl_3$, $Co(NO_3)_2$) and oxidative anions (NaF, $K_2Cr_2O_7$) exhibited negligible effects on the fluorescence intensity of the $Fe_{0.05}Al_{0.95}$-MIL sample, as shown in **Figure 2.6d**. It should be noted that no obvious fluorescence changes were observed for some more electrically neutral interferents (NaCl, $CaCl_2$, $MgCl_2$) and reducing interferents (KI) since the Fe^{3+} within the $Fe_{0.05}Al_{0.95}$-MIL is an oxidative agent. All the results discussed above indicate that the as-synthesized bimetallic MOF $Fe_{0.05}Al_{0.95}$-MIL can serve as an excellent sensor for quantitative H_2S detection in complex aqueous systems.

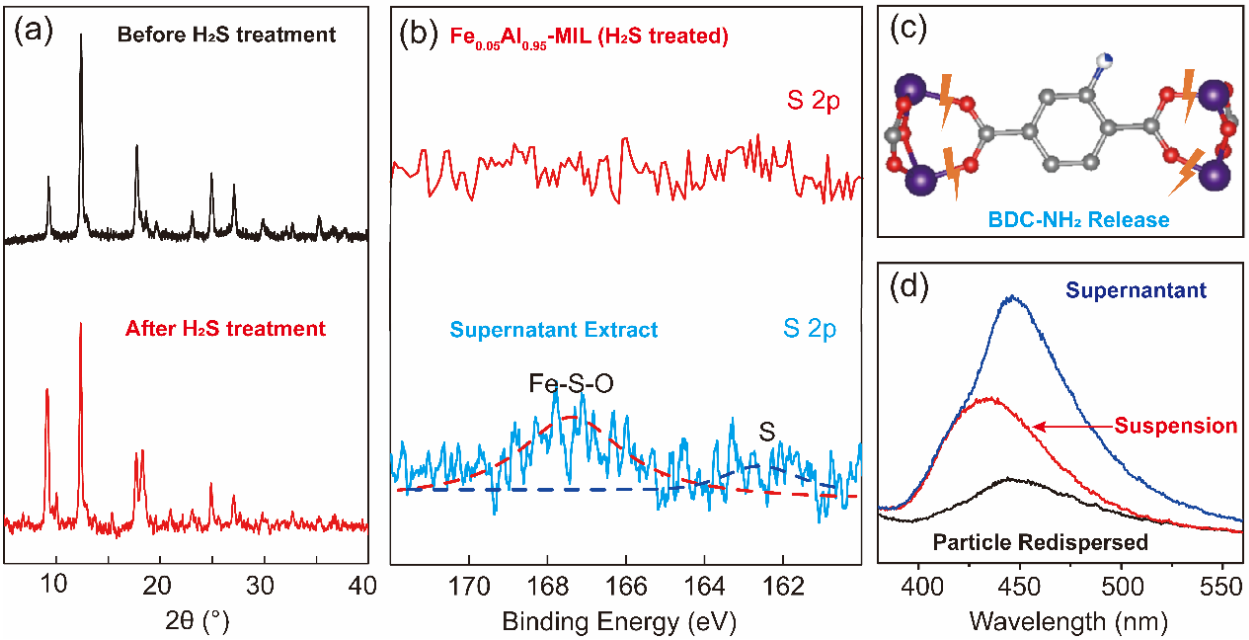

Figure 2.7 (a) PXRD patterns of $Fe_{0.05}Al_{0.95}$-MIL before and after H_2S treatment; (b) S 2p spectra of retained H_2S-treated $Fe_{0.05}Al_{0.95}$-MIL particles and supernatant extract; (c) Scheme of BDC-NH_2 released during H_2S treatment; and (d) PL spectra of supernatant, suspension, and particle re-dispersed in water.

The "turn-on" effect on $Fe_{0.05}Al_{0.95}$-MIL towards H_2S treatment in an aqueous system was investigated by the analysis of both particles retained in the suspension and supernatant extracts. Detailed experimental information was described in our previous report.[83] The crystallinity of the remaining H_2S-treated $Fe_{0.05}Al_{0.95}$-MIL particles was initially determined by PXRD. As shown in **Figure 2.7a**, the structure of H_2S treated $Fe_{0.05}Al_{0.95}$-MIL was almost completely maintained except for several extra minor peaks and peak ratio variations, which are probably caused by local defects due to the interaction between H_2S and bimetallic MOF. The FT-IR spectrum of H_2S treated $Fe_{0.05}Al_{0.95}$-MIL was also measured, and almost the same spectrum was obtained, indicating that recollected $Fe_{0.05}Al_{0.95}$-MIL after H_2S detection shared similar surface chemistry properties with the unreacted probe $Fe_{0.05}Al_{0.95}$-MIL. To identify the reaction site of H_2S during the sensing process, high-resolution S 2p scanning by an XPS

spectrometer was conducted. As shown in **Figure 2.7b**, no S information was captured for H_2S treated $Fe_{0.05}Al_{0.95}$-MIL particles, while two S-related peaks located at 162.2 eV and 167.7 eV were observed from the supernatant extracts; these peaks are likely attributed to Fe-S-O and precipitated sulfide (S), respectively.[121] Additionally, for H_2S treated $Fe_{0.05}Al_{0.95}$-MIL particles, Fe can be hardly observed in the XPS spectrum compared to the pristine $Fe_{0.05}Al_{0.95}$-MIL (**Figure 2.3a**), which demonstrated that Fe has been "pulled out" from the framework by H_2S. Moreover, $-NH_2$ groups observed in the FT-IR spectrum of supernatant extracts further confirmed that the BDC-NH_2 linker was released during the partial decomposition of bimetallic MOF during H_2S detection. Considering the loss of Fe in H_2S treated $Fe_{0.05}Al_{0.95}$-MIL and the existence of the released BDC-NH_2 linker in the supernatant, the possible reaction process and mechanism could be proposed as follows. During the H_2S sensing process, Fe^{3+} in $Fe_{0.05}Al_{0.95}$-MIL is seized by H_2S rapidly due to the ultrahigh affinity between S^{2-} and Fe^{3+} (ultra-small solubility product constant of Fe_2S_3, 1.4×10^{-88}). The rapid interaction between S^{2-} and Fe^{3+} could also be reflected by the prompt fluorescence deduction within the first 15 seconds after the addition of NaHS (**Figure 2.6a**). However, the direct reaction product Fe_2S_3 is not stable and could convert to FeS and S immediately; FeS would further be oxidized to Fe^{3+} ($Fe_2(SO_4)_3$) in the presence of air (**Figure 2.7b**). Since Fe nodes were lost through the breakage of the Fe-O bond in the $Fe_{0.05}Al_{0.95}$-MIL framework, the linker was released into the solution. (**Figure 2.7c**) Furthermore, PL spectra of both supernatant and resuspended particles were measured again under the same light irradiation. It was found that the supernatant containing the released BDC-NH_2 linkers had the highest fluorescence intensity, while the H_2S treated particles showed negligible contribution to fluorescence enhancement. This is caused by the fact that undissolved H_2S treated $Fe_{0.05}Al_{0.95}$-MIL could absorb and scatter the incident excitation light, thus decrease

the fluorescence intensity. Therefore, it can be concluded that the released BDC-NH_2 ligands were real fluorophores that contributed to the fluorescence enhancement.

2.4 Conclusions

With the assistance of a simple "one-pot" hydrothermal method, a series of bimetallic MOFs, Al_xFe_{1-x}-MIL (x = 0.05, 0.1, and 0.2) have been synthesized for H_2S detection in an aqueous system. Detailed investigations were conducted on bimetallic MOFs including their crystalline structures, optical properties, and H_2S performance. The results showed that only a small amount of secondary Fe^{3+} ions could result in a complete fluorescence quenching in the bimetallic MOF, which could be attributable to the strong LMCT between Fe^{3+} and BDC-NH_2. The response of $Fe_{0.05}Al_{0.95}$-MIL towards H_2S was also tested in an aqueous system. A fluorescence enhancement was observed and a very strong linear relationship was achieved between fluorescence intensity and H_2S concentrations (0-38.46 μM), indicating that $Fe_{0.05}Al_{0.95}$-MIL could be a good candidate for selective and H_2S quantitative detection. Based on the analysis of the H_2S treated bimetallic MOF particles and supernatant, a possible mechanism was explored. During the H_2S sensing process, the secondary Fe^{3+} ions were "pulled out" by S^{2-} from the framework with a concomitant of partial decomposition of bimetallic MOF. The released BDC-NH_2 ligands from the structure were identified to be the real fluorophores responsible for the fluorescence enhancement. Overall, partial substitution of Al ions in Al-MIL-53-NH_2 with secondary Fe^{3+} ions was proved to be an effective method to design a luminescent MOF probe for H_2S detection. We believe this strategy would expand the usage of bimetallic MOFs for chemical sensing applications.

Chapter 3. Unraveling the origin of the "Turn-On" effect of Al-MIL-53-NO_2 during H_2S detection

CrystEngComm. 2020;22(2):195-204.

DOI: 10.1039/c9ce01595g

Abstract:

Nitro-functionalized metal-organic frameworks (MOFs), such as Al-MIL-53-NO_2, have been widely used in quantitative hydrogen sulfide (H_2S) detection based on the “turn-on” effect where fluorescence enhancement was observed upon contact with H_2S. This was believed to be caused by the fact that the electron-withdrawing -NO_2 groups in initial non-luminescent MOFs were reduced to electron-donating -NH_2 groups in the sensing process. However, since most H_2S detection is conducted in a suspension system consisting of MOFs and solvents, it is still unclear whether these -NH_2 groups are on MOFs or in liquid. Using Al-MIL-53-NO_2 as a model MOF, this work aims to answer this question. Specifically, the supernatant and undissolved particles separated from Al-MIL-53-NO_2 suspensions after being exposed to H_2S were analyzed systematically. The results show that it is the free BDC-NH_2 (2-aminobenzene-1, 4-dicarboxylic acid) in the solution rather than the formation of Al-MIL-53-NH_2 that really caused the fluorescence enhancement. In particular, the formed BDC-NH_2 is reduced from shedding BDC-NO_2 (2-nitrobenzene-1,4-dicarboxylic acid) during the decomposition of Al-MIL-53-NO_2, which is attacked by OH^- in the NaHS solution. We anticipate that this work will offer new ways of tracing fluorophores for the MOF-based sensing applications in an aqueous system.

3.1 Introduction

The fluorescence-based detection method has been growing rapidly because of its high selectivity and sensitivity, short response time, simplicity in operation, and easy observation in real-time imaging. [29, 122] Up till now, plenty of fluorescent materials have been designed and used for H_2S sensing. [123-125] Among these fluorescent materials, metal-organic frameworks (MOFs), a class of porous crystalline materials composed of bridged organic linkers and centered metal ions/clusters [126], are interesting candidates because the great abundance of functional ligands and metals endow MOFs with very promising physical and chemical properties. [127-130] Several luminescent MOFs have been used for H_2S detection in aqueous or real physiological systems. [28, 30, 84, 85, 92, 99, 100, 121, 131-139] Among these explored mechanisms of the H_2S sensing process, the "turn-on" effect is the most popular one, where original non-luminescent MOFs in the "turn-off" state, was activated and enhanced upon being exposed to H_2S. Nitro-functionalized MOFs have been proved to be effective probes for H_2S detection based on the "turn-on" effect.[28, 132, 138] Specifically, the nitro groups ($-NO_2$) in nitro-functionalized MOFs would decrease the electron density of the aromatic ring because of the unpaired electrons at nitrogen, which makes MOFs emit very weak fluorescence and stay in the "turn-off" state. After being treated by H_2S, electron-donating $-NH_2$ groups were obtained, and the "turn-on" signal in fluorescence was captured.

Based on this mechanism, Zr-UiO-66-NO_2 was first synthesized by Ghosh et al. to realize the "turn-on" response towards 0.0-4.0 mM H_2S through a transformation from Zr-UiO-66-NO_2 to Zr-UiO-66-NH_2. [131] Later on, Biswas et al. reported Ce-UiO-66-NO_2,[132] DUT-52-$(NO_2)_2$, [134], and Zr-UiO-66-$(NO_2)_2$ [84] for quantitative H_2S detection in physiological systems and living cells. The lowest detection limit at 92.31×10^{-9} M was recently reported by Qian et al. using polymer mixed-matrix membranes (MMM) developed by the combination of Al-MIL-53-NO_2

nanoparticles and PVDF (polyvinylidene fluoride). [138] Among all these nitro-functionalized MOF compounds, the linear relationships were obtained in the different ranges of H_2S concentrations with the fluorescence intensity, which can be applied for the real quantitative H_2S sensing.

As most of these "turn-on" assays were conducted in a suspension system, where the solid-state nitro-functionalized MOFs were dispersed in NaHS/Na_2S solutions, the fluorescence obtained was actually attributed to the combined effects of real fluorophores and non-luminescent particles in the suspension. Even though researchers ascribed the fluorescence enhancement in suspension to the formation of NH_2-functionalized MOFs, the direct evidence of -NH_2 existence within the MOFs after H_2S treatment is still lacking. In addition, misinterpretation of fluorescent signals may also arise for the following reasons. 1. The precipitation of undissolved particles in suspension will change the pathway of excitation radiation, which further leads to the fluctuations of fluorescence intensity; 2. The irradiation could be absorbed by the non-luminous undissolved particles in the suspensions, which makes the effective light for the absorption of real fluorophores decrease. This phenomenon is called the inner-filter effect, and the existence of high concentrations of non-luminous undissolved particles could reduce the fluorescence intensity; 3. Except for the absorption, the irradiation light is also scattered in all directions from the small molecules in the suspensions. In a case of a suspension with a small Stokes shift, the broad scattering peak near the excitation wavelength sometimes may overlap with the emission peak, which makes the fluorescence intensity from fluorophores challenging to separate. Therefore, it is sometimes difficult to identify the real fluorophores in such a complex suspension system.

To further explore the mechanism of the "turn-on" effect, Al-MIL-53-NO_2 was utilized in

this study to react with H_2S in an aqueous system. Furthermore, the supernatant and the undissolved particles were isolated for the first time to locate the possibly formed -NH_2 groups. Meanwhile, the effect of the undissolved MOF particles on the fluorescence intensity in the sensing application was also analyzed. Interestingly, after being treated by H_2S (0.1-1.0 mM), the undissolved nanoparticles remained in the suspension were proved to be Al-MIL-53-NO_2 rather than Al-MIL-53-NH_2 and no -NH_2 groups were formed at the surface of the residual solids, which made no contribution to the fluorescence enhancement. The fluorescence "turn-on" effect was actually caused by the free BDC-NH_2 in the solution, which was reduced from BDC-NO_2 in the collapse of Al-MIL-53-NO_2 when exposed to H_2S. With the existence of fluorophore BDC-NH_2 in an aqueous system, both supernatant (limit of detection, LOD = 69.7 μM) and suspension (i.e., Al-MIL-53-NO_2 particles were dispersed evenly in aqueous solutions of NaHS by ultrasonication) (LOD = 69.3 μM) can be used to realize quantitative H_2S sensing within 0-0.7 mM H_2S. The result of this work unravels the origin of "turn-on" effect of Al-MIL-53-NO_2 in H_2S sensing and explores the new ways (separation of suspension into supernatant and undissolved residues) of fluorophore tracing in MOF-based detection.

3.2 Materials and Methods

Chemicals Sodium hydrosulfide hydrate ($NaHS \cdot xH_2O$, ~70%), 2-nitrobenzene-1,4-dicarboxylic acid ($C_8H_5NO_6$, BDC-NO_2, ≥99%), 2-aminobenzene-1,4-dicarboxylic acid ($C_8H_7NO_4$, BDC-NH_2, ≥99%) and aluminum chloride hexahydrate ($AlCl_3 \cdot 6H_2O$, ≥99%) were obtained from Sigma Aldrich. N-dimethylformamide ($HCON(CH_3)_2$, DMF) was purchased from VWR Corporation. Ethanol (C_2H_5OH, 190 proof) was obtained from Gold Shield. Deionized (DI) water was used to prepare solutions. All chemicals were used without further purification.

Synthesis of Al-MIL-53-NO_2 Al-MIL-53-NO_2 nanoparticles were synthesized according to the

previous reference. [138] Typically BDC-NO_2 (42.2 mg, 0.2 mmol) was dissolved in 10 ml DMF by sonication for 1 minute. Then $AlCl_3.6H_2O$ (48.3 mg, 0.2 mmol) with an above solution was transferred into a 25 ml Teflon lined steel autoclave and heated at 180 °C for 12 hours. The obtained yellow particles were separated by centrifugation at 10000 rpm for 10 minutes and washed with 15 ml DMF and 15 ml ethanol three times to remove unreacted chloride species and BDC-NO_2. Finally, the collected particles were dried in air at 200 °C for 6 hours to completely remove the attached DMF molecules.

Synthesis of Al-MIL-53-NH_2 Al-MIL-53-NH_2 was prepared based on a reported recipe.[106] $AlCl_3.6H_2O$ (1.45g, 6.0 mM) and 2-aminobenzene-1,4-dicarboxylic acid (BDC-NH_2) (1.1g, 6.0 mM) were mixed in 30 ml DMF and then kept in the 100 ml Teflon lined steel autoclave at 150 °C for 5 hours. After being cooled to room temperature, the obtained yellow particles were washed with 15 ml DMF and 15 ml ethanol three times. The as-synthesized Al-MIL-53-NH_2 has activated in 60 ml DMF solution at 155 °C for 24 hours and then heated in air at 155 °C for 24 hours.

Materials characterization The morphologies of the samples were analyzed using a scanning electron microscope (SEM) with energy disperse X-ray (EDX) spectroscopy (Su-70, Hitachi). The structure and crystallinity of Al-MIL-53-NO_2 were determined by powder X-ray diffraction (PXRD) (PANalytical X'Pert Pro MPD). The analysis of vibrations of functional groups was carried out with a Fourier transform infrared (FT-IR) spectrometer (Nicolet iS50, Thermo Scientific). Photoluminescence properties of the samples were characterized by a fluoroscence spectrometer (PTI QuantaMaster-400). X-ray photoelectron spectroscopy (XPS) measurement was conducted with a Thermo Scientific ESCALAB 250 to investigate the chemical state of the element on the surface of Al-MIL-53-NO_2. The pore size and surface area of the Al-MIL-53-NO_2

were measured by using Autosorb iQ (Quantachrome Instruments).

H_2S Fluorescence Sensing Measurements NaHS was used as the H_2S source and dissolved in DI water to form a transparent solution. [132, 133, 138] In this paper, "H_2S treated" or "H_2S treatment" means Al-MIL-53-NO_2 is suspended in NaHS solution with a specific concentration. In a typical experiment, 1.5 mg Al-MIL-53-NO_2 was suspended into the cuvette containing 3.0 ml of NaHS solution with various concentrations (0.0-5.0 mM) for 2 hours before centrifugation. The corresponding supernatant and the suspended undissolved particles were separated by centrifugation at 12000 rpm for 10 minutes. The re-collected particles were washed with water three times and re-dispersed into 3.0 ml DI water for further photoluminescence measurement. For all the fluorescence measurements, the excitation wavelength (λ_{ex}) was 339 nm, and the emission spectra were recorded in the range of 380-580 nm. Both emission and excitation slits were set to be 2 nm.

3.3 Results and Discussions

The crystallinity and structure of Al-MIL-53-NO_2 were determined by PXRD. As shown in **Figure 3.1a**, all the peaks are well consistent with those reported in the previous references, where Al-MIL-53-NO_2 has a monoclinic crystal structure.[138, 140, 141] The main peak was located at ~8.5°, which is ascribed to the (100) plane.[140] The crystals and morphologies were also characterized by scanning electron microscopy (SEM). It is found that the Al-MIL-53-NO_2 powders are composed of irregular nanoparticles with sizes ranging from 20 nm to 300 nm (**Figure 3.1b**), which is also similar to what was reported previously.[138] In addition to the crystallinity and morphology, vibration analysis of surface functional groups was directly carried out by FT-IR. The absorption peak at 1542 cm^{-1} (**Figure 3.1c**) originated from the N=O stretching vibration of the nitro groups attached to the coordinated ligands, which demonstrated

the successful incorporation of the -NO_2 group into the MOF crystals.[134] The strong absorption bands at 1421 cm^{-1} and 1619 cm^{-1} are attributed to the symmetric and asymmetric -CO_2 stretching vibrations from the coordinated BDC-NO_2 linkers, respectively. It should be noted that the small peak at 3662 cm^{-1} is ascribed to the μ_2-OH group.[140] The porosity of Al-MIL-53-NO_2 was further confirmed by the N_2 sorption measurements at 77 K. As shown in **Figure 3.1d,** the rapid increase in the low relative pressure regions demonstrated the existence of micropores in Al-MIL-53-NO_2. The surface area of Al-MIL-53-NO_2 based on the Brunauer–Emmett–Teller (BET) theory was calculated to be 1163 m^2 g^{-1}, which provides large numbers of active sites to interact with H_2S in the sensing process.[142, 143] Overall, the above results indicated that the Al-MIL-53-NO_2 has been synthesized successfully.

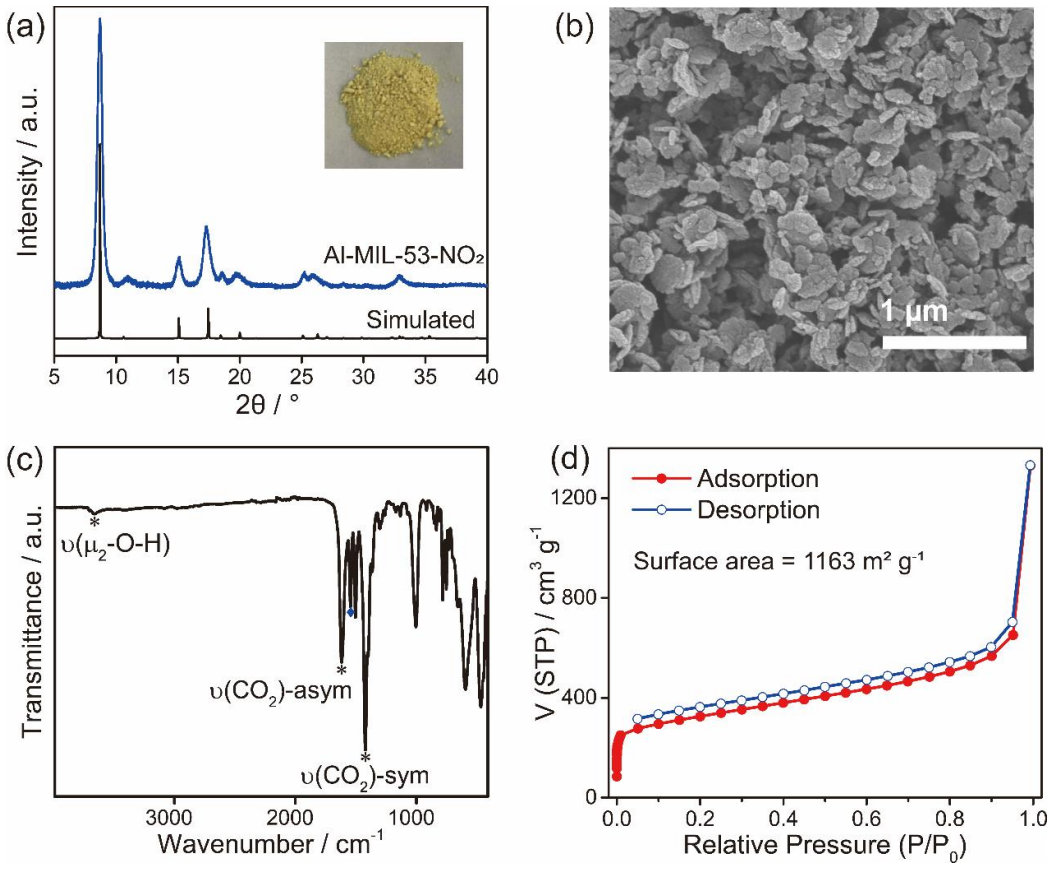

Figure 3.1 (a) PXRD patterns and digital image (inset), (b) SEM image, (c) FT-IR spectrum, and (d) gas sorption isotherms of Al-MIL-53-NO_2 nanoparticles.

The detection capability of Al-MIL-53-NO_2 for H_2S was investigated by performing a fluorescence "turn-on" experiment in the aqueous suspension system. NaHS was used as a source of H_2S in this study.[133, 138] Owing to the existence of electron-withdrawing nitro groups in the coordinated BDC-NO_2 ligand, Al-MIL-53-NO_2 is non-luminous and remains in the fluorescence "turn-off" state. [138] Once exposed to H_2S, -NO_2 would be reduced to electron-donating -NH_2 groups, and the fluorescence enhancement was presented based on the following reaction:

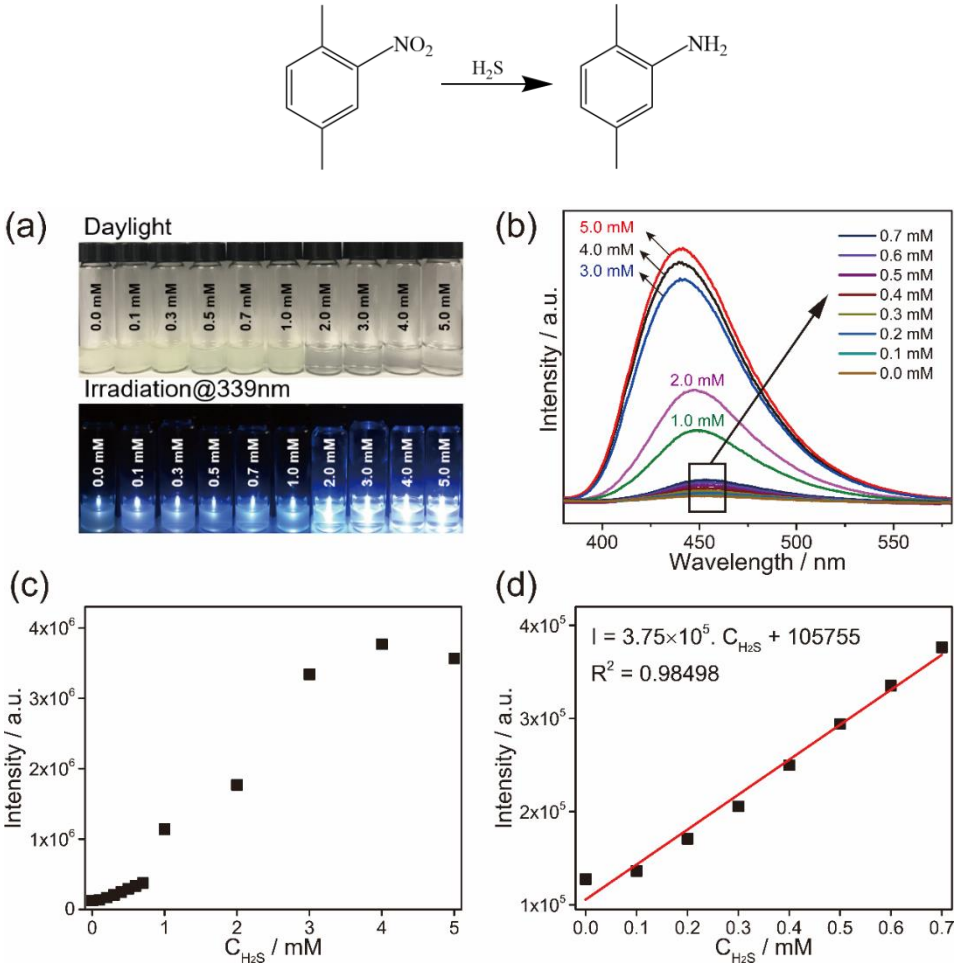

Figure 3.2 (a) Digital images of Al-MIL-53-NO_2 suspensions with various NaHS concentrations under visible light (up) and UV light (339 nm, down); (b) Emission spectra of Al-MIL-53-NO_2 suspensions with various NaHS concentration (Excitation wavelength: 339 nm); (c and d) Emission intensity versus NaHS concentration.

For H_2S sensing quantification, 1.5 mg Al-MIL-53-NO_2 was suspended in 3 ml DI water with various NaHS concentrations from 0.0 mM to 5.0 mM. To ensure the complete conversion of -NO_2 to -NH_2 in the sensing process, the suspension was kept in the sealed glass vial for 2 hours and then shaken to form the uniform suspension for photoluminescence measurement. The excitation wavelength was determined at 339 nm by scanning 1.0 mM H_2S treated Al-MIL-53-NO_2 suspension from 380 nm to 580 nm, with the maximum emission peak at 450 nm. All the fluorescence emission spectra were recorded from 380 nm to 550 nm at the excitation wavelength of 339 nm in this study. It is found that the H_2S showed a significant "turn-on" response to the Al-MIL-53-NO_2 suspensions (**Figure 3.2(a-c)**). An excellent linear correlation (R^2 = 0.98498) was obtained between the fluorescence intensities and H_2S concentrations within 0.7 mM (**Figure 3.2d**). Moreover, the limit of detection (LOD) was calculated to be 69.3 μM, which indicated that Al-MIL-53-NO_2 can be used for quantitative detection of H_2S in the aqueous suspension system. It is noteworthy that the fluorescence intensity was vastly enhanced when the H_2S concentration was larger than 1.0 mM and tended to be constant within the range from 2.0 mM to 5.0 mM. The possible mechanisms for such a significant "turn-on" fluorescence increment will be discussed next.

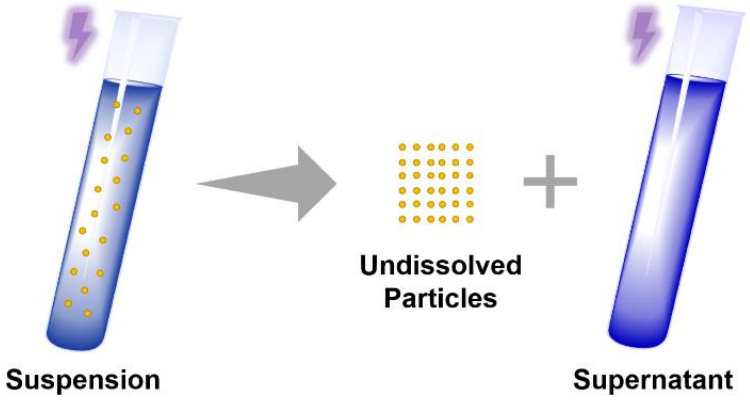

Scheme 3.1. Undissolved particles and supernatant were separated by centrifugation for further analysis.

Most studies ascribed the "turn-on" effect to the conversion of -NO_2 to -NH_2 groups by "MOF transformation" and fluorescence signals of MOFs in the suspension were used for quantitative H_2S detection. Few researchers separated the undissolved particles to give direct evidence of -NH_2 groups on the surface of MOF after being exposed to H_2S. In order to determine whether the luminescence enhancement comes from the -NH_2 groups in MOF or the free ones in the solution, the suspensions were centrifuged at 12000 rpm for 10 minutes to separate the undissolved particles and supernatant for further analysis (see **Scheme 3.1**). The exploration of such a "Turn-On" effect will be carried out by analyzing both undissolved nanoparticles and supernatant.

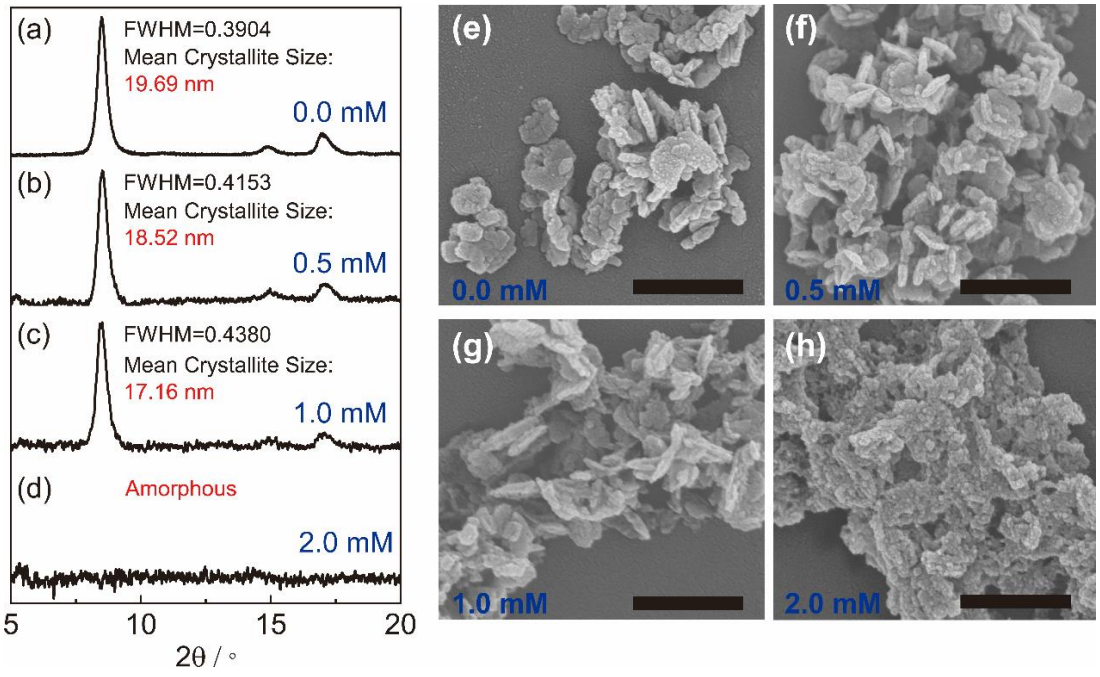

Figure 3.3 PXRD patterns and SEM images of undissolved nanoparticles collected from Al-MIL-53-NO_2 suspensions with various NaHS concentrations: 0.0 mM (a, e), 0.5 mM (b, f), 1.0 mM (c, g), and 2.0 mM (d, h). The scale bar for (e-h) is 500 nm.

The undissolved nanoparticles separated from the suspensions were washed with DI water three times and dried in the air at 120 °C for two hours to remove water molecules. The 0.5

mM and 1.0 mM H_2S treated Al-MIL-53-NO_2 were characterized by PXRD. The PXRD patterns matched well with the pristine Al-MIL-53-NO_2 nanoparticles and no apparent phase of as-synthesized Al-MIL-53-NH_2 was observed. According to the Scherrer equation,

$$\tau = \frac{K\lambda}{\beta \cos\theta} \tag{3.1}$$

where τ is the mean size of the crystallite; K is the dimensionless shape factor (K=0.89); λ is the X-ray wavelength (λ = 1.5406 Å); β is the line broadening at the maximum intensity (FWHM); θ is the Bragg angle, it is found that with H_2S concentration increased from 0.0 mM to 0.5 mM, and 1.0 mM, the FWHM (Full Width at Half Maximum) of the peak at 8.5° becomes broader and the corresponding calculated mean crystallite size within (100) domain is reduced from 19.69 nm to 18.52 nm, and 17.16 nm, respectively (**Figure 3.3(a-c))**. The minor shrinkage of Al-MIL-NO_2 crystals could be caused by the original Al-MIL-53-NO_2 being degraded from the outer to the core, where the peripheral bridged Al-O bonds were broken in the alkaline NaHS solution. [144] Similar morphologies of recollected Al-MIL-53-NO_2 nanoparticles treated by 0.5 mM and 1.0 mM H_2S compared to the pristine Al-MIL-53-NO_2 (**Figure 3.3(e-g)**) confirmed that the residual Al-MIL-53-NO_2 nanoparticles kept the same shapes within 1.0 mM H_2S treatment. When the H_2S concentration came to 2.0 mM, the initial Al-MIL-53-NO_2 crystalline materials were collapsed, and an amorphous PXRD pattern was obtained (**Figure 3.3d**). The large crystals disappeared, leaving much smaller amorphous particles, as shown in **Figure 3.3h**. Interestingly, similar peak broadening phenomena were also observed in other nitro-functionalized MOFs (Zr-UiO-66-NO_2, Ce-UiO-66-NO_2, and Zr-UiO-66-$(NO_2)_2$) during H_2S detection,[28, 84, 132] which indicated that all these MOFs could be partially consumed and the particle sizes became smaller after being treated by H_2S. The particles with reduced crystal size and the released species into the solution could cause a dramatic change in the fluorescence intensity, which will be further

discussed using Al-MIL-53-NO_2 in the next section.

The functional groups of undissolved Al-MIL-53-NO_2 nanoparticles treated by 0.5 mM and 1.0 mM H_2S were analyzed by an FT-IR spectrometer. Two major peaks were observed for Al-MIL-53-NH_2 at 3387 and 3499 cm^{-1}, corresponding to symmetric and asymmetric N-H stretching vibration, respectively. However, no apparent peaks were observed for the undissolved particles, which indicated that -NO_2 on undissolved Al-MIL-53-NO_2 nanoparticles were not reduced to the -NH_2 after H_2S sensing.

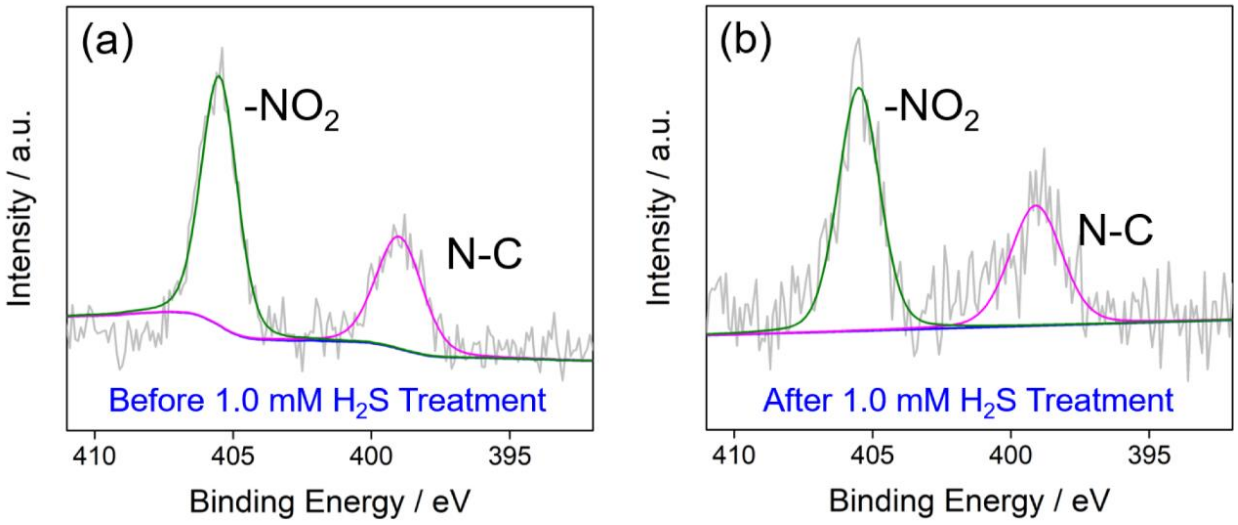

Figure 3.4 High-resolution spectra of N 1s of Al-MIL-53-NO_2 before (a) and after (b) being treated by 1.0 mM H_2S.

The Al-MIL-53-NO_2 before and after 1.0 mM H_2S treatment was further analyzed by X-ray photoelectron spectroscopy (XPS). Herein, the as-synthesized Al-MIL-53-NH_2 was used for comparison. The high-resolution N 1s spectrum of Al-MIL-53-NH_2 exhibits two peaks at 399.3 eV and 398.5 eV, which can be assigned to C-N bonds and NH_2 groups, respectively. [145] For pristine Al-MIL-53-NO_2 without being exposed to 1.0 mM H_2S, peaks of binding energy at ~532 eV, ~405 eV, ~285 eV, ~119 eV, and ~74 eV are ascribed to C 1s, N 1s, O 1s, Al 2s, and Al 2p,

respectively. All the peaks can still be found in the recollected Al-MIL-53-NO_2 nanoparticles at the same position after 1.0 mM H_2S treatment. Moreover, for pristine Al-MIL-53-NO_2, the high-resolution spectrum of N 1s can be divided into two peaks located at 399.1 eV and 405.5 eV (**Figure 3.4a**), which are attributed to N-C and –NO_2 groups within the Al-MIL-53-NO_2, respectively.[146] After being exposed to 1.0 mM H_2S, no other peaks related to N 1s appeared (**Figure 3.4b**) and the ratio of peak area of N-O to C-N remained almost the same (Before: 1.71:1; After 1.62:1), indicating that undissolved Al-MIL-53-NO_2 nanoparticles in 1.0 mM H_2S solution shared similar surface chemical properties with the pristine unreacted Al-MIL-53-NO_2.

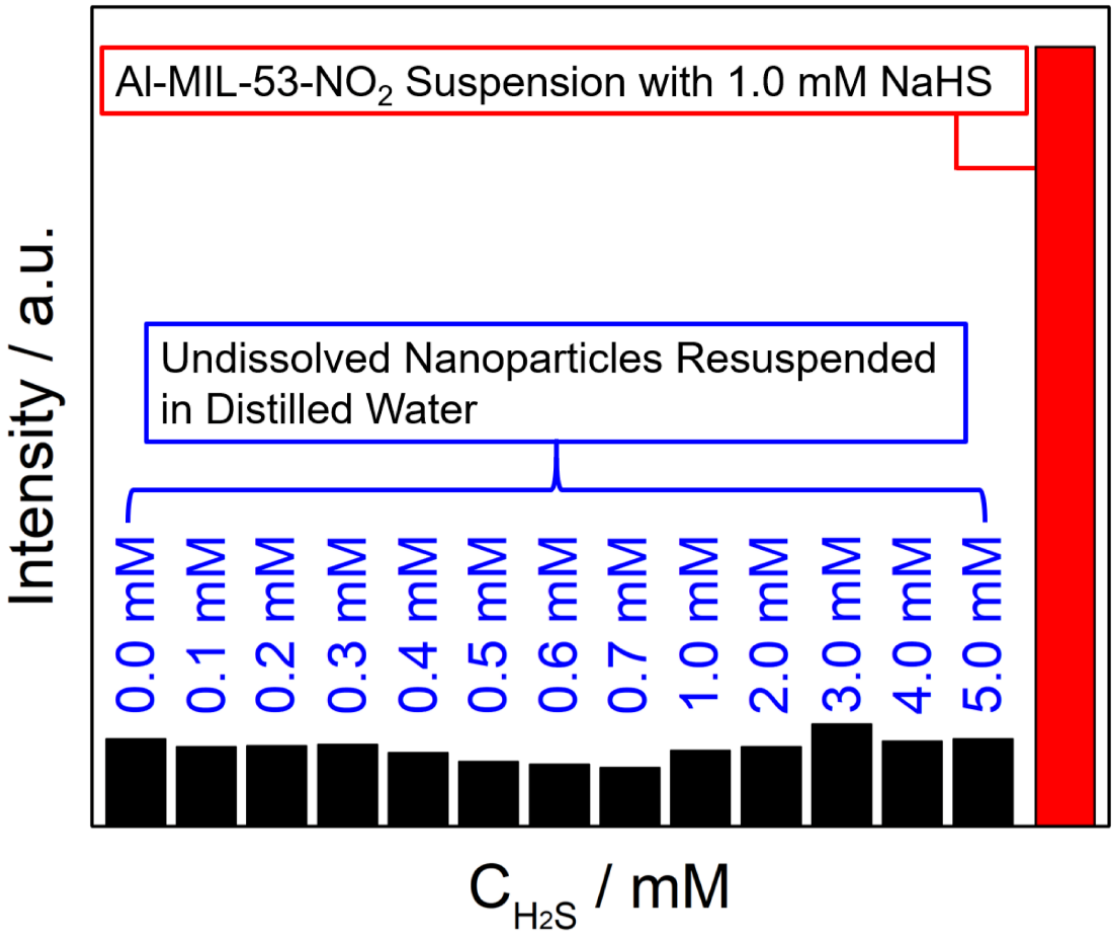

Figure 3.5 Emission intensities at 450 nm (excitation wavelength: 339 nm) of aqueous solutions of undissolved nanoparticles (treated by 0.0 mM to 5.0 mM H_2S) (black columns) and Al-MIL-53-NO_2 suspension with 1.0 mM NaHS (red column).

Additionally, the recollected Al-MIL-53-NO_2 nanoparticles after interaction with various concentrations of H_2S were resuspended into 3.0 ml DI water for further photoluminescence measurement. It turns out that all the undissolved Al-MIL-53-NO_2 nanoparticles dispersed in water showed no fluorescence intensity and stayed in the "turn-off" mode (**Figure 3.5**), which further confirmed that there were no -NH_2 groups at the surface of the undissolved H_2S-treated Al-MIL-53-NO_2 nanoparticles.

Overall, the recollected particles from the H_2S treatment suspension were analyzed by XRD, SEM, FT-IR, PL, and XPS, and these nanoparticles were proved to be almost identical to the unreacted Al-MIL-53-NO_2 (0.1-1.0 mM). In addition, there were no -NH_2 groups attached to these remained Al-MIL-53-NO_2 based on the FT-IR and XPS data, indicating that -NO_2 on the surface of Al-MIL-53-NO_2 was not converted to -NH_2. Therefore, it can be concluded that these remained unreacted suspended Al-MIL-53-NO_2 particles make no contribution to the fluorescence enhancement in the H_2S sensing process.

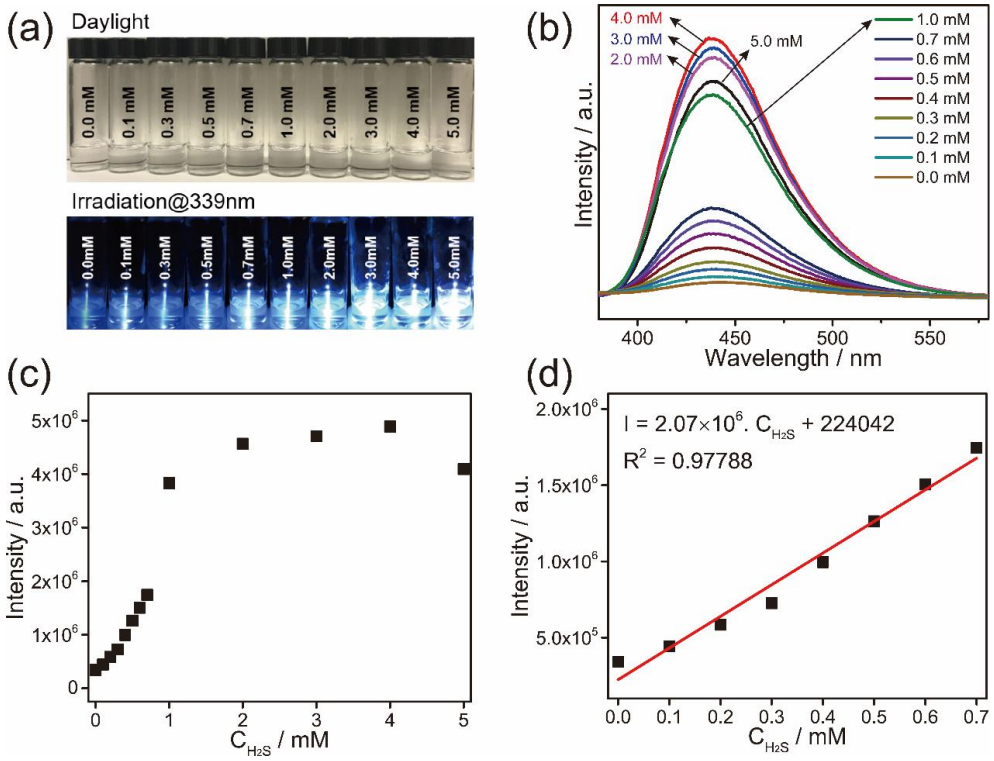

Figure 3.6 (a) Digital images of Al-MIL-53-NO_2 supernatants separated from Al-MIL-53-NO_2 suspensions with various NaHS concentrations under visible light (up) and UV light (339 nm, down); (b) Emission spectra of Al-MIL-53-NO_2 supernatants from Al-MIL-53-NO_2 supernatants with various NaHS concentrations (Excitation wavelength: 339 nm); (c and d) Emission intensity versus NaHS concentration.

Since the fluorescence enhancement in the initial suspension system does not come from the undissolved Al-MIL-53-NO_2 nanoparticles treated by H_2S, isolated supernatants were used for further analysis. Photoluminescence properties of isolated supernatants were measured and the fluorescence enhancement was also observed under the supernatant system (**Figure 3.6(a-c)**). It is interesting to find that a good linear relationship was also obtained within 0.7 mM, and the LOD of H_2S detection with supernatant was calculated to be 69.7 μM (**Figure 3.6d**), which indicated that the supernatant could be used to realize quantitative H_2S sensing as well.

To analyze the fluorophores in the supernatant, the transparent supernatant from 1.0 mM H_2S treated Al-MIL-53-NO_2 suspension was heated at 120 °C in the air to evaporate the solvent and the extracts were characterized by FT-IR. The sodium 2-aminoterephthalate, which serves as the real fluorophore in the solution, was detected in the FT-IR spectrum of the residues.[147] The broad peak with a maximum at 3370 cm^{-1} can be assigned to the amino groups that interacted with the metal sodium after evaporation.[147, 148] The completely deprotonated asymmetric and symmetric COO^- vibrations were observed at 1590 cm^{-1} and 1371 cm^{-1}, respectively. [147] Moreover, a tiny amount of -NO_2 groups was also detected, indicating the BDC-NO_2 from Al-MIL-53-NO_2 existed in the supernatant after 1.0 mM H_2S treatment. Considering no -NH_2 groups were observed on the undissolved Al-MIL-53-NO_2 nanoparticles, these results suggest that the linker BDC-NO_2 was first released because of the Al-MIL-53-NO_2 degradation in the solution and then reduced to BDC-NH_2 by H_2S treatment. Such partially structural

decomposition of the initial Al-MIL-53-NO_2 (Al-($OOC-NO_2^-$)) → Al-OH^- + NO_2-COO^- (BDC-NO_2)) could stem from the replacement of linkers by hydroxide ions (OH^-) which competitively bind to the metal cations from MOF clusters in the NaHS basic solution.[144, 149] The conversion of -NO_2 to -NH_2 that occurs in the solution rather than on the MOF is probably because the free BDC-NO_2 in aqueous is more easily reduced by NaHS while the center of Al-O clusters in solid-state Al-MIL-53-NO_2 increase the resistance towards NaHS attack. Therefore, it can be concluded that towards H_2S treatment, the part of the Al-MIL-53-NO_2 was collapsed and the released BDC-NO_2 has been reduced to BDC-NH_2, which gave rise to the fluorescence "turn-on" effect. (**Scheme 3.2**)

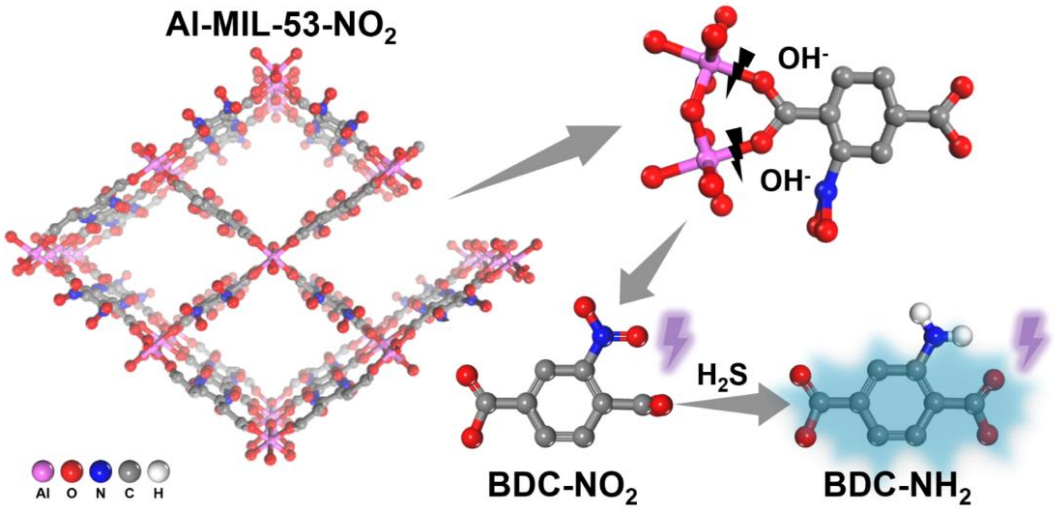

Scheme 3.2 Schematic illustration of Al-MIL-53-NO_2 for H_2S sensing.

The results of the above supernatant analysis matched well with the peak broadening in the XRD pattern as discussed in the previous section. The remaining particles with reduced crystal size and the released fluorophores in the solution could also have an effect on the fluorescence signal. It is noteworthy that, for Al-MIL-53-NO_2 treated by 1.0 mM H_2S, a much greater fluorescence intensity at 450 nm of supernatant was achieved as compared to that of

suspension (**Figure 3.7a**). Such an enhancement of the emission of supernatants can also be observed for Al-MIL-53-NO_2 upon the treatment of H_2S with other concentrations. The reduced fluorescence of suspension as compared to supernatant is mainly caused by the unreacted non-luminescent Al-MIL-53-NO_2 dispersed in the aqueous system. The existence of unreacted Al-MIL-53-NO_2 would absorb and scatter the incident excitation light and hence decrease the photoluminescence intensity.[150] To further understand the emission difference between the supernatant and suspension, we define the relative reduction (η) as the ratio of fluorescence intensity difference between supernatant and suspension to that of suspension,

$$\eta = \frac{I_{sup} - I_{sus}}{I_{sus}} \tag{3.2}$$

where I_{sup} is the fluorescence intensity of suspension; I_{sup} is the fluorescence intensity of supernatant (**Figure 3.7a**). As shown in **Figure 3.7b**, η increased from 2.25 at 0.1 mM (H_2S) and reached the maximum 3.64 at 0.7 mM (H_2S) and then decreased with further increment of H_2S concentration until the minimum 0.15 was obtained at 5.0 mM. Such variations of the relative reduction (η) could be explained by the consumption of Al-MIL-53-NO_2 in the H_2S sensing process. When the H_2S concentration was less than 0.7 mM, only a small amount of Al-MIL-53-NO_2 was consumed, so the scattering effect of the rest of the Al-MIL-53-NO_2 in the suspension system (0.1-0.7 mM) was almost the same. Therefore, with more interaction with H_2S (0.1-0.7 mM), more corresponding reaction product BDC-NH_2 being released into the solution and the linear relationship was kept from 0.1 mM to 0.7 mM (**Figure 3.2c**), considering the scattering could be ignored. When Al-MIL-53-NO_2 being exposed to 1.0 mM H_2S, more initial Al-MIL-53-NO_2 has collapsed and the scattering effect was sharply weakened, so the much larger fluorescence enhancement in suspension system was obtained and the linear relationship between the fluorescence intensity and H_2S concentration cannot be maintained (**Figure 3.2c**).

This “turning point” was also reflected in the sharp reduction in η from 3.64 at 0.7 mM to 2.36 at 1.0 mM (**Figure 3.7b**). For 2.0-5.0 mM H_2S treatment suspensions, the initial Al-MIL-53-NO_2 was completely destroyed and the corresponding suspensions became more transparent (**Figure 3.2a**), indicating the scattering effect in this range could be neglected. Therefore, η tends to be stable and extremely small after being exposed to 2.0-5.0 mM H_2S (**Figure 3.7b**).

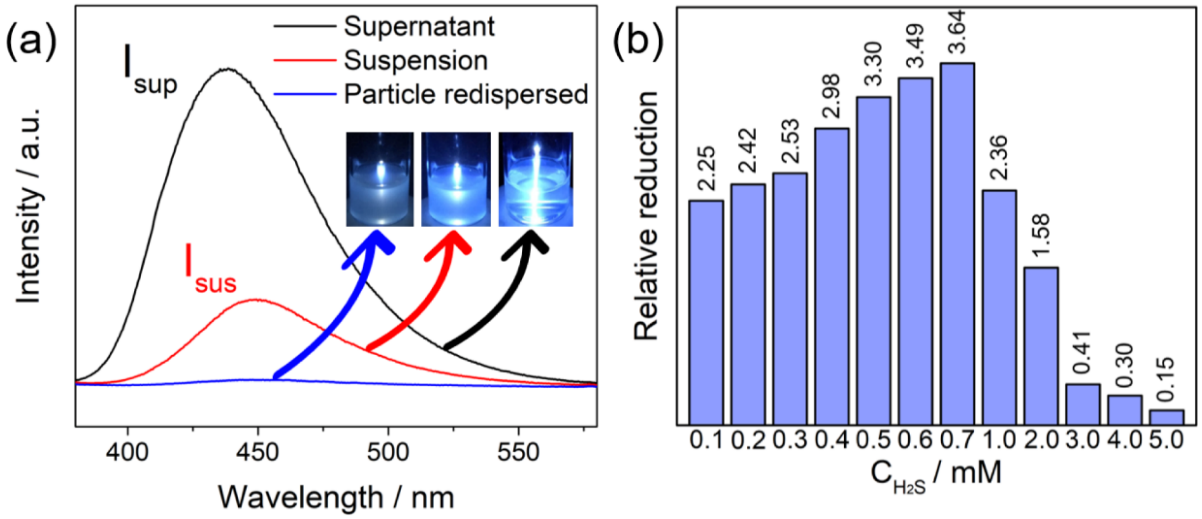

Figure 3.7 (a) Emission spectra (monitored at 339nm) of Al-MIL-53-NO_2 suspended in 1.0 mM NaHS solution (black line), Al-MIL-53-NO_2 supernatant separated from 1.0 mM NaHS treated Al-MIL-53-NO_2 suspension (red line), undissolved particle separated from 1.0 mM NaHS treated Al-MIL-53-NO_2 suspension re-dispersed in aqueous solution (blue line); (b) The relative reduction in fluorescence intensity of Al-MIL-53-NO_2 treated by various NaHS concentration.

3.4 Conclusions

In summary, the photoluminescence properties of Al-MIL-53-NO_2 for H_2S sensing have been systematically analyzed in both suspensions and supernatant system. The mechanism of Al-MIL-53-NO_2 probe for H_2S detection was unraveled that the fluorescence enhancement was ascribed to the BDC-NH_2 reduced from BDC-NO_2 in the collapse of Al-MIL-53-NO_2 exposed to H_2S. The undissolved nanoparticles treated by 0.1-1.0 mM H_2S were proved to be Al-MIL-53-

NO_2 rather than Al-MIL-53-NH_2 with XRD, FT-IR, and XPS measurements and these non-luminescence nanoparticles make no contribution to the fluorescence enhancement in “turn-on” process. In particular, both suspension (LOD = 69.3 μM) and supernatant (LOD = 69.7 μM) can be used for H_2S quantitative detection within 0-0.7 mM. This work provides new insight into the ways of fluorophore location exploration in probe-consuming sensing applications.

Chapter 4. Self-Decontaminating Nanofibrous Filters for Efficient Particulate Matter Removal and Airborne Bacteria Inactivation

Environmental Science: Nano, 8(4), 1081-1095. (2021)

DOI: 10.1039/D0EN01230K

Abstract

With the increased bacteria-induced hospital-acquired infections (HAIs) caused by bio-contaminated surfaces, the requirement for a safer and more efficient antibacterial strategy in designing personal protective equipment (PPE) such as N95 respirators is rising with urgency. Herein, a self-decontaminating nanofibrous filter with a high particulate matter (PM) filtration efficiency was designed and fabricated via a facile electrospinning method. The fillers implemented in the electrospun nanofibers were constructed by grafting a layer of antibacterial polymeric quaternary ammonium compound (QAC), that is, poly [2-(dimethyl decyl ammonium)ethyl methacrylate] (PQDMAEMA), onto the surface of metal-organic framework (MOF, UiO-66-NH_2 as a model) to form the active composite UiO-PQDMAEMA. The UiO-PQDMAEMA filter demonstrates an excellent PM filtration efficiency (> 95%) at the most penetrating particle size (MPPS) of 80 nm, which is comparable to that of the commercial N95 respirators. Besides, the UiO-PQDMAEMA filter is capable of efficiently killing both Gram-positive (*S. epidermidis*) and Gram-negative (*E. coli*) airborne bacteria. The strong electrostatic interactions between the anionic cell wall of the bacteria and positively charged nitrogen of UiO-PQDMAEMA are the main reasons for severe cell membrane disruption, which leads to the death of bacteria. The present work provides a new avenue for combating air contamination by using the QAC-modified MOF-based active filters.

4.1 Introduction

Hospital-acquired infections (HAIs), also known as health-associated infections, have been recognized as a major threat to the safety of patients and healthcare workers worldwide.[151-155] During the COVID-19 pandemic, numerous cross-infections occurred in the hospitals among healthcare workers and patients, indicating that the adverse effects of HAIs such as mortality, morbidity, and associated costs are enormous.[156] To reduce the HAIs, face-piece respirators such as N95 respirators and surgical masks are recommended by the United States Centers for Disease Control and Prevention (CDC) as efficient respiratory personal protective equipment (PPE).[157-159] For convenience, the term 'face mask' is used to represent N95 respirators and surgical masks throughout the article. Even though the commercial face masks can provide users with certain degree of protection, there are still intensive researches and efforts to improve their performance in terms of particulate matter (PM) filtration, user-friendliness, and airborne pathogens inactivation.[160-162]

Electrospinning producing nanofibers from a polymer solution is an efficient technique to fabricate filter media with high PM filtration performance, attributing to the small diameters of the nanofibers and fiber charges.[163-167] To further increase the functionality, e.g., hydrophobicity, breathability, toxic gas removal, etc., of the electrospun filters, metal-organic frameworks (MOFs), a class of porous crystalline polymers, have been embedded into the electrospun polymer to form the MOF-based filters.[79, 168-172] Endorsed by the hierarchical structures and tunable surface chemistry, the MOF-based nanofiber filters not only possess different functionalities but also achieve a high PM filtration efficiency and a lower pressure drop[36, 168] which is beneficial to the wearer's comfort in breathing. However, most of these MOF-based filters cannot be used to actively kill microorganisms such as bacteria. To impart the antibacterial

properties to the MOF-based filters, the key is to develop a fabrication method for filters with high efficiency for the simultaneous removal of PM and inactivation of bacteria.

Bacteria pathogens are one of the major infectious agents that cause the persistence of HAIs.[173] Indirect contact with contaminated surfaces and airborne droplets are two of the most common modes of bacteria transmission.[174] Most commercial face masks and electrospun MOF-based filters can only passively block the transmission of airborne bacteria but not be able to kill them *in-situ*, i.e., on the mask surface. The bacteria being captured by the face mask may accumulate on the mask surface and can still survive for hours or even days, which would significantly increase the possibility of HAIs through surface contact transmission.[69, 70] Therefore, there is an urgent demand to develop antibacterial filters for face masks. This need can be achieved by incorporating antibacterial materials into face mask filters. Conventional strategies of using antibacterial agents such as Ag ions,[175] Cu ions,[176] metal oxides,[177], and photosentisizers[178] are not very suitable because most of these materials are toxic to humans and environmentally unfriendly. In particular, when people breathe, talk, cough, or sneeze, the water droplets may condense on the mask surface,[179] which might cause the release of these chemicals.[180] As a result, a safer method is demanded to impart the face mask with nonleaking and antibacterial properties.

Quaternary ammonium compounds (QACs) are potent antimicrobials that are widely used as disinfectants because of their low toxicity, the flexibility of molecule structures, the readiness of fixation on the surface, the low probability of antibiotic resistance, and so on.[181-184] The bactericidal activity of QACs stems from the electrostatic attraction between permanent positively charged nitrogen (N^+) in QACs and negatively charged bacterial membrane,[185] which would ultimately lead to cell lysis, namely the burst of cytoplasmic material.[186] In particular, the

polymeric QACs with long alkyl chains exhibited enhanced bactericidal activity because the longer alky chains can interact with the lipid cell walls more strongly and destabilize the bacterial membrane more effectively.[187] Even though the recent emerging popular "grafting from" approach, also known as "surface-initiated polymerization", has enabled the controllable grafting QACs on the material surfaces,[188] the immobilization of polymeric QACs onto the face mask filters is still challenging for the following reasons. Firstly, the surface of the filter should be pretreated by plasma or other chemical treatment to allow the fixation of the suitable initiators, which is complicated and time-consuming.[188] Secondly, the harsh organic solvents would impair the PM filtration efficiency of electret media, which is one of the most important functionalities of the face mask filter. [37, 167, 189] Therefore, how to immobilize the polymeric QACs on the face mask filters without compromising the PM filtration efficiency is a prominent quest.

To achieve this goal, this work reports a rational design approach to incorporate a QAC-modified MOF into the electrospun fibers to form an active composite filter. As an important type of MOFs, the amino-derived MOFs provide great platforms to covalently attach functional groups by post-synthetic modification. Herein, a robust UiO-66-NH_2 is used as the base material,[190, 191] which is subsequently decorated with a layer of polymeric QAC, i.e., poly [2-(dimethyl decyl ammonium)ethyl methacrylate] (PQDMAEMA) through a classical atomic transfer radical polymerization (ATRP) approach. With the assistance of the electrospinning technique, the as-synthesized active composite UiO-PQDMAEMA was embedded with the polyacrylonitrile (PAN) solution to produce an antibacterial nanofibrous filter, which also exhibits a high PM filtration performance comparable to a commercial N95 respirator (**Scheme 4.1**). The UiO-PQDMAEMA@PAN filter is capable of efficiently killing both Gram-positive (*S. epidermidis*) and Gram-negative (*E. coli*) bacteria by destroying their cell membranes,

highlighting that the UiO-PQDMAEMA@PAN can be potentially used as an antibacterial core filter for N95 respirators. We expect that this design of antibacterial filters can also be used for the fabrication of the heating, ventilation, and air conditioning (HAVC) air filter as well as the membrane for waterborne bacteria disinfection.

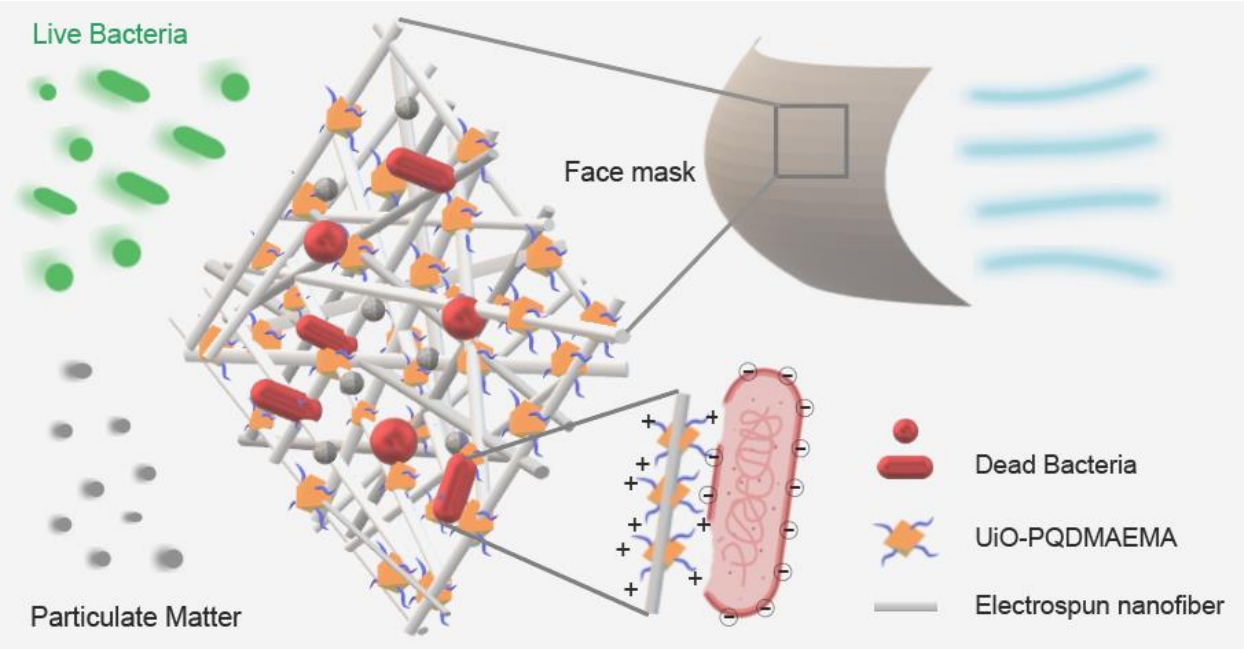

Scheme 4.1 The schematic illustration of UiO-PQDMAEMA@PAN filter towards PM capture and airborne bacteria inactivation.

4.2 Materials and Methods

Chemicals N, N, N', N'', N''-pentamethyl diethylenetriamine (PMDETA, 99%), 2-(dimethylamino)ethyl methacrylate (DMAEMA, 98%), copper (I) bromide (CuBr, 98%), copper (II) bromide ($CuBr_2$, 99%), 2-bromoisobutyryl bromide (BIBB, 98%), 1-bromodecane (98%), isopropyl ether (99%), acetonitrile (99.5%), triethylamine (TEA, 99%), 2-amino-1,4-dicarboxylic acid ($BDC\text{-}NH_2$, 99%), zirconium chloride ($ZrCl_4$, 99.5%), acetic acid (99%), silver nitrate ($AgNO_3$, 99.9%), copper nitrate trihydrate ($Cu(NO_3)_2{\cdot}3H_2O$, 99%), sodium sulfide nonahydrate ($Na_2S{\cdot}9H_2O$) and polyacrylonitrile (PAN, MW = 150,000) were purchased from

Sigma Aldrich. Anhydrous tetrahydrofuran (THF, 99.8%) was obtained from Alfa Aesar. Methanol (99.8%) and N, N-dimethylformamide (DMF, 99%) were purchased from VWR Corporation. All chemicals were used as received without further purification.

Preparation of UiO-66-NH_2, UiO-BIBB, and UiO-PQDMAEMA The synthetic procedures for UiO-PQDMAEMA preparation are schematically depicted in **Scheme 4.2**. In general, the raw UiO-66-NH_2 was first decorated with initiator 2-bromoisobutyryl bromide (BIBB) via covalent bonding to form UiO-66-BIBB. Then, the monomer 2-(dimethyl decyl ammonium) ethyl methacrylate (QDMAEMA) was polymerized and grafted on the surface of UiO-66-BIBB through the ATRP process to obtain the final product, which is denoted as UiO-PQDMAEMA. The details of material synthesis processes can be seen as follows.

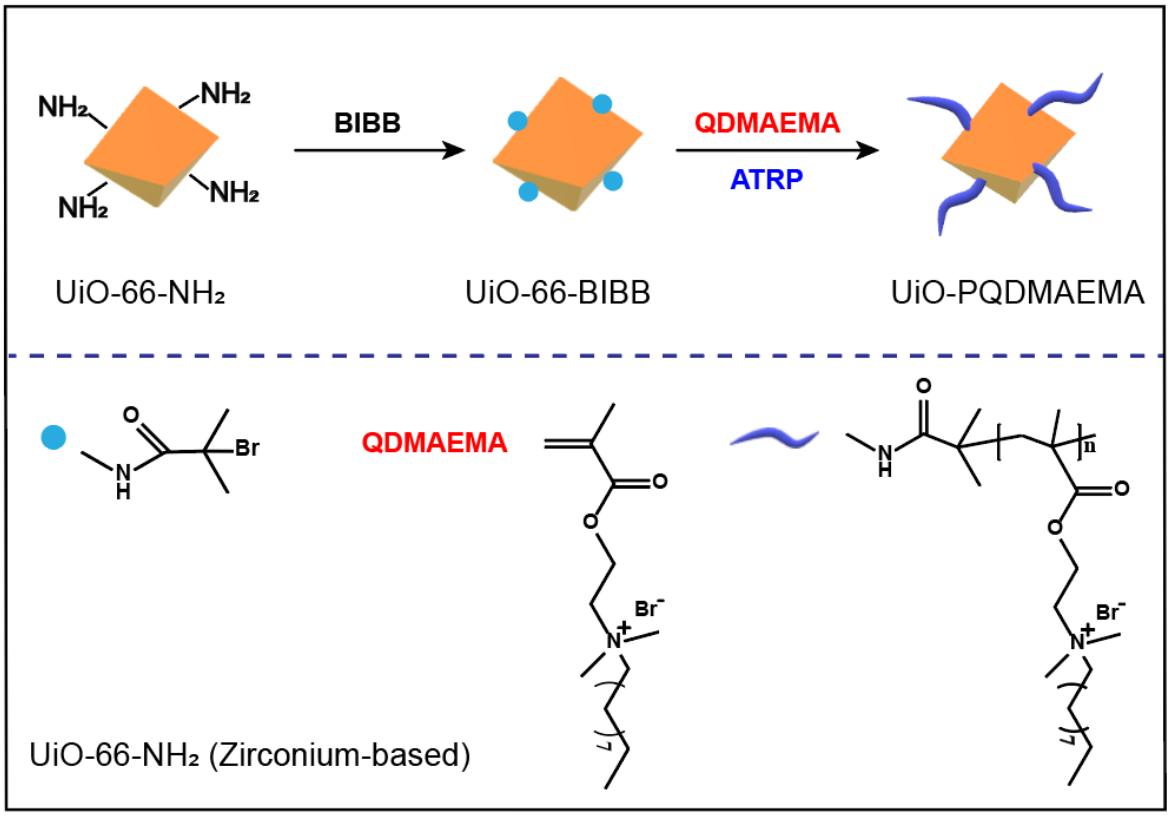

Scheme 4.2 Schematic preparation route for UiO-PQDMAEMA

Preparation of UiO-66-NH_2 UiO-66-NH_2 was prepared based on a previous work with some modifications.[192] Typically, a mixture of 0.2332g $ZrCl_4$, 0.1812g BDC-NH_2, and 6 ml acetic acid were dissolved in 50 ml DMF by ultrasonication for 5 minutes. Subsequently, the above mixture was transferred into a 100 ml Teflon-lined stainless-steel autoclave, which was kept at 120 °C for 24 hours. The obtained precipitates were washed thoroughly by DMF and methanol several times. The activation was conducted by immersing the above particles in 50 ml methanol for 72 hours. Finally, the pale-yellow particles were dried at 100 °C under vacuum for 12 hours.

Preparation of UiO-66-BIBB The UiO-66-BIBB was obtained by functionalizing UiO-66-NH_2 under the protection of nitrogen in a 50 ml flask.[190] In a typical procedure, 0.3 g UiO-66-NH_2 was suspended in 20 ml anhydrous THF by sonication. 418 μL TEA and 124 μL BiBB were dissolved in 10 ml THF separately. The TEA solution was injected into the UiO-66-NH_2 suspension under stirring. Then the BIBB solution was dropwise added into the mixture in 30 minutes with ice water cooling and strong stirring. The reactants were subsequently sealed and stirred at 50 °C for 24 hours. Finally, the particles were washed with THF and methanol and dried under vacuum at 40 °C. The obtained products were named UiO-66-BIBB.

Preparation of UiO-PQDMAEMA The typical ATRP process was conducted based on a previous work but with some modifications.[181] Poly [2(dimethyl decyl ammonium) ethyl methacrylate] (PQDMAEMA) brushes were prepared by ATRP of QDMAEMA from UiO-66-BIBB. To prepare QDMAEMA, 2.68 ml DMAEMA and 3.9 ml of 1-bromodecane were added into 10 ml acetonitrile in a 50 ml flask and reacted for 24 hours at 40 °C. After cooling to room temperature, the solution was slowly dripped into 200 ml isopropyl ether, and the white precipitates were collected by centrifugation. The precipitate was dissolved in acetonitrile and then carried on the precipitation centrifugation process for another two times. For ATRP, 0.8g

QDMAEMA and 200 µL PMDETA were added into a 10 ml mixture of deionized water and methanol (volume ratio = 1:1) in a 50 ml flask. Under the protection of nitrogen, 20 mg $CuBr_2$ and 0.2 g UiO-66-BiBB were added to the mixture. After nitrogen bubbling for 20 minutes, 64.8 mg CuBr was added into the flask, which was then tightly sealed. After stirring for 36 hours at 30 °C, the PQDMAEMA-modified UiO-66-BIBB was prepared (denoted as UiO-PQDMAEMA). The samples were separated by centrifugation and washed by deionized water and methanol for 3 times. Finally, the obtained particles were naturally dried in the air.

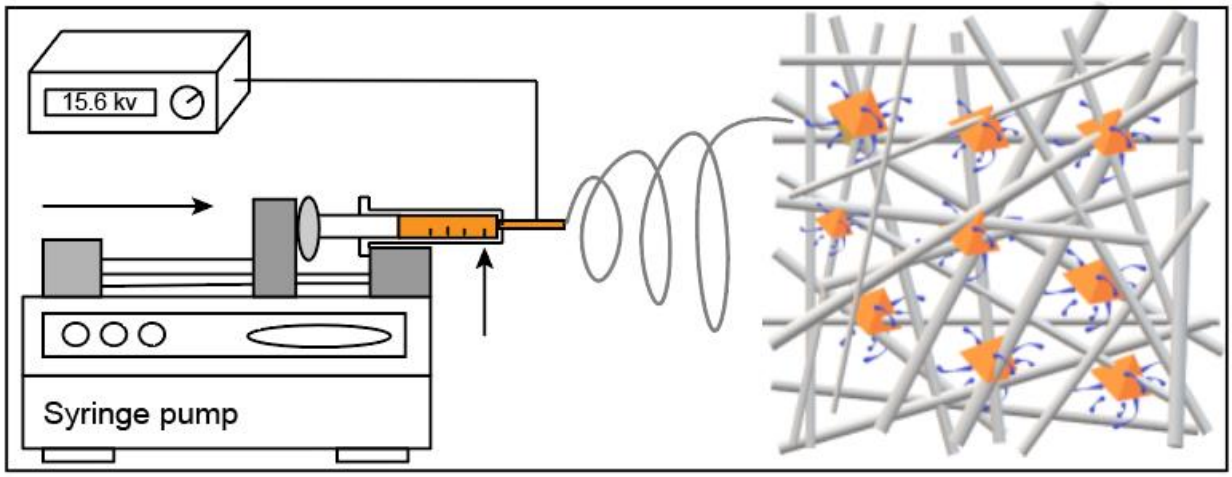

Scheme 4.3 Schematic illustration of filter fabrication by electrospinning technique.

Fabrication of Face Mask Filter The face mask filter was fabricated via the facile electrospinning method, where the electric force is generated by a high voltage to draw threads of polymer solutions to fibers with diameters in the order of hundred nanometers.[193] The experimental details are summarized here. Four different DMF (N, N-dimethylformamide) solutions of PAN (6 wt % PAN loading), UiO-66-NH_2@PAN (60 wt % MOF loading), UiO-PQDMAEMA@PAN (60 wt % UiO-PQDMAEMA loading), and Cu@PAN (60 wt % $Cu(NO)_3 \cdot 3H_2O$ loading) were used as the precursors for the nanofibers. The electrospinning process was operated at a precursor flow rate of 0.5 ml/hour. A high voltage of 17 kV was

applied and the distance between the collector and spinneret was set at 17 cm. The obtained fibers were collected on the substrate of stainless-steel mesh (from McMaster-Carr). The temperature and relative humidity (RH) were kept at 50 °C and 10%, respectively.

Materials Characterization The surface functional groups of the samples were analyzed by a Fourier transform infrared (FT-IR) spectrometer (Nicolet iS50). X-ray diffraction (XRD) patterns were collected by the PANalytical X'Pert Pro MPD. Morphologies of the samples were observed by SEM (scanning electron microscopy, Su-70, Hitachi) and TEM (transmission electron microscopy, JEOL JEM-F200). Thermogravimetric analysis (TGA) was conducted with a TA Q500 under nitrogen gas flow with a heating rate of 10 °C/min. The gas adsorption experiments were carried out using Autosorb iQ (Quantachrome Instrument). The fluorescence images were obtained by the Zeiss Axiovert 200M fluorescence microscope. The surface compositions were determined by the X-ray photoelectron spectrometer (XPS, Thermo Scientific ESCALAB 250).

Particulate Filtration Tests The particle filtration tests were conducted based on the ISO standard (ISO 21083-1:2018) for the flat sheet media and the experimental system is shown in **Figure 4.1a**.[194] The particle filtration efficiency of as-synthesized filters was tested under 9.3 cm/s face velocity which is within the media face velocity ranges in the N95 test (~5-10 cm/s).[38, 195] In brief, monodisperse sodium chloride (NaCl) particles were generated by an atomizer (TSI model 9302, TSI Inc.) and classified by a differential mobility analyzer (DMA, Model 3082, TSI Inc.) with sizes of 20, 30, 50, 80, 100, 150, 200, 300, 400, and 500 nm. Before challenging the filter media, the classified monodisperse particles were neutralized by a Po^{210} neutralizer to minimize the particle charge for mimicking the charging condition of ambient particles, which are normally in Boltzmann equilibrium.[37] An ultrafine condensation particle counter (UCPC,

Model 3776, TSI Inc.) operated at 1.5 L/min and a three-way valve were used to measure the upstream and downstream particle number concentrations of the filter media. For comparison, the filtration performance of a commercial N95 respirator from VWR (Makrite®) was also tested, in which a relatively flat portion of the respirator was cut out to form a flat sheet and the aforementioned same filtration procedure was applied.

The size-fractionated penetration, $P(d_x)$, representing the fraction of particles with diameter d_x can go through the filter medium, is defined as:

$$P(d_x) = \frac{C(d_x)_{downstream}}{C(d_x)_{upstream}} \tag{4.1}$$

where $C(d_x)_{downstream}$ and $C(d_x)_{upstream}$ are the downstream and upstream number concentrations of d_x particles, respectively. The size-fractionated filtration efficiency, $PFE(d_x)$, of the filter is thus calculated as:

$$PFE(d_x) = 1 - P(d_x) \tag{4.2}$$

The correction of $PFE(d_x)$ due to particle diffusion loss was also carried out. The upstream and downstream particle concentrations were measured for at least three times to obtain the representative filtration results. The standard deviation ($\sigma(d_x)$) was calculated using the following equation:

$$\sigma(d_x) = \frac{C(d_x)_{downstream}}{C(d_x)_{upstream}} \sqrt{\left(\left(\frac{\sigma_{downstream}}{C(d_x)_{downstream}}\right)^2 + \left(\frac{\sigma_{upstream}}{C(d_x)_{upstream}}\right)^2\right)} \tag{4.3}$$

where $\sigma_{downstream}$ and $\sigma_{downstream}$ are the standard deviations at the downstream and upstream of the filter holder, respectively.[196]

Bacteria Filtration Tests A system for bacteria filtration tests was also developed in this study (**Figure 4.1b**). Specifically, two representative bacteria *S. epidermidis* (Gram-positive) and *E. coli* (Gram-negative) suspensions with a density at 10^7 CFU/mL in phosphate-buffered saline (PBS) solution were used as precursors. Then, the suspensions were atomized by an ultrasonic nebulizer operated at 2.4 MHz to generate bioaerosols to challenge the filters at a flow rate of 12.5 L/min for 1 minute. A BioSampler (SKC Inc.) containing 20 ml sterile PBS solution was used to collect the escaped bioaerosol. After collection, the escaped bacteria concentrations were determined by the standard plate counting method. The plates were incubated at 37 °C for 20 hours, and the number of colonies was enumerated through visual inspection. The bacterial filtration efficiency (BFE) of the filter is defined as follows:

$$BFE = 1 - \frac{C_f}{C_{total}} \tag{4.4}$$

where C_f (CFU/ml) is the bacteria concentration in the Biosampler with a face mask filter operation; C_{total} (CFU/ml) is the bacteria concentration in the Biosampler without a mask filter operation.

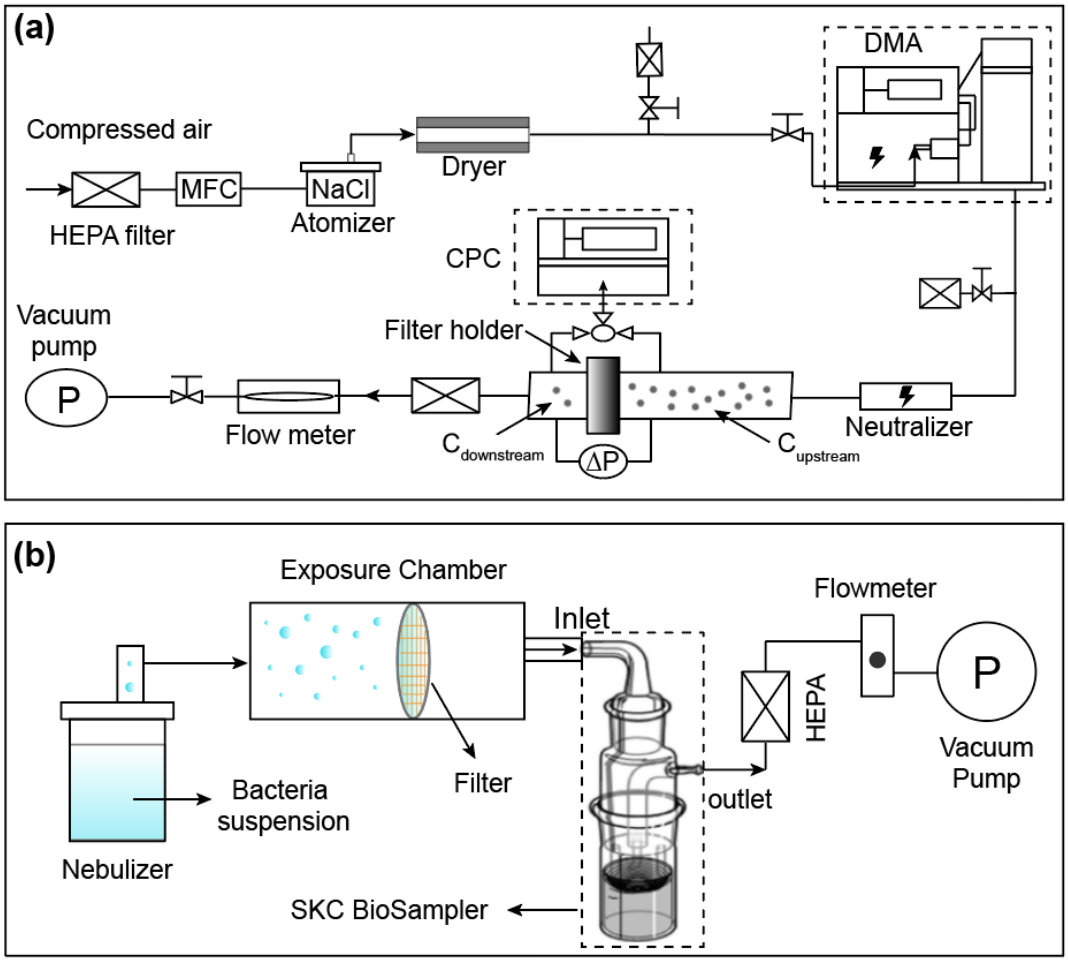

Figure 4.1 Schematic diagram of the experimental setup for particle filtration measurements (a) and bacteria filtration tests (b).

Bacteria Inactivation Assessments The bacteria inactivation assessments were carried out as follows. After being challenged by the bioaerosol for 1 minute, the filter was sealed in a petri dish and placed in the dark for 2 hours to allow the interaction between the filter surface and captured bacteria. Subsequently, the filter was vortexed at 5000 rpm for 5 minutes to resuspend the captured bacteria in the 20 ml PBS solution. Then, the suspension was diluted with PBS, and 3 μL of each decimal dilution was dropped in the sterile nutrient agar culture plates. The agar plates with the bacteria suspensions were incubated at 37 °C for 20 hours to give the visible

colonies, which were enumerated to calculate the number of living bacteria. The bacteria inactivation efficiency (BIE) was calculated by the following equation:

$$BIE = 1 - \frac{C_{live}}{C_{total}} \tag{4.5}$$

where C_{live} is the concentration of live bacteria remaining on the filter. Additionally, after being placed in the dark for 2 hours, the filter was cultured in the nutrient agar at 37 °C for 20 hours for residual analysis of remained viable cells.

Fluorescence microscopy is a useful technique to examine the viability of bacterial cells before and after contacting the filter. To perform this analysis, 1 ml bacteria cell suspension was centrifuged and resuspended in 10 μL of PBS solution, which was subsequently stained by a live/dead staining kit (Molecular Probes, Invitrogen) in the dark for 1 hour. Bacterial cells with intact cell membranes (live) were stained by SYTO 9 and fluorescent green, whereas propidium iodide (PI) penetrates only damaged membranes and stains the dead bacteria, which presented red fluorescence.

4.3 Results and Discussions

The surface chemistry of UiO-66-NH_2, UiO-66-BIBB, UiO-PQDMAEMA, and monomer QDMAEMA were analyzed by FT-IR as shown in **Figure 4.2a**. It is found that the peak at 768 cm^{-1} in the raw UiO-66-NH_2, attributed to the N-H wagging vibrations,[197] disappears in UiO-66-BIBB after modifications. This indicates that the initiator BIBB is successfully anchored on the -NH_2 group of UiO-66-NH_2 via covalent bonding. After ATRP reaction, an emerging peak at 1721 cm^{-1} is found in UiO-PQDMAEMA, which originates from the C=O stretching vibration of ester groups from QDMAEMA[198]; Besides, two additional peaks at 2822 cm^{-1} and 2770 cm^{-1} are also observed in UiO-PQDMAEMA, which are assigned to the -$N(CH_3)_2$

symmetric and asymmetric vibrations from QDMAEMA, respectively.[199] Therefore, it can be concluded that PQDMAEMA is successfully grafted onto UiO-66-NH_2 via ATRP.

In addition to the surface chemistry, the crystalline structures of UiO-66-NH_2, UiO-66-BIBB, and UiO-PQDMAEMA were examined by XRD. As shown in **Figure 4.2b**, the XRD pattern of the as-synthesized UiO-66-NH_2 is well consistent with the simulated one, where the characteristic peaks at 7.4° and 8.8° are attributed to the (111) and (200) crystal planes, respectively.[200] It is noted both UiO-66-BIBB and UiO-PQDMAEMA share almost the same XRD patterns as UiO-66-NH_2, indicating that the crystalline structure of UiO-66-NH_2 is maintained after BIBB treatment and polymerization. The unchanged crystalline structure of UiO-66-NH_2 throughout the entire synthesis procedures also implies that the UiO-66 modified materials are very stable, which is favorable for the post-processing and applications.

To further elucidate the evolution of nitrogen from the -NH_2 group in UiO-66-NH_2, the near-surface elemental information was determined by the XPS measurements. **Figure 4.2c** shows the deconvoluted N 1s core-level peaks of UiO-66-NH_2, UiO-66-BIBB, and UiO-PQDMAEMA. The XPS spectra of UiO-66-NH_2 and UiO-66-BIBB exhibit two nitrogen peaks at 398.9 eV and 399.8 eV, which are assigned to N-H and C-N, respectively.[201] A new peak at 402.0 eV is found in UiO-PQDMAEMA, which is attributed to the C-N^+ component from the monomer QDMAEMA, confirming that an outer quaternized surface layer is formed.[181] Based on the XPS spectra in **Figure 4.2c**, the quaternization degree (QD) of UiO-PQDMAEMA was estimated to be 48%.[202]

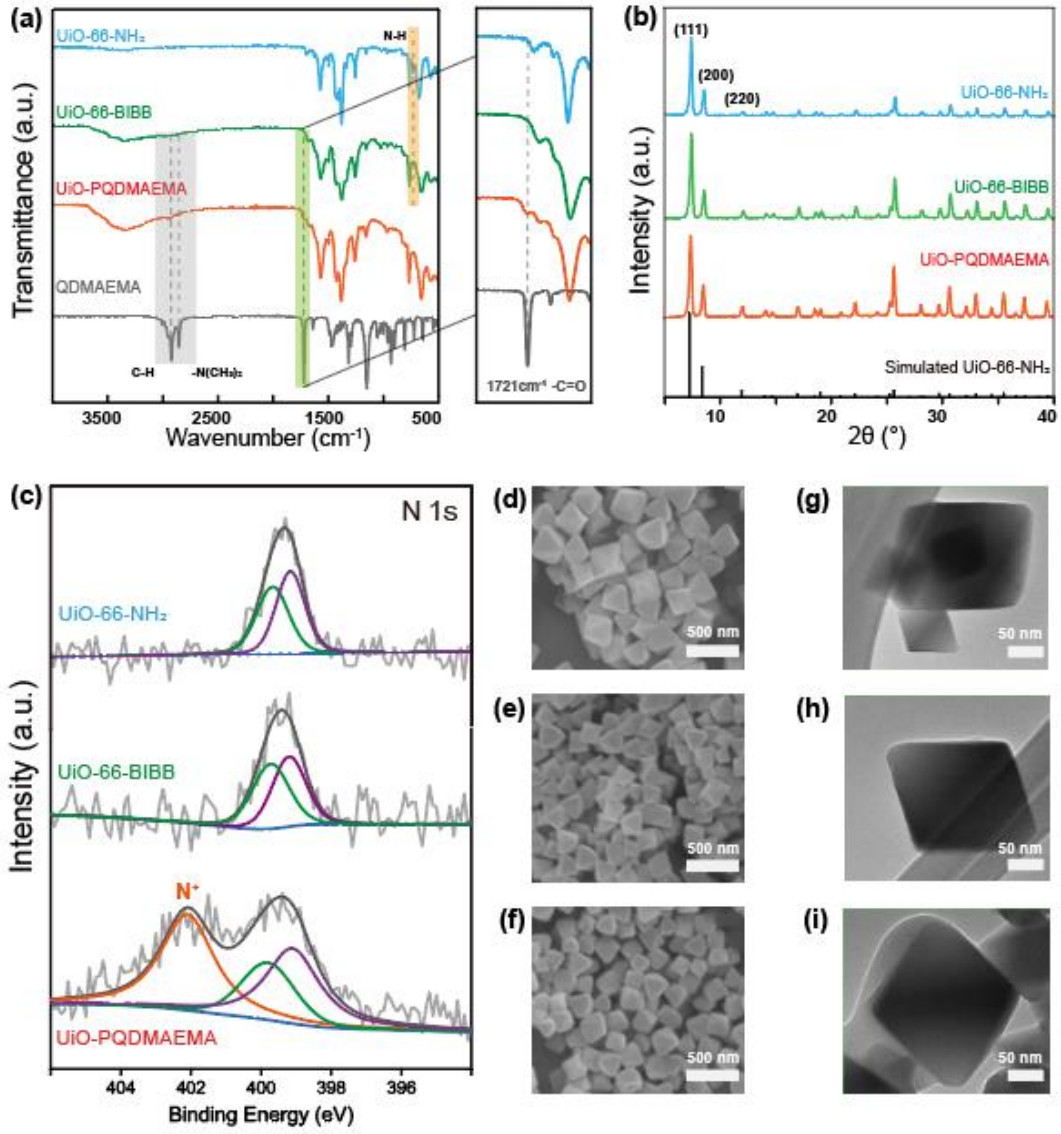

Figure 4.2 FT-IR spectra (a) and XRD patterns (b), high-resolution N 1s XPS spectra (c), SEM images (d-f), and TEM images (g-i) of UiO-66-NH_2, UiO-66-BIBB, and UiO-PQDMAEMA, respectively (top to bottom). Scale bars in (d-f): 500 nm; Scale bars in (g-i): 50 nm.

The morphologies of UiO-66-NH_2, UiO-66-BIBB, and UiO-PQDMAEMA were also observed by SEM. As shown in **Figure 4.2(d, e, g, h)**, UiO-66-BIBB has similar crystal shapes to that of UiO-66-NH_2 with an average particle size of ~265 nm. After the ATRP reaction, the surface of UiO-PQMAEMA becomes smooth (**Figure 4.2f**), and an obvious polymer shell can be observed in its TEM image (**Figure 4.2i**). Understandably, the core contour and size are

similar to those of unmodified UiO-66-NH_2, which is well consistent with the XRD results in **Figure 4.2b**. According to the TGA results, the percentage of polymer in UiO-PQDMAEMA was estimated at 9.93%. All the above results once again confirm the successful grafting of PQDMAEMA onto UiO-66-NH_2.

To fabricate composite nanofibers by using the electrospinning approach, a precursor solution of polymer and filler particles is generally used, resulting in the production of composite nanofibers where the filler particles are uniformly distributed inside the polymer backbone.[169] This homogeneous structures are often undesirable as the functionality of the embedded fillers cannot be fully exploited. This is especially true in this work. To take full advantages of the surface properties of UiO-PQDMAEMA for efficient contact-killing bactericidal assays, the UiO-PQDMAEMA particles should be exposed on the surface of the polymer fibers. However, selective coating of the UiO-PQDMAEMA particles on the PAN fiber surface by using a single-step electrospinning method is challenging. In this work, we developed an engineering approach to rationally tune the diameter of the backbone support PAN fibers smaller than that of the filler UiO-PQDMAEMA particles ($d \cong 213$ nm, **Figure 4.2f**) to expose them on the surface of the PAN fiber. Because the terminal fiber diameter (d_f) in electrospinning is determined by an equilibrium between the repulsive electrostatic force and liquid's surface tension, it can be predicted by the following equation:[203]

$$d_f \sim \left(\gamma \frac{Q^2}{I^2}\right)^{\frac{1}{3}} {w_p}^{\frac{1}{2}} \tag{4.6}$$

where γ is the surface tension of the polymer solution, Q is the feeding flowrate, I is the electric current in the system, and w_p is the polymer volume fraction. Besides, the surface tension is also a function of temperature, which can be expressed as:[204]

$$\gamma = \gamma^0 \left(1 - \frac{T}{T_c}\right)^n \tag{4.7}$$

where γ^0 is the constant for each liquid, n is a positive empirical factor, T_c is the critical temperature and T is the actual temperature. To obtain thinner fibers, we rationally decrease the γ of PAN/DMF solution by increasing the working temperature to 50 °C, given that Q, I, and w_p are all fixed in our system. Furthermore, the working RH was kept at a low level of 10% to generate the thinner nanofibers because a lower RH would favor the solvent evaporation and thus the solidification rate of the jet.[205] Not surprisingly, the defect-free and uniform nanofibers are observed in the pure PAN filter (**Figure 4.3a**). The average diameter of pure PAN fibers is measured to be ~139 nm (**Figure 4.3c**), which is thinner than those fabricated at room temperature (25 °C) and higher RH of 35% with an average diameter size of 242 nm. **Figure 4.3b** shows the morphology of the UiO-PQDMAEMA@PAN filter, where the UiO-PQDAMEMA particles are well decorated on the PAN fiber surface with an overall average diameter of 368 nm (**Figure 4.3d**). The exposure of the UiO-PQDMAEMA particles to the environment (**Figure 4.3b**) gives them more contacting opportunities with captured bacteria. The nitrogen sorption isotherms of the pure PAN and UiO-PQDMAEMA@PAN filters are shown in **Figure 4.3e.** With the successful integration of porous UiO-PQDMAEMA into the PAN fibers, the BET surface area is increased to 790.1 $m^2\ g^{-1}$, which is much higher than the pure PAN filter of 50.8 $m^2\ g^{-1}$. For UiO-PQDMAEMA@PAN, the rapid increase in N_2 uptake at a low relative pressure ($P/P_0 < 0.01$) indicates the abundance of micropores (pore size < 20 Å), which is due to

the existence of UiO-PQDMAEMA, while the slight increase at high relative pressure and the existence of hysteresis suggest the presence of mesopores (200 Å > pore size > 20 Å).[206] Compared to the pure PAN with only mesopores, the UiO-PQDMAEMA@PAN filter exhibits a hierarchical structure containing the characteristics of both micropores and mesopores (**Figure 4.3f**). Moreover, XRD and FT-IR analyses indicate that the crystalline structure and surface chemistry of the UiO-PQDMAEMA are retained after the electrospinning process.

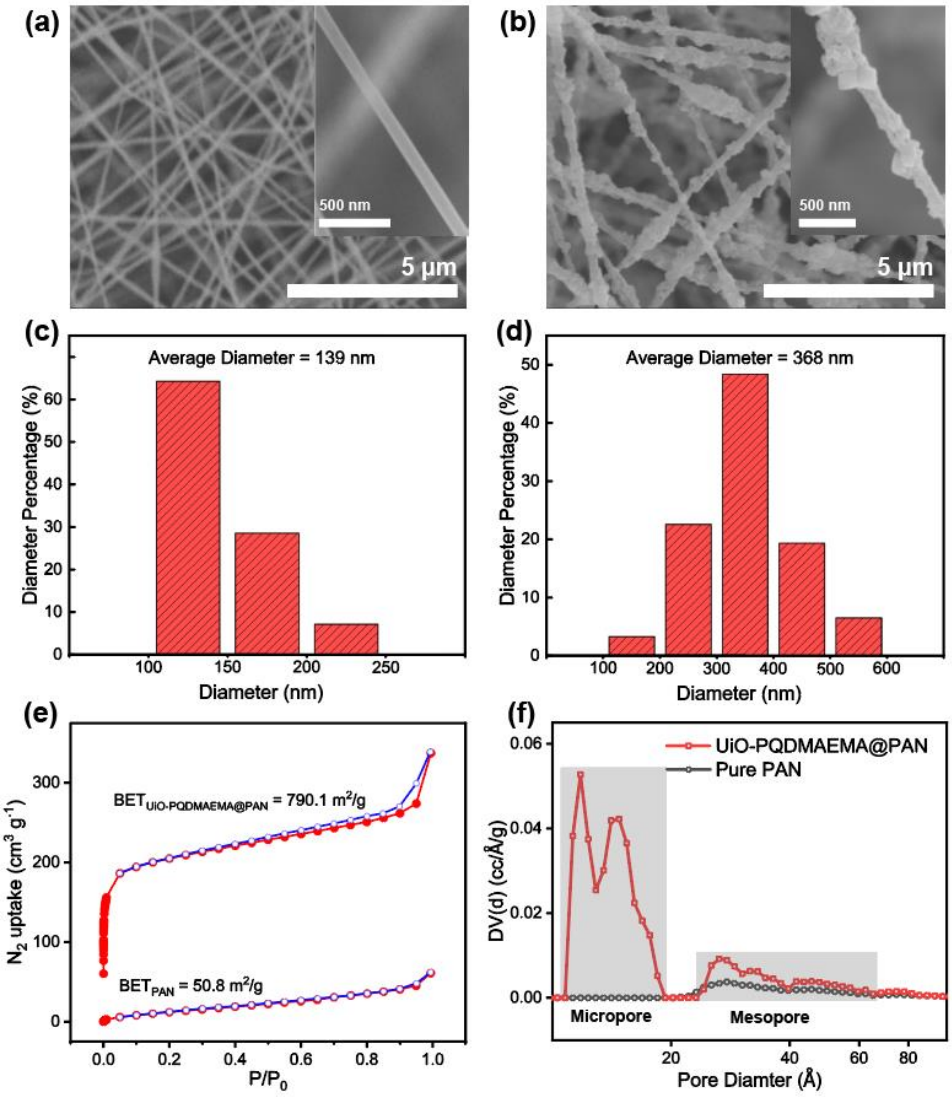

Figure 4.3 SEM images, fiber diameter distribution, and BET analysis of pure PAN filter (a, c, e, f) and UiO-PQDMAEMA@PAN filter (b, d, e, f).

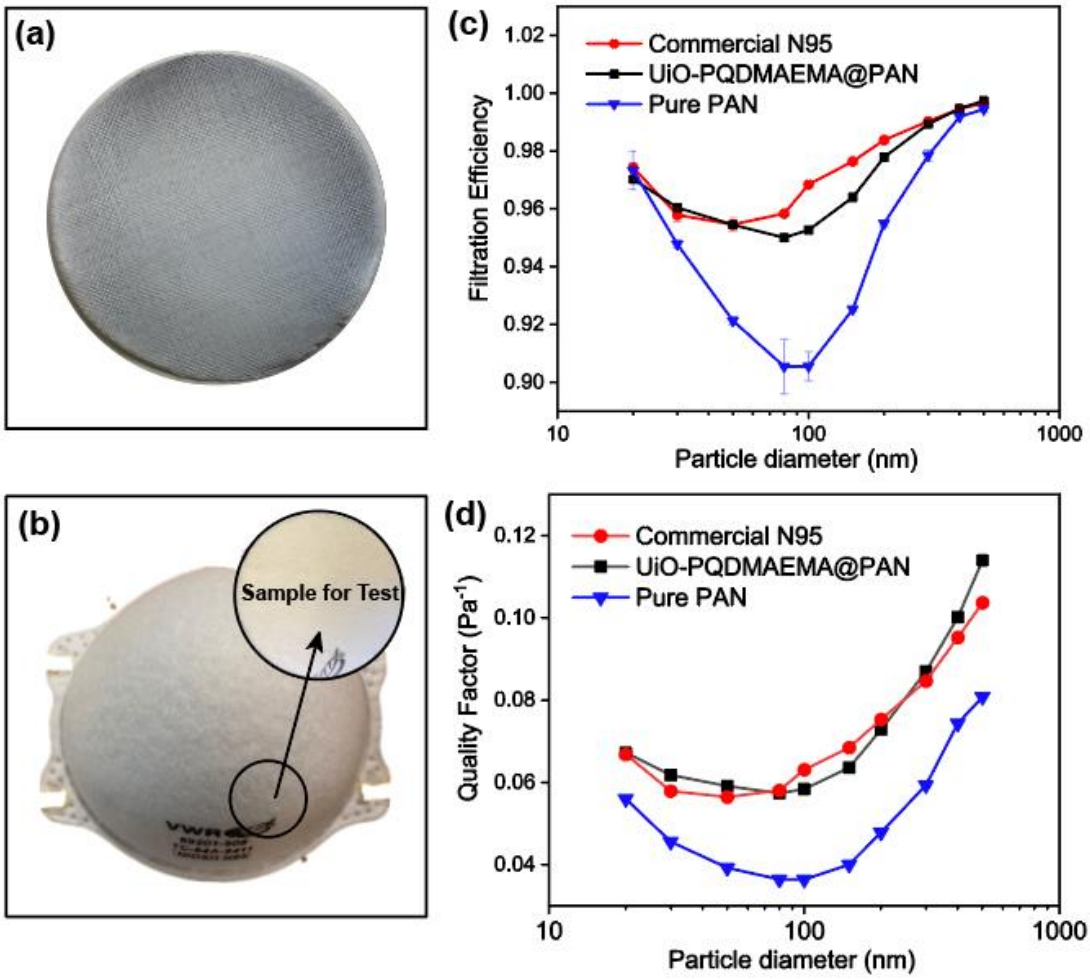

Figure 4.4 Digital images of as-synthesized UiO-PQDMAEMA@PAN filter (a) and commercial N95 respirator (b); Inset image in (b) is a relatively flat sheet cut out from the commercial N95 respirator for particle filtration test; Particle filtration efficiency (c) and quality factor (d) tested by NaCl particles of 20-500 nm at a face velocity at 9.3 cm/s towards pure PAN filter, UiO-PQDMAEMA@PAN filter, and commercial N95 respirator.

The particle filtration performances of the UiO-PQDMAEMA@PAN filter (shown in **Figure 4.4a**) and the N95 (shown in **Figure 4.4b**) were tested by the experimental setup shown in **Figure 4.1a**. It should be noted that the particle filtration efficiency measured throughout the study is the initial particle filtration efficiency as the challenging particles were low concentration monodisperse particles due to the classification of DMA. Thus, the loading effects can be neglected.[207, 208] According to the classic filtration theory,[53] when the particles pass

through the fibrous filter, they are captured by the fiber through a combination of mechanisms including direct interception, inertial impaction, Brownian diffusion, gravitational settling, and electrostatic attraction. For the particles captured at a specific size, the predominant mechanisms vary based on the properties of the tested filters.[55] Therefore, each filter often has a specific size-fractionated efficiency curve. **Figure 4.4c** compares the efficiency curves amongst the pure PAN, UiO-PQDMAEMA@PAN, and N95 filters. It is seen that the particle filtration efficiency decreases with particle size until it reaches the most penetrating particle size (MPPS) at around 80 nm, and subsequently increases for particles greater than 80 nm. By controlling the volume of the precursors, the thickness of the UiO-PQDMAEMA@PAN filter is adjusted to 16 μm, and the minimum filtration efficiency of as-synthesized UiO-PQDMAEMA@PAN filter at 80 nm is measured to be ~95.1%. The filtration performance is comparable to that of a commercial N95 respirator, which makes the UiO-PQDMAEMA@PAN a potential candidate for an N95 respirator filter medium. It is noted that as compared to the pure PAN filter tested under the same pressure drop (52.3 Pa), a higher filtration efficiency is obtained for the UiO-PQDMAEMA@PAN filter and the MPPS is smaller than that of pure PAN fiber (MPPS = 100 nm). This is probably due to the positively charge from the UiO-PQDMAEMA, which increase the electostatic attraction during the filtration.

The pressure drop is another very important parameter, as breathing air behind the face mask requires significant pressure or energy provided by the users, which is highly related to wearer's comfort and health during breath. Therefore, a low-pressure drop is always a desirable filter property. The quality factor (QF), a comprehensive parameter, is used to evaluate the filtration performance of the filter media, which takes both efficiency and pressure into account. The QF is defined as:[51]

$$QF = -\frac{\ln(1 - PFE)}{\Delta P} \tag{4.8}$$

where PFE and ΔP are the particle filtration efficiency and pressure drop across the filter, respectively. The higher the QF, the better the filter is. Given that the higher QF values are obtained as compared to the pure PAN, the UiO-PQDMAEMA@PAN filter has a much better filtration performance because of the incorporation of UiO-PQDMAEMA in the electrospun nanofibers. Additionally, the minimum QF value of the UiO-PQDMAEMA@PAN filter is calculated to be 0.058 at MPPS of 80 nm, which is comparable to that of 0.056 for the commercial N95 respirator at 50 nm, indicating that the UiO-PQDMAEMA@PAN filter demonstrates a satisfactory filtration performance.

The bacteria filtration performance of the UiO-PQDMAEMA@PAN filter is evaluated by challenging with the bioaerosols containing *S. epidermidis* (Gram-positive bacteria) and *E. coli* (Gram-negative bacteria). The schematic diagram of the experimental setup for the bioaerosol filtration is shown in **Figure 4.1b**. The BioSampler (SKC Inc) which combines impingement with centrifugal motion is used for the escaped bacteria collection. Specifically, there are three collection nozzles positioned at a specific angle above the collection sterile PBS solution during the sampling, and the air stream with bacteria is directed to the wall of the sampling where a liquid film is formed due to the centrifugal motion of the liquid.[209] This design lowers the microorganism stress as compared to the conventional impinger and ensures the viability of the collected bacteria, which makes SKC BioSampler a reliable and *de facto* reference sampler in bioaerosol studies.[210] The recommended air flowrate for the N95 respirator test is 28.3 L/min by the U.S. Food and Drug Administration (FDA),[211] where the face velocity is calculated to be 3.1 cm/s.[211] In our system, the face velocity of the tested filter is calculated to be

10.5 cm/s, given that the working flowrate of the BioSampler should be fixed at 12.5 L/min to ensure the accuracy of the bacteria collection.[212] As shown in **Figure 4.5(a, b)**, no bacteria of *S. epidermidis and E. coli* are found after passing through the UiO-PQDMAEMA@PAN filter as well as the commercial N95 respirator, which indicates that all the airborne bacteria are completely captured by the filter even at a high face velocity of 10.5 cm/s. The reason for the airborne bacteria that cannot pass through the UiO-PQDMAEMA@PAN filter is mainly due to their sizes. Both *S. epidermidis* and *E. coli* have sizes in the range from 0.5 to 2 μm, which is much larger than the MPPS (< 100 nm) as discussed above. Therefore, the bacteria filtration of these filters is much more efficient. In summary, the as-synthesized UiO-PQDMAEMA@PAN filter demonstrates an excellent performance towards bacteria capture, which could be potentially used to protect user's safety by blocking out the routes of airborne bacteria transmission.

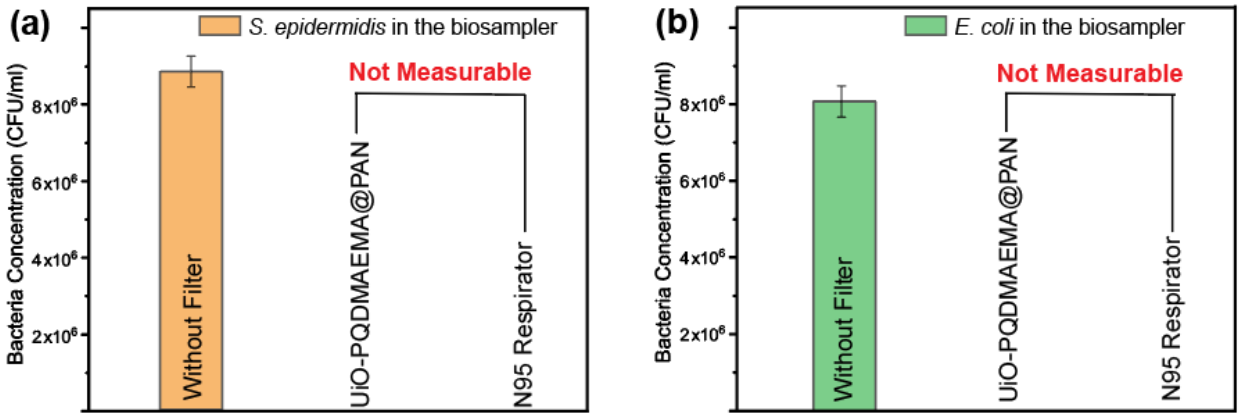

Figure 4.5 Collected *S. epidermidis* (a) and *E. coli* (b) concentration in the SKC BioSampler after the airborne bacteria passing through the UiO-PQDMAEMA@PAN filter and commercial N95 respirator.

The bacteria inactivation performance of the UiO-PQDAMEMA@PAN filter was also evaluated towards both *S. epidermidis* and *E. coli*. Control experiments of pure PAN filter and UiO-66-NH_2@PAN filter were also conducted for comparison. As shown in **Figure 4.6(a, b)**,

both pure PAN and UiO-66-NH_2@PAN filters show limited capabilities of killing bacteria while the UiO-PQDMAEMA@PAN filter has a significant inactivation efficiency of ~97.4% of *S. epidermidis* and ~95.1% of *E. coli*, indicating that the grafted UiO-PQDMAEMA on the surface of PAN fibers enables the filter to have efficient bactericidal behaviors. Further live/dead bacteria fluorescence assays using LIVE/DEAD kit were also conducted to investigate the bactericidal effects of the UiO-PQDMAEMA@PAN filter. Before conducting the experiments, most bacteria were alive and stained by SYTO 9, therefore, numerous green dots are observed in **Figure 4.6(c, d)**. However, the number of dead bacteria, which emit the red fluorescence was increased significantly after contacting the surface of the UiO-PQDMAEMA@PAN filter, implying that the membrane integrity of bacterial cells is disrupted. Meanwhile, the ratio of live and dead bacteria in fluorescence images shows almost no change in the control group of pure PAN and UiO-66-NH_2@PAN filters once again confirming the bactericidal behaviors of the UiO-PQDMAEMAM@PAN filter. The commercial N95 respirator was also tested towards bactericidal performance. As shown in **Figure 4.6(a, b)**, negligible bacterial inactivation efficiencies can be obtained for *S. epidermidis* and *E. coli*, indicating that most of the adhered bacteria are still alive, which is the main reason that the contaminated respirator could be the source of HAIs transmission. As compared to the commercial N95 respirator, the as-synthesized UiO-PQDMAEMA@PAN filter demonstrates an efficient and rapid bacteria inactivation performance, which makes it a promising candidate for the antibacterial filter in the N95 level respirator.

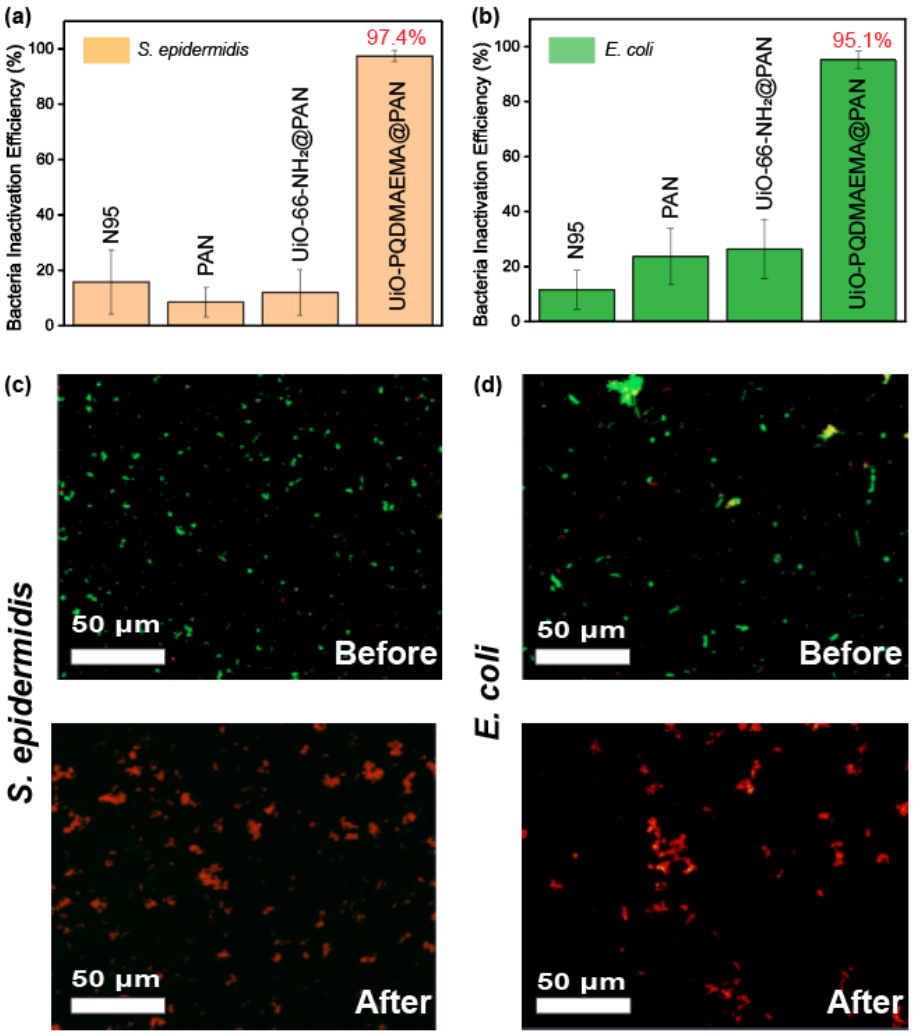

Figure 4.6 *S. epidermidis* (a) and *E. coli*. (b) inactivation performance towards commercial N95 respirator filter, PAN, UiO-66-NH_2@PAN, and UiO-PQDMAEMA@PAN filter; Fluorescence images of the collected *S. epidermidis* (c) and *E. coli*. (d) before and after contacting the UiO-PQDMAEMA@PAN filter.

Since typical bactericidal activities of QAC-based polymers are based on the contact killing mechanism, where the electrostatic interactions between negatively charged bacteria cell wall and positively charged QAC-based molecules are mainly responsible for the disruption of bacteria membrane, two prerequisites should be satisfied to endow the materials to have efficient antibacterial performance. [188, 213] One is the enough contacting time between bacteria and QAC-modified surfaces, and the other is that a threshold of charge density should be reached. [214] In

this study, when the airborne bacteria are captured by the filter, they are trapped by multiple nanofibers containing numerous contacting sites of positively charged UiO-PQDMAEMA (N^+). (**Scheme 4.1**, **Figure 4.2c**) The UiO-PQDMAEMA@PAN filters exhibit limited bactericidal performance within the first 30 minutes, which is probably due to the insufficient interactions between bacterial cell wall and UiO-PQDMAEMA particles. When the contacting time extended to 2 hours, 97.4% of *S. epidermidis* and 95.1% *E. coli* were finally killed. Compared to the Gram-positive bacteria *S. epidermidis*, the Gram-negative bacteria *E. coli* exhibited a relatively greater resistance to contact disinfection, as shown in **Figure 4.6**, indicating a difference in physicochemical interaction with the UiO-PQDMAEMA@PAN. The discrepancy in the antibacterial efficiency could be caused by various cell structures between the Gram-positive bacteria and the Gram-negative bacteria. The Gram-positive bacterial cell wall is composed of a simple layer of peptidoglycan. This layer has numerous pores, which allow the QAC molecules to readily penetrate the thick cell wall and reach the cytoplasmatic membrane.[215] However, the cell wall of the Gram-negative bacteria *E. coli* is comprised of two membranes reinforced by the expression of lipopolysaccharide on the cellular surface, which provides an additional protective property.[216] Therefore, a more efficient antibacterial performance was obtained towards *S. epidermidis* than *E. coli*.

The positive charge density of outer layer is another key parameter to define antibacterial efficacy.[214] For *S. epidermidis* and *E. coli* inactivation, the prerequisite charge density should be above the critical threshold of 1×10^{12} -10^{14} N^+/cm^2. [217, 218] To calculate the charge density of UiO-PQDMAEMA, we used the crystal in **Figure 4.2i** for further estimation. The crystal in red contour is the initial UiO-66-NH_2, which is decorated by a layer of QAC polymer. Assuming that

charges were uniformly distributed within the polymer layer, the charge density (CD) can be determined by the following equation:

$$CD = \frac{Q}{A} \tag{4.9}$$

where Q is the surface charge and A is the surface area. The CD of UiO-PQDMAEMA was calculated to be 3×10^{14} N^+/cm^2. Therefore, UiO-PQDMAEMA in this work is expected to exhibit effective antibacterial actions. Besides, the monomer DMAEMA is quaternized by 1-bromodecane to impart the QDMAEMA with 10 carbon atoms in the alkyl chains. (**Scheme 4.2**) The relatively long alkyl chains in UiO-PQDMAEMA could interact strongly with the peptidoglycan cell wall and, finally, bacteria are killed by the lysis of their cytoplasm.[187]

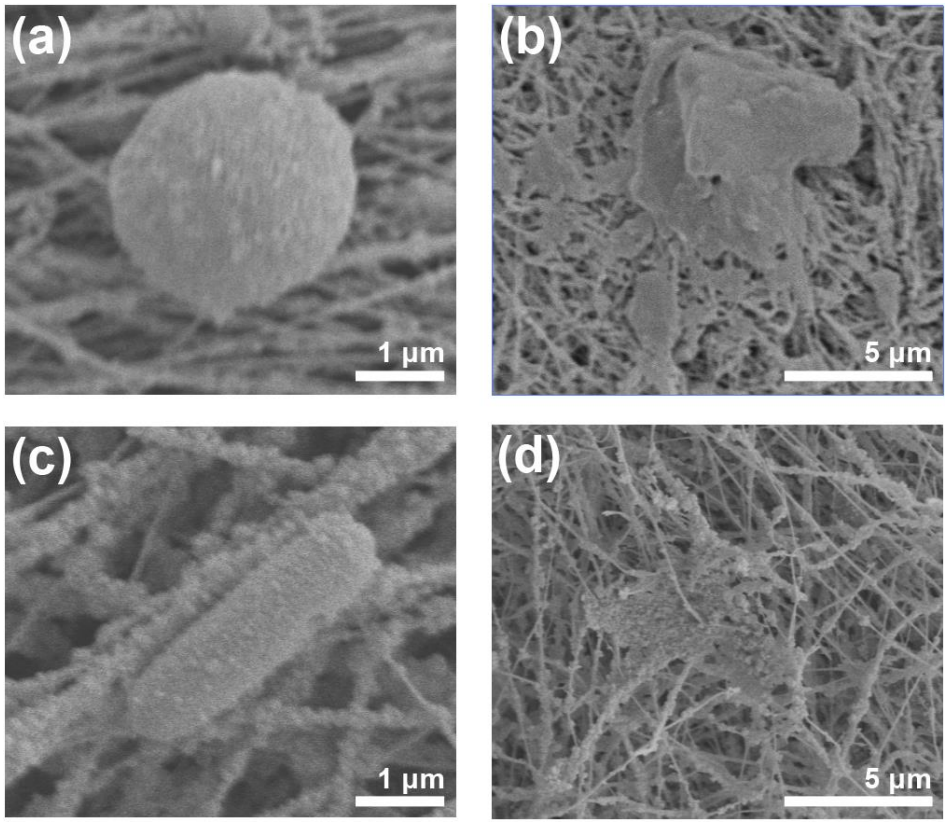

Figure 4.7 SEM images of UiO-PQDMAEMA@PAN filter with *S. epidermidis* (a, b) and *E. coli*. (c, d) after contacting treatment for 0 and 2 hours.

To further unravel the interactions between UiO-PQDMAEMA@PAN filter and bacteria, the morphologies of *S. epidermidis* and *E. coli* were observed by SEM. As shown in **Figure 4.7 (a, c)**, the cells of *S. epidermidis* and *E. coli* maintained intact upon initial contact with the UiO-PQDMAEMA filter. After contacting treatment for 2 hours, the shapes of both *S. epidermidis* and *E. coli* are deformed, and the cell membranes are severely damaged (**Figure 4.7 (b, d)**), which indicates that the QAC modified MOF enables the electrospun filter with efficient antibacterial capability against both Gram-negative and Gram-positive bacteria.

The leakage of the antibacterial agent during the filtration and antimicrobial activity is a serious issue because improper intake of these chemicals would result in severe health issues.[219] Among the commercial antimicrobial face masks and respirators, Ag^{+} and Cu^{2+} are the two most frequently used metal ions in the filter media to inactivate microorganisms.[220] Herein, we fabricated a Cu^{2+}-loaded PAN filter (Cu@PAN) for comparison. To examine the leakage behaviors, both UiO-PQDMAEMA@PAN and Cu@PAN filters were immersed in the 100 ml DI water for 2 hours. Then, 1 ml $AgNO_3$ (1 mM) and Na_2S (1 mM) were added into UiO-PQDMAEMA@PAN and Cu@PAN solutions, respectively. The rationale for designing the leakage test is as follows. For the UiO-PQDMAEMA@PAN filter, there might be some Br^{-} released from the 1-bromodecane ($C_{10}H_{21}Br$) in the UiO-PQDMAEMA particles (see **Scheme 4.2** for details). If Br^{-} is leaked from the filter, it would react quickly with Ag^{+} to form a yellow precipitate, AgBr. Similarly, the Cu^{2+} released from Cu@PAN filter would combine with S^{2-} in the Na_2S solution to produce CuS precipitates. No color change is observed in the UiO-PQDMAEMA@PAN beaker after $AgNO_3$ titration, indicating there is negligible Br^{-} leakage. While the solution turned to be brown in the Cu@PAN beaker, which is caused by the formation of a low concentration of CuS precipitates. As compared to the Cu@PAN filter, negligible

leakage was found in the UiO-PQDMAEMA@PAN immersed in the water, indicating that the UiO-PQDMAEMA@PAN filter is safe for humans and environmentally friendly.

4.4 Conclusions

In summary, we designed an antibacterial filter where the QAC modified MOF (UiO-PQDMAEMA) was incorporated into the electrospun PAN fibers. The antibacterial agent polymeric QACs (PQDMAEMA) was grafted onto the surface of UiO-66-NH_2 via ATRP. To partially expose the surface of the UiO-PQDMAEMA particles, the backbone electrospun PAN nanofibers were produced at an enhanced working temperature of 50 °C and low RH of 10%. The as-synthesized UiO-PQDMAEMA@PAN filter exhibited a satisfactory performance towards PM filtration and bacterial blockage, which is comparable to those of the commercial N95 respirator. In particular, the UiO-PQDMAEMA@PAN filter demonstrated excellent bactericidal activities towards both Gram-positive *S. epidermidis* and Gram-negative *E. coli* via a contact-killing mechanism. The incorporated UiO-PQDMAEMA particles with positively charged nitrogen (N^+) in the long alky chain resulted in the deformation and damage of cells after electrostatic interactions between UiO-PQDMAEMA and bacteria. The current work indicates that the UiO-PQDMAEMA@PAN could be a comprehensive protection core filter for the N95 respirator against PM and airborne bacteria. This study also sheds light on the design of QAC modified antibacterial materials and paves a way for the application of these materials in air cleaning.

Chapter 5. Biointerface Matters: Smart Charge Integration on Heterogeneous Photocatalyst Surface to Boost Photocatalytic Disinfection Activity

Abstract

Photocatalytic disinfection of pathogens has become a popular approach in public health due to its environmentally friendly bactericidal capabilities. However, it still suffers from low efficacies due to the inherent electron-hole recombination and poor interactions between bacterial cells and photogenerated reactive oxygen species (ROS) on the biointerface. In particular, the ROS with extremely short migration distances cannot reach the bacterial cells before they deteriorate into less potent or neutral species, which results in reduced antibacterial activities. However, these phenomena are still poorly understood. Inspired by the fact that bacterial cells are negatively charged, we rationally designed and coated a layer of positively charged quaternary ammonium compound (QAC) polymer onto the surface of a heterogeneous photocatalyst (*i.e.*, g-C_3N_4/metal-organic framework) to enhance the affinity towards bacterial cells via electrostatic interactions. The QAC-coated photocatalyst is denoted as C-M-Q. The visualization and quantification of the electrostatic interactions between the bacterial cells and the C-M-Q photocatalyst were conducted by using a confocal laser scanning microscope (CLSM) and atomic force microscope (AFM), respectively. The results showed that the positively charged QAC layer did promote the bacterial-photocatalyst contact via electrostatic attractions. Due to the cooperative effects of bacterial cells adhesion and ROS generation, the photocatalytic bactericidal activity of C-M-Q is significantly enhanced. Notably, the C-M-Q photocatalyst achieves 3.20 logs of inactivation efficiency for Gram-positive *Streptococcus epidermidis* (*S. epidermidis*) and 1.45 logs for Gram-negative *Escherichia coli* (*E. coli*) bacteria within 60 min under the visible light irradiation. This work sheds light on the photocatalyst design with surface charge modification for antibacterial applications.

5.1 Introduction

The ongoing COVID-19 pandemic, which is caused by a new human coronavirus (SARS-CoV-2), has posed a severe threat to human health.[221-223] Besides SARS-CoV-2, many other pathogenic microbes are devastating to humans as well. Pathogenic bacteria, for instance, are infecting millions of people and killing over one million people every year, which results in a heavy burden on the social economy and public health.[153, 224, 225] Typically, pathogenic bacteria are transmitted via direct and indirect modes. During direct transmission, the pathogenic bacteria are transferred from a reservoir to a susceptible host by direct contact or droplet spread.[226] By indirect transmission, people are infected by the bio-contaminants in the environment, such as airborne particles, food, water, and fomites (contaminated surfaces).[223, 227, 228] Converging evidence shows that environmental biocontamination will result in an increased risk of the secondary transmission.[229] Therefore, efficient disinfection in the environment is essential to decrease the spread of pathogenic bacterial transmission and thus assure the safety of public health.[227, 230-235]

In recent years, the advanced oxidation processes have been widely used for bacterial disinfection, in which the reactive oxygen species (ROS) such as hydroxyl radical ($^{\cdot}OH$), hydrogen peroxide (H_2O_2), superoxide ($\cdot O_2^-$), and singlet oxygen ($^1O_2$) are utilized to cause extensive damage to most macromolecules including protein, DNA, and lipids.[233, 236-248] In particular, the photocatalysis technology is receiving considerable attention as it uses the light to generate various ROS to eradicate pathogenic bacteria.[1, 234, 235, 237, 249] However, the efficacy of photocatalytic disinfection towards bacterial cells is limited due to the lack of consideration in biointerface design. In addition to the inherent electron-hole recombination that is generally regarded as a major hindering factor in photocatalysis, several other essential factors need to be

considered as well to design a highly efficient photocatalyst for bacterial disinfection. Firstly, ROS are generated only on the surface of the photocatalyst. They typically have short half-life times ($t_{1/2}$) and migration distances (λ).[248, 250] Specifically, $^{\cdot}OH$, H_2O_2, $\cdot O_2^-$, and $^1O_2$ have half-life times of 1-4 μs, 1 μs, 1 ms, and 1-4 μs, with migration distances of 30 nm, 1 nm, 1μm, and 30 nm, respectively.[251] For example, $^{\cdot}OH$ radicals only affect bacterial cells located a few nanometers (λ_{OH} = 1 nm) from their site of generation. Given the extremely short half-life time ($t_{1/2}$ = 1 μs), $^{\cdot}OH$ species are unlikely to reach cells and cause damage to biomolecules in most cases.[245] Even though $^{\cdot}OH$ is 100-fold more potent than H_2O_2 and $\cdot O_2^-$, the potency is not fully used, which limits the overall photocatalytic bactericidal efficacy.[245, 252] The second reason for limited photocatalytic disinfection performance is the affinity of bacterial cells to photocatalysts is not strong. Because of the chemical complexity of the cell wall, the movement of the bacterial cells in the aqueous photocatalyst system is unpredictable.[253] The poor affinity of bacterial cells to the photocatalyst surface will result in slow photocatalytic disinfection rates.[254] For example, bacteria in neutral pH values are negatively charged due to the presence of carboxylic and phosphate groups in the cell wall.[181, 255, 256] However, most metal oxide-based photocatalysts (*e.g.*, TiO_2) also carry negative charges in neutral pH due to the hydroxide anions (OH-) adoption on the surface.[256] This creates electrostatic repulsion on the biointerface, leading to a decreased bacterial cells adhesion on the photocatalyst, where the photocatalytic disinfection depends strongly on the ROS diffusion and penetration into bacterial cells.[257] Therefore, to improve the photocatalytic performance, the biointerface where bacterial cells interact with the photocatalyst must be rationally designed.

In a photocatalytic disinfection system, the fate of bacterial cell movement on the biointerface is determined by many factors, including Brownian motion, van der Waals attraction,

gravitation, electrostatic interactions, and hydrophobicity interactions.[258, 259] According to the well-known extended Derjaguin-Landau-Verwey-Overbeek (DLVO) theory, the adhesion force (F_{adh}) between bacterial cells and material surface can be expressed as follows:[258]

$$F_{adh} = F_{vdW} + F_e + F_{AB} \quad (5.1)$$

where F_{vdW} is the classical van der Waals force, F_e is the electrostatic force, and F_{AB} is the acid-base (AB) interaction force. If F_{adh} has a positive value, namely, the attractive forces overweigh repulsive forces, the contact between bacterial cells and material surface proceeds, and vice versa. F_{vdW} is generally attractive regardless of the types of bacteria and materials. F_{AB} can be either attractive or repulsive depending on the environment, bacteria, and the surface chemistry of materials. But F_{AB} is only effective at a short-range (i.e., within 10 nm) due to the electron acceptor/electron donor interactions between polar moieties in polar media (*e.g.*, water).[258] Therefore, the interaction at a long-range is governed by the overall effects of F_{vdW} and F_e. Fortunately, in natural water system, almost all bacteria are negatively charged, which gives the chance to attract bacterial cells with electrostatic effects by modulating the material into positively charged.[181, 255, 256] Therefore, tuning material with a positively charged surface will favor the attraction of bacteria, which is expected to endow the photocatalyst with more efficient photocatalytic antibacterial activities.

However, the quantitative understanding of the interactions between the bacterial cells and the photocatalyst surface is still lacking. In particular, to further unravel the role of the electrostatic interactions in photocatalytic disinfection, we designed a heterogeneous photocatalyst by rationally immobilizing a layer of positively charged quaternary ammonium compound (QAC) polymer onto the surface of g-C_3N_4/MIL-124-NH_2 composite. The final product is termed "C-M-Q". The bare photocatalyst C-M is composed of two components, where

C indicates tris-s-triazine based g-C_3N_4, a two-dimension (2D) structure material comprising small flat sheets with wrinkles and M refers to metal-organic frameworks (MOFs, MIL-125-NH_2 as an example), a class of highly porous materials constructed by metal ions and organic ligands. Poly [2-(dimethyl decyl ammonium) ethyl methacrylate] (PQDMAEMA) was chosen as the QAC polymer, which can not only attract the bacterial cells toward the surface of the C-M-Q photocatalyst but also kill the bacteria by destroying their cell membranes via the strong electrostatic forces. As expected, compared to the bare photocatalyst C-M, the C-M-Q with a positively charged QAC layer demonstrated significantly improved photocatalytic antibacterial performance, achieving 3.20 log inactivation efficiency for *S. epidermidis* and 1.67 log inactivation for *E. coli* in 60 minutes under visible light irradiation. Systematic material characterization and biological experiments were carried out to reveal the cooperative photocatalytic antibacterial behaviors caused by the positively charged QAC layer at the C-M-Q surface. Particularly, we used the atomic force microscope (AFM), a powerful tool to investigate nano-mechanical properties, to quantify the force-interactions between C-M-Q and bacterial cells. A remarkable enhancement in adhesion force of 972 pN was observed between C-M-Q modified cantilever tip and bacteria, while only 115 pN adhesion force was measured between unmodified reference Si cantilever tip and bacteria. The results once again confirm that positive charge integration (QAC layer) on MOF-based catalyst facilitates bacteria adhesion on the photocatalyst surface. The outcome of this work sheds light on the photocatalyst design using charge effects to promote bacterial-photocatalyst contact for photocatalytic antibacterial applications.

5.2 Materials and Methods

Preparation of C-M and C-M-Q The bare photocatalyst C-M is fabricated via a solvothermal method, where the originally prepared g-C_3N_4 (C) was suspended in the precursor of MOF MIL-

125-NH_2 (M) before heat treatment. For QAC modification, the monomer 2-(dimethyl decyl ammonium) ethyl methacrylate (QDMAEMA) was polymerized and grafted on the surface of C-M through the classical atomic transfer radical polymerization (ATRP) approach to obtain the final product, which is denoted as C-M-Q. The preparation route is seen in **Scheme 5.1**.

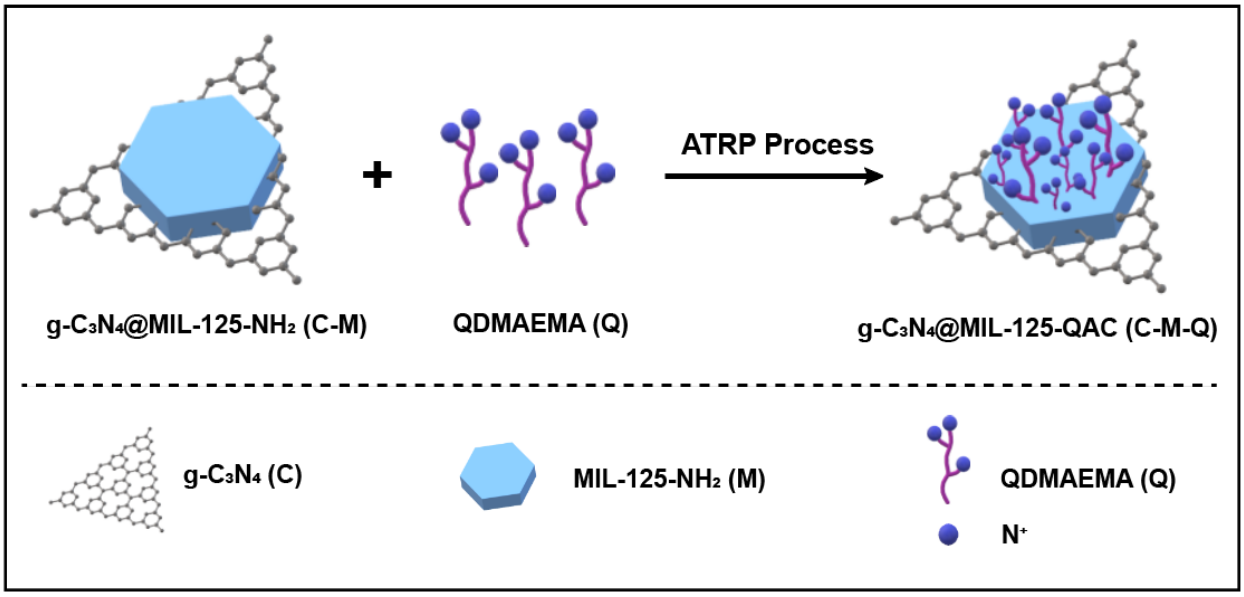

Scheme 5.1 Schematic preparation route for C-M-Q.

Chemicals N, N, N', N'', N''-pentamethyl diethylenetriamine (PMDETA, 99%), 2-(dimethylamino)ethyl methacrylate (DMAEMA, 98%), copper (I) bromide (CuBr, 98%), copper (Ⅱ) bromide ($CuBr_2$, 99%), 2-bromoisobutyryl bromide (BIBB, 98%), 1-bromodecane (98%), isopropyl ether (99%), acetonitrile (99.5%), triethylamine (TEA, 99%), 2-amino-1,4-dicarboxylic acid (BDC-NH_2, 99%), titanium tetraisopropoxide (TTIP, 97%), urea (99.0-100.5%), catalase from bovine liver, Poly-L-lysine solution (0.01%), 1-ethyl-3-(3dimethylaminopropyl) carbodiimide (EDC, 98%), and N hydroxysuccinimide (NHS, 98%) were purchased from Sigma Aldrich. Anhydrous tetrahydrofuran (THF, 99.8%) was obtained

from Alfa Aesar. Methanol (99.8%) and N, N-dimethylformamide (DMF, 99%) were purchased from VWR Corporation. All chemicals were used as received without further purification.

Synthesis of g-C_3N_4 (C) g-C_3N_4 was prepared based on the previous work with some modifications.[260] Typically, 10 g urea powder was put into a crucible with a cover, which was subsequently kept at 550 ℃ in a muffle furnace for 2 hours with a heating rate of 0.5 ℃/min. The obtained pale-yellow powders were washed with deionized water for three times and dried in the vacuum at 50 ℃ for storage.

Synthesis of g-C_3N_4@MIL- 125-NH_2 (C-M) g-C_3N_4 was prepared based on the previous work with some modifications.[260] Typically, 10 g urea powder was put into a crucible with a cover, which was subsequently kept at 550 ℃ in a muffle furnace for 2 hours with a heating rate of 0.5 ℃ /min. The obtained pale-yellow powders were washed with deionized water for three times and dried in the vacuum at 50 ℃ for storage.

Synthesis of g-C_3N_4@MIL- 125-NH_2 (C-M) C-M was synthesized via a solvothermal method. Firstly, 0.651 g 2-aminoterephthalic acid (BDC-NH_2) was dissolved in a mixture of 15 ml DMF and 15 ml methanol. Then, 0.3 g g-C_3N_4 was added into above solution, which was further ultrasonicated for 30 minutes to get the homogeneous suspension. 0.797 ml titanium tetraisopropoxide (TTIP) was added into above suspension, which was subsequently transferred to a Teflon-lined steel autoclave reactor and placed in an oven at 150 °C for 15 h. he obtained yellow products were isolated by centrifugation and washed by 30 mL DMF and 30 mL methanol, respectively, for three times. Finally, the samples were dried under 50 °C overnight in vacuum.

Synthesis of g-C_3N_4@MIL-125-BIBB (C-M-BIBB) The C-M-BIBB was obtained by functionalizing C-M under the protection of nitrogen in a 50 ml flask.[255] In a typical procedure, 0.3 g C-M was suspended in 20 ml anhydrous THF by sonication. 418 μL TEA and 124 μL BIBB were dissolved in 10 ml THF separately. The TEA solution was injected into the C-M suspension under stirring. Then the BIBB solution was dropwise added into the mixture in 30 minutes with ice water cooling and strong stirring. The reactants were subsequently sealed and stirred at 50 °C for 24 hours. Finally, the particles were washed with THF and methanol and dried under vacuum at 40 °C. The obtained products were named C-M-BIBB.

Synthesis of g-C_3N_4@MIL-QAC (C-M-Q) The atomic transfer radical polymerization(ATRP) process was conducted based on a previous work but with some modifications.[255] Poly [2(dimethyl decyl ammonium) ethyl methacrylate] (PQDMAEMA, a typical antibacterial quaternary ammonium compound (QAC) agent) brushes were prepared by ATRP of QDMAEMA from C-M-BIBB. To prepare QDMAEMA, 2.68 ml DMAEMA and 3.9 ml of 1-bromodecane were added into 10 ml acetonitrile in a 50 ml flask and reacted for 24 hours at 40 °C. After cooling to room temperature, the solution was slowly dripped into 200 ml isopropyl ether, and the white precipitates were collected by centrifugation. The precipitate was dissolved in acetonitrile and then carried on the precipitation centrifugation process for another two times. For ATRP, 0.7 g QDMAEMA and 200 μL PMDETA were added into a 10 ml mixture of deionized water and methanol (volume ratio = 1:1) in a 50 ml flask. Under the protection of nitrogen, 10 mg $CuBr_2$ and 0.15 g C-M-BIBB were added to the mixture. After nitrogen bubbling for 20 minutes, 32.4 mg CuBr was added into the flask, which was then tightly sealed. After stirring for 36 hours at 30 °C, the PQDMAEMA-modified C-M-BIBB was prepared. The

samples were separated by centrifugation and washed by deionized water and methanol for 3 times. Finally, the obtained particles were naturally dried in the air, which is denoted as C-M-Q.

Material characterization The chemical functional groups were examined by a Fourier transform infrared (FT-IR) spectrometer (Nicolet iS50). The crystallinity of the materials was determined by powder X-ray diffraction (PXRD, PANalytical X'Pert Pro MPD). Morphologies of the materials were observed by scanning electron microscopy (SEM, Su-70, Hitachi). Thermal stability and components of the samples were determined by thermogravimetric analysis (TGA) with a TA Q500 under a nitrogen flow environment. The optical properties of the samples were investigated by a UV-visible (UV-vis) spectrometer. The surface charge of the materials was examined by a zeta potential analyzer (Zetasizer Nano ZS, Malvern Instruments Ltd.). The electronic state of the elements within the materials was analyzed by X-ray photoelectron spectroscopy (XPS, Thermo Scientific ESCALAB 250). The fluorescence images were obtained by the Zeiss Axiovert 200M fluorescence microscope. Water contact angles were characterized by a goniometer (OCA 15, DataPhysics). The conductivity of the solution was measured by the Hach Sension MM374.

Photocatalytic disinfection Gram-positive *Streptococcus epidermidis* (*S. epidermidis*) and Gram-negative *Escherichia coli* (*E. coli*) were used as the model bacteria. *S. epidermidis* cells were cultured in a nutrient solution containing 5 g peptone/L and 3 g meat extract/L at 37 °C for 18 hours to yield a cell concentration of ~10^9 CFU/mL. *E. coli* cells were cultured in Lysogeny Broth (LB) at 37 °C for 24 hours to yield a cell concentration of ~10^9 CFU/mL. Both *S. epidermidis* and *E. coli* cells were cleaned with the sterilized phosphate-buffered saline (PBS) (pH = 7.4) by centrifugation (4000 rpm for 10 minutes). The final bacterial concentration for bactericidal experiments was adjusted to ~10^7 CFU/mL by gradient dilution using the PBS buffer.

Typically, 1.5 mg photocatalyst was added into a quartz cuvette containing a 3 mL bacterial solution (10^7 CFU/mL). The bacteria and photocatalyst were sufficiently mixed at room temperature and irradiated under the simulated solar light at a density of 100 mW/cm^2. The lamp (Xe arc lamp, Newport Corporation, 450 W) was also equipped with a water filter (Newport Corporation 6123NS) to remove unwanted IR light and resultant heat, as well as an ultraviolet (UV) cut-off filter (Edmund Optics, 390 nm) to limit the lethal UV exposure to the bacteria. After exposure to the light at various times (15-60 minutes), a 100 μL mixture was pipetted out. The bacterial concentration was determined by the standard plate counting method. The agar plates containing the collected bacteria with a series of dilutions were incubated at 37 °C overnight for enumeration. The control experiments were conducted in the absence of light irradiation in the same situations. The bacterial inactivation efficiency (E) was calculated by the following equation:

$$E = \log\frac{C}{C_0} \tag{5.2}$$

where C and C_0 are the bacterial concentrations of the samples taken at a certain time and before the light irradiation, respectively.

ROS determination and measurements The species of ROS were determined by the scavenger test, where various trapping agents were added to the photoreactor during the reaction.[261] Specifically, isopropyl alcohol (IPA, 0.2 ml), catalase (10 units/ml), and p-benzoquinone (p-BQ, 33.3 μM) were used as the scavengers for ·OH, H_2O_2, and $\cdot O_2^-$, respectively.[261, 262] To exclude the toxicity effects of the scavenger agents (*e.g.*, p-benzoquinone) on the bacterial cells, the photocatalytic experiments were performed in the same situation but with a replacement of dye Rhodamine B.

Bacterial staining The bacterial cells were visualized by using a fluorescence microscope. Specifically, 1 ml bacterial cell suspension was centrifuged and resuspended in 10 μL of PBS solution, which was subsequently stained by a live/dead staining kit (Molecular Probes, Invitrogen) in the dark for 1 hour. Bacterial cells with intact cell membranes (live) were stained by SYTO 9 and fluorescent green, whereas propidium iodide (PI) penetrates only damaged membranes and stains the dead bacterial cells, which emits red fluorescence.[255, 263]

Bacterial Immobilization Bacterial immobilization is important as a small movement during AFM imaging in a fluid will lead to unstable and even incorrect results.[264] To firmly fix the bacterial cells on the substrate, the following treatments were applied.[254] Specifically, the overnight cultured bacterial cells were washed three times with PBS with centrifugation at 4000 rpm for 10 minutes. Then, the collected pellets were resuspended in a 1 mL PBS solution and treated with 1-ethyl-3-(3dimethylaminopropyl) (EDC, 1 mg/mL) and N-hydroxysuccinimide (NHS, 2 mg/mL) for 10 minutes. After EDC and NHS treatments, the carboxyl groups on the bacterial surface convert into amine-active succinimidyl esters. A drop of the above bacterial suspension (40 μL) was placed on a poly-L-lysine treated glass slide for 20 minutes and rinsed with DI water sufficiently to remove the loosely attached bacteria. In this case, the remained bacterial cells were firmly immobilized on the surface by an amine-coupling reaction between the succinimidyl esters on the outer cell membrane and primary amines on the poly-L-lysine coating the glass slide.

AFM Force-Curve Measurement in Fluid Typical AFM measurements were conducted in the air. However, the capillary force will result from the condensation of water vapor between the bacterial surface and the AFM tip during the contact.[265] This capillary meniscus will load an additional normal force on the tip, which will lead to errors in the interpretation of the

mechanical results.[265] To eliminate the capillary effects, all the force-curve measurements were carried out at room temperature in PBS solution, using a Dimension Icon AFM (Bruker Corporation) with the peak force tapping mode (PeakForce-Quantitative Nano-Mechanics). A tip of SCANAYST-FLUID+ (Bruker) with a spring constant of ~0.7 N/m was utilized. Before each experiment, the spring constant and the deflection sensitivity were calibrated using the "touch calibration" method. The trig threshold force (peak force setpoint) was set to 2.0 nN to get enough indentation on the bacterial surface. The scan rate was adjusted to 1 Hz and the peak force amplitude was set to 150 nm to obtain the stable force curves. The images were recorded at 128 pixels × 128 pixels with a driving frequency of 1 kHz. Data processing was performed using the commercial Nanoscope Analysis 2.0 software (Bruker AXS Corporation). 16 pairs of "approach" and "retract" data were extracted and averaged from the force volume image for further analysis.

5.3 Results and Discussions

The C-M-Q photocatalyst was rationally designed and fabricated by coating a layer of polymeric QAC, that is QDMAEMA (Q) with a positive charge, on the surface of the bare C-M photocatalyst via the ATRP approach.[181, 255] The C-M is producing ROS upon light irradiation, which is composed of two components. One is graphite-like carbon nitride g-C_3N_4 (C), a metal-free two-dimensional semiconductor photocatalyst.[260] The other one is a titanium-based MOF MIL-125-NH_2 (M), a highly porous crystalline photocatalyst with a large surface area.[266] Both g-C_3N_4 and MIL-125-NH_2 have been widely used in various photocatalytic applications because they are bio-compatible, water-stable, and visible-light responsive.[1, 220, 267] However, when using g-C_3N_4 or MIL-125-NH_2 individually, the high recombination rate of electron-hole (e^--h^+) pair is the main factor limiting its photocatalytic efficiency.[268] Construction of heterojunction is widely

used to lower the recombination rate, thus, improving the photocatalytic activity.[268, 269] Therefore, the hybrid g-C_3N_4/MIL-125-NH_2 (C-M) is synthesized as a bare photocatalyst in this study. Besides photocatalyst, the layer of positively charged polymer polymeric QDMAEME (Q) anchored on the C-M surface is the key to photocatalytic disinfection in this study. This positively charged Q layer can attract the negatively charged bacteria moving towards the C-M surface, which will help make full use of ROS species during the photocatalysis reactions by shortening the distance between the ROS and bacterial cells in the biointerface. Moreover, the Q itself is a well-known broad-spectrum bactericidal agent, which can destroy the bacterial membranes via strong electrostatic interaction.[188, 270] Thus, it is expected such material design will significantly improve the photocatalytic disinfection performance.

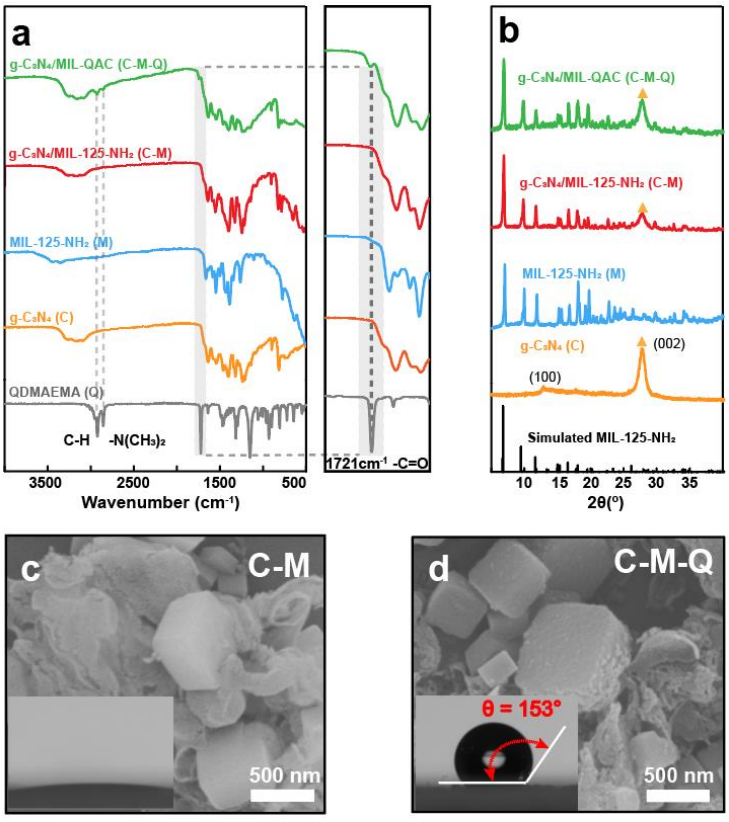

Figure 5.1 PXRD patterns (a) and FT-IR spectra (b) of the materials. SEM images of C-M (c) and C-M-Q (d). Insects in (c, d) are the water contact angle images. Scale bar in (c, d): 500 nm.

The representative samples, *i.e.*, the as-synthesized C-M, Q, and C-M-Q, were first subjected to detailed characterization. **Figure 5.1a** shows the evolution of functional groups during C-M-Q synthesis. The as-prepared bare photocatalyst C-M (red line) contains vibrational bands from both g-C_3N_4 (C, yellow line) and MIL-125-NH_2 (M, blue line), which indicates the co-existence of g-C_3N_4 (C) and MOF (MIL-125-NH_2, M) in the composite. After QAC coating on the C-M surface via the ATRP process, a new peak at 1721 cm^{-1}, which is attributed to the C=O stretching vibration of easter groups from QDMAEMA, is found in C-M-Q (**Figure 5.1a**, grey area); besides, two additional peaks at 2822 cm^{-1} and 2770 cm^{-1} are also observed in C-M-Q, which are assigned to the -$N(CH_3)_2$ symmetric and asymmetric vibrations from the monomer QDMAEMA, respectively.[217, 255] Therefore, it can be concluded that the QDMAEMA has been successfully polymerized and grafted on to the C-M heterostructure photocatalyst via the ATRP approach.

In addition to the surface chemistry, the crystalline structures were examined by the PXRD. As shown in **Figure 5.1b**, the PXRD pattern of as-synthesized MIL-125-NH_2 is well consistent with the simulated one, where the characteristic peaks at 6.8°, 9.5°, and 11.6° are ascribed to the (101), (200), and (211) crystal planes, respectively.[271] For g-C_3N_4, the peaks at 11.1° ((100) crystal plane) and 27.7° ((002) crystal plane) correspond to the two-dimensional (2D) graphic structure, which matches well with the previous study.[254] When forming C-M heterogeneous structure, crystalline phase compositions from both g-C_3N_4 and MIL-125-NH_2 were maintained. Furthermore, after the ATRP process, the C-M-Q shows a similar PXRD pattern to the C-M, indicating the QAC modification does not change the crystalline structure of g-C_3N_4 and MIL-125-NH_2 in the C-M-Q composite.

The morphologies of C-M and C-M-Q were observed by SEM, as shown in **Figure 5.1(c, d)**. For C-M, the lamellar structure g-C_3N_4 was aggregated and injunction with plate-like crystals of MIL-125-NH_2, forming the heterogeneous structure photocatalyst. Before QAC modification, the crystal M in C-M has sharp edges and flat smooth surfaces. (**Figure 5.1c**) After QAC coating with the ATRP process, the initiator molecules (*i.e.*, BIBB) will be firstly anchored on the -NH_2 sites from MIL-125-NH_2 crystal, which is subsequently followed by the continuous QAC polymerization. Therefore, a rough amorphous-phase layer of QAC is observed on the surface of the MIL-125-NH_2 crystal surface in the C-M-Q composite, as shown in **Figure 5.1d**. According to the thermogravimetric analysis (TGA), the weight percentage of QAC loading was finally estimated to be 17.4%. The hydrophobicity of the C-M was also significantly changed because the coated polymeric QAC layer contains a long alkyl chain length (n = 8).[217] As shown in the insect in **Figure 5.1(c, d)**, the C-M-Q exhibited a superhydrophobic surface with a WCA of 153° while C-M showed a hydrophilic surface with a WCA of 0°. The above results once again confirmed the successful QAC decoration on the C-M surface.

The bacterial inactivation experiments were conducted using C-M and C-M-Q in an aqueous PBS solution (pH = 7.4) under light irradiation. To eliminate the lethal influence of UV light on the bacterial cells, the Xe lamp was equipped with a UV cut-off filter. In addition, a water filter (Newport, 6123NS) was also placed in front of the photoreactor to prevent IR exposure from the Xe lamp.[272] After UV and IR light filtering, the light source lies in the visible light range, which is considered safe for bacteria.[273] As expected in **Figure 5.2(a, b)**, negligible bactericidal activities are observed in both *S. epidermidis* and *E. coli*, compared to the control groups (bacteria in dark without photocatalyst), indicating the light source used in this study is not harmful to bacterial cells. Since similar photocatalytic disinfection performances were

observed on both *S. epidermidis* and *E. coli*, we will mainly use *S. epidermis* for demonstration. As illustrated in **Figure 5.2a**, the C-M photocatalyst in the dark exhibited an unnoticeable reduction of bacterial cells, whereas it reaches a 1.5 logs reduction of *S. epidermidis* under the light irradiation, suggesting the bactericidal activity is mainly due to the photo-generated ROS in the solution rather than the toxicity of photocatalyst itself. For C-M-Q in the dark, where a layer of positively-charged QAC polymer coating surrounds the C-M photocatalyst, the QAC layer can achieve a 1.5 logs reduction of *S. epidermis* via the contact-killing mechanism.[214] When the light is further applied, a significantly boosted photocatalytic bactericidal efficiency of 3.2 logs reduction of *S. epidermis* is obtained. Even though the bactericidal activities of C-M-Q come from the contributions of both photo-generated ROS in the aqueous and positively-charged QAC layer, the efficacy of 3.2 logs is still higher than the calculated 2.48 logs, where ROS and QAC are assumed to kill bacteria independently. Similar photocatalytic bacterial inactivation activity is also observed for the Gram-negative bacteria *E. coli*. Therefore, in the biointerface, the cooperative antibacterial behaviors from photo-generated ROS and positively charged QAC layer must play a significant role in improving the overall bactericidal activities. To reveal the mechanism of photocatalytic disinfection using C-M-Q, analysis will be carried out from the following aspects. (i) Photocatalytic performance of C-M; (ii) Charge effects of QAC; (iii) Bacteria-photocatalyst contact interaction in biointerface.

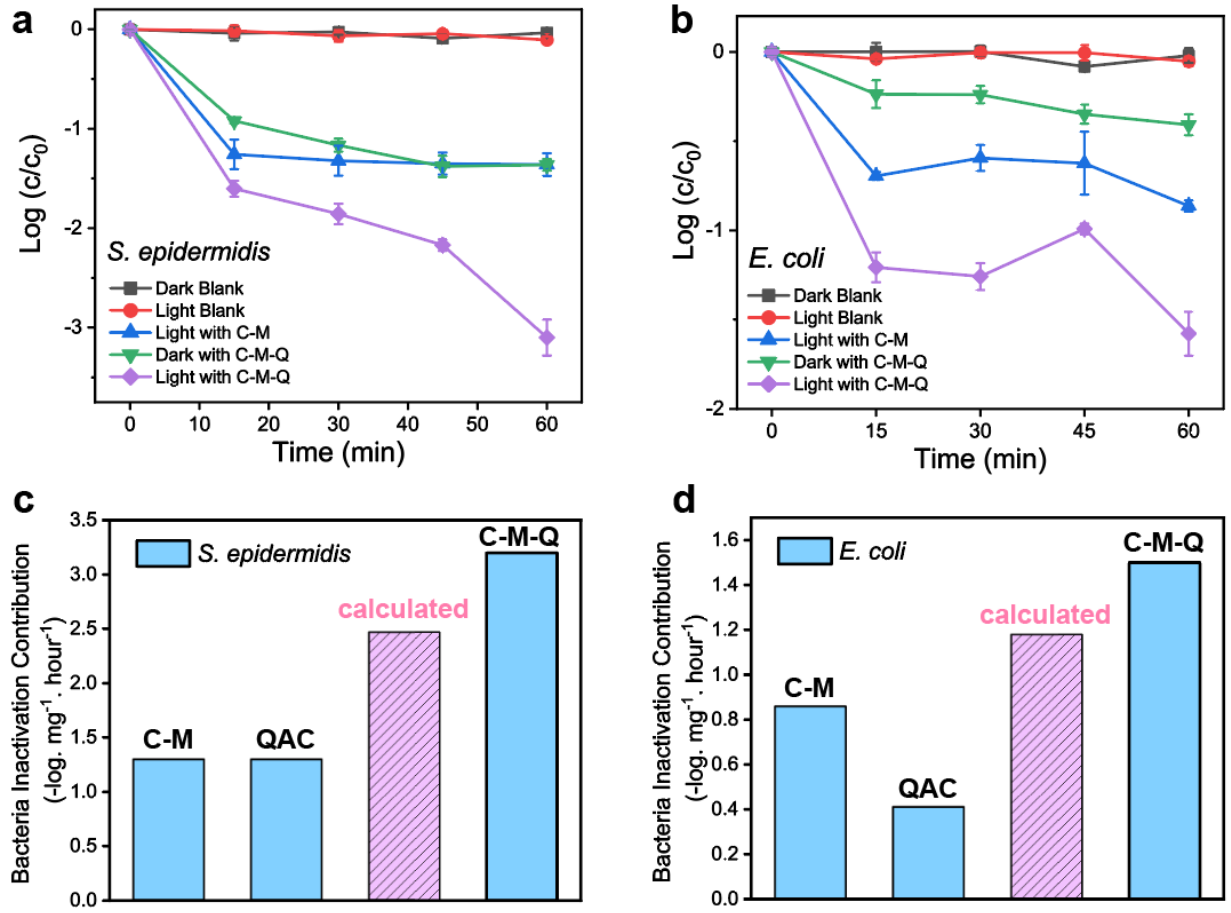

Figure 5.2 Bactericidal activities for Gram-positive *S. epidermidis* (a) and Gram-negative *E. coli* (b) under different conditions. Contribution of different components in C-M-Q for photocatalytic disinfection on Gram-positive *S. epidermidis* (c) and Gram-negative *E. coli* (d).

In C-M-Q, heterogeneous structure C-M is served as the photocatalyst to generate ROS under visible light irradiation. When used alone, either g-C_3N_4 or MIL-125-NH_2 suffers from poor photocatalytic activity because of the fast recombination rate of electro-hole pairs.[267] But forming a heterojunction with appropriate band structure, charge transfer with photocatalyst will be promoted; thus the photocatalytic performance will improve.[266] To determine the band structure of C-M, the method proposed by Kraut et al. was applied to calculate the band alignment between g-C_3N_4 and MIL-125-NH_2.[274] The core-level energy and upper edge of the valence band (VB) were obtained from XPS measurements (**Figure 5.3(a-c)**). The bandgaps

were determined from the UV-Vis analysis (**Figure 5.3d**). The valence band offset, VBO, can be calculated with the following equation,

$$VBO = \left(E_{N-cole}^{bulk} - E_{N-valence}^{bulk}\right) - \left(E_{Ti-cole}^{bulk} - E_{Ti-valence}^{bulk}\right) - \left(E_{N-cole}^{composite} - E_{Ti-cole}^{composite}\right) \quad (5.3)$$

The conduction band offset (CBO) can be determined by:

$$CBO = BG_{g-C_3N_4} + VBO - BG_{MIL-125-NH_2} \quad (5.4)$$

Where E_{N-cole}^{bulk} and $E_{Ti-cole}^{bulk}$ are the core-level energies of bulk g-C_3N_4 (C) and MIL-125-NH_2 (M), respectively; $E_{N-valence}^{bulk}$ and $E_{Ti-valence}^{bulk}$ are the upper edges of VBs of g-C_3N_4 and MIL-125-NH_2, respectively. $E_{N-cole}^{composite} - E_{Ti-cole}^{composite}$ indicates the core-level energy difference in the g-C_3N_4/MIL-125-NH_2 (C-M) photocatalyst.

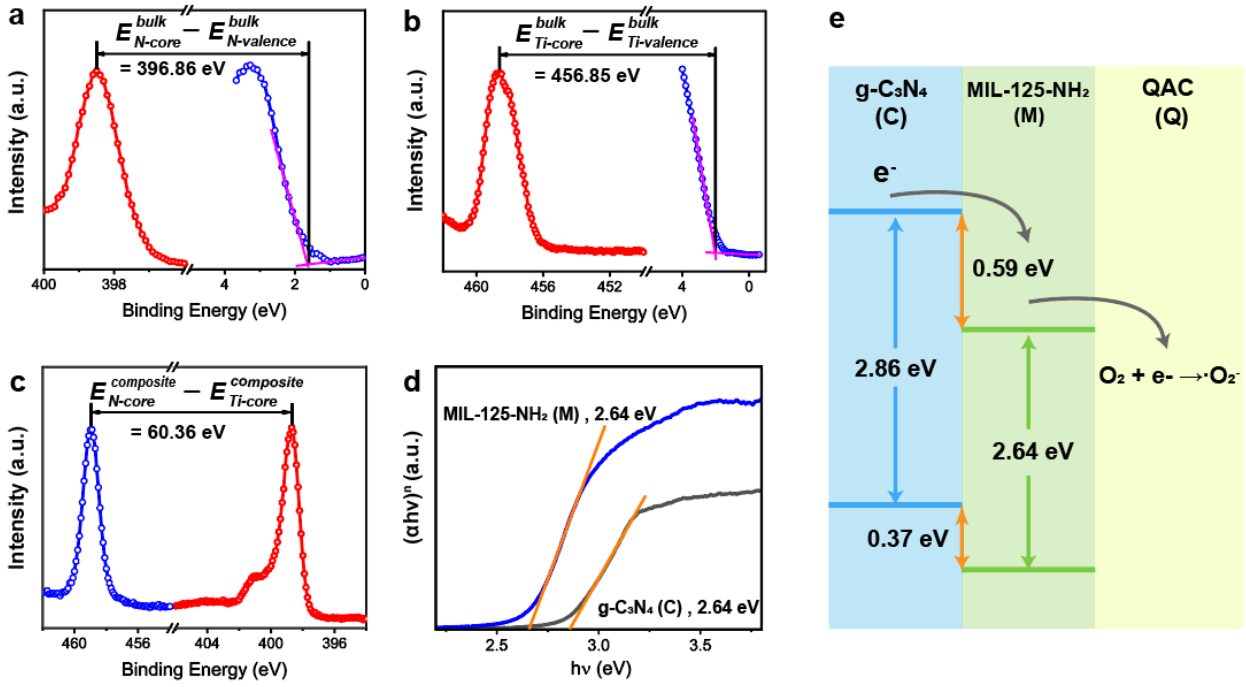

Figure 5.3 XPS valence band and core-level spectra of (a) pure bulk g-C_3N_4 (C), (b) pure bulk MIL-125-NH_2 (M), and (c) g-C_3N_4/MIL-125-NH_2 (C-M) composite; (d) Tauc plots of pure bulk g-C_3N_4 (C) and MIL-125-NH_2 (M); (e) schematic illustration of charge transfer in C-M-Q.

With the aforementioned information, the precise band alignment in the C-M was obtained and is schematically shown in **Figure 5.3e**. Typically, the generation of •OH is thermodynamically unfavorable due to the deficient valence band potential of g-C_3N_4 (2.09 V vs. NHE).[266] On the other hand, the photoelectron on the conduction band of g-C_3N_4 (-0.81 V vs. NHE) is negative enough to reduce surface adsorbed O_2 to $\cdot O_2^-$ ($O_2 + e^- \rightarrow \cdot O_2^-$, -0.33 V vs. NHE).[275] With a more negative conduction band of g-C_3N_4, the photogenerated electrons on g-C_3N_4 can migrate to MIL-125-NH_2 to react with O_2. The efficient transfer of carriers between g-C_3N_4 and MIL-125-NH_2 highly remediates the electron-hole recombination and contributes to the higher charge carrier density.[266]

To determine the ROS species during photosynthesis, a ROS-scavenger approach was used where various radical scavengers in the PBS solution along with the photocatalyst C-M.[262] Specifically, isopropyl alcohol (IPA, 0.2 ml), catalase (CAT, 10 mM), and p-benzoquinone (p-BQ, 33.3 μM) were selected as the scavengers for ·OH, H_2O_2, and $\cdot O_2^-$, respectively.[262] Considering the IPA and p-BQ are toxic bacterial cells, which will result in errors in the analysis of results.[276] We replace the bacterial cells with a widely used model dye molecule, that is Rhodamine B, in the photocatalytic system.[277] The ROS species will be determined by analyzing the photocatalytic degradation of Rhodamine B. The photocatalytic degradation efficiency of Rhodamine B was achieved at 100%, 100%, and 9.7% with the presence of IPA, CAT, and p-BQ, respectively. As expected, the $\cdot O_2^-$ is the most dominant species in the photocatalytic system, as the addition of the $\cdot O_2^-$ scavengers (i.e., p-BQ) resulted in negligible photocatalytic degradation of Rhodamine B. These results are also in agreement with the band analysis of C-M in **Figure 5.3e.** Quantification of $\cdot O_2^-$ were carried out with an indirect method, where the resultant product H_2O_2 was measured using the well-known DMP method. The photocatalytic generated $\cdot O_2^-$ for

C-M and C-M-Q were determined to be 20.64 μM and 18.34 μM, respectively. Both values are much larger than either g-C_3N_4 (2.16 μM) or MIL-125-NH_2 (14.14 μM), demonstrating the C-M heterojunction did improve the photocatalysis. Negligible difference was observed on $\cdot O_2^-$ level between C-M and C-M-Q, indicating that the C-M heterostructure photocatalyst maintains its photocatalytic ROS generation after QAC modification.

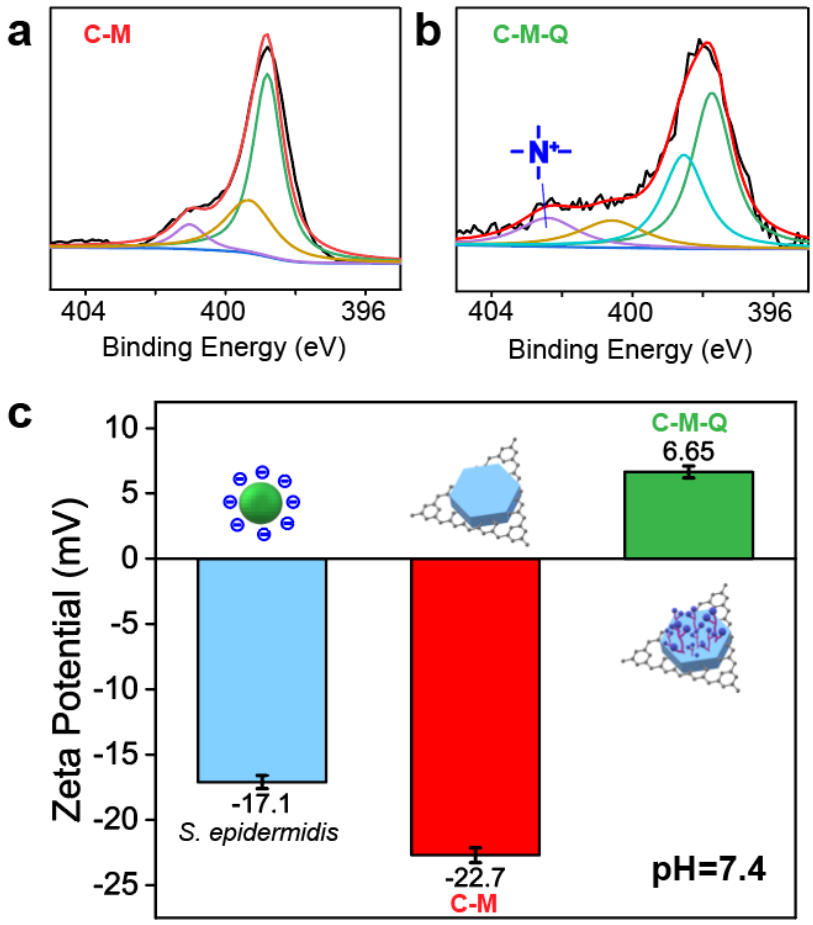

Figure 5.4 XPS spectra of N 1s of C-M and C-M-Q; (c) zeta potential of *S. epidermidis*, C-M, and C-M-Q in PBS buffer (pH = 7.4).

To elucidate the charge distribution of QAC on the photocatalyst, the near-surface elemental composition of the C-M and C-M-Q were firstly determined by XPS measurements in the dry state. **Figure 5.4(a, b)** shows the deconvoluted N1s core level peaks of C-M and C-M-Q.

Both C-M and C-M-Q have three peaks at the same binding energies of 398.7 eV, 400.1 eV, and 401.2 eV, which are assigned to sp^2-hybridized nitrogen (C–N=C), sp^3-hybridized nitrogen in tertiary amine ($N–(C)_3$) and sp^3-hybridized nitrogen in secondary amine ($H–N–(C)_2$), respectively.[278] The additional minor peak at 402.5 eV in C-M-Q corresponds to the quaternary nitrogen from QDMAEMA (NR_4^+), once again indicative of the successful surface attachment of QAC on C-M during the ATRP process.[270] By curve fitting of the high-resolution N 1s XPS spectra, the relative area percentage of quaternary nitrogen NR_4^+ is calculated to be 12.4%. The relatively low percentage of quaternary nitrogen on C-M-Q surface is probably caused by the g-C_3N_4 nanosheets wrapping around the composite, which leaves fewer QAC moieties on MIL-125-NH_2 to be counted within the detection limit of XPS (thickness: 0~7-10 nm).[270]

Considering in photocatalyst disinfection system particles and bacterial cells are immersed in the water, the surface charge of these particles can be investigated by the Zeta-potential (ζ-potential). Typically, an electrically charged particle attracts a thin layer of oppositely charged particles and firmly binds to it, forming a thin liquid layer known as the Stern layer; when the particle diffuses in solution, it will then diffuse into an outer diffuse layer consisting of loosely connected ions, forming an electrical double layer.[279] The surface charge variation between C-M and C-M-Q in PBS buffer (pH = 7.4) is more significant as compared to the dry state, as shown in **Figure 5.4c**. The C-M has a negative ζ-potential of -22.7 mV while C-M-Q has a positive ζ-potential of 6.65 mV. It is because this layer of positively-charged QAC on the C-M-Q surface significantly alters the photocatalyst (*i.e.*, C-M) from negatively to positively charged. Moreover, the *S. epidermidis* with a ζ-potential of -17.1 mV, like most bacterial cells in nature, are negatively charged due to the rich components of carboxylic, amino, and phosphate groups in the cell wall. [181, 255, 256] According to the well-known Derjaguin, Landau, Verwey,

Overbeek (DLVO) theory, which is used to quantitatively describes the force between charged interfaces in an aqueous solution, the electrostatic force (F_{el}) can be determined with the following simplified equation:[280, 281]

$$F_{el} = \frac{4\pi R\sigma_1\sigma_2\lambda_D}{\varepsilon_e\varepsilon_0} e^{-\frac{d}{\lambda_D}} \quad (5.5)$$

where R is the apex radius of material 1; σ_1 and σ_2 represent the surface charge density of the material 1 and material 2, respectively; λ_D is the Debye length; ε_0 is the vacuum permittivity; ε_e is the dielectric permittivity of the electrolyte; and d is the distance between the two surfaces. Therefore, the opposite ζ-potential surface charge creates the driving force for the electrostatic attraction between the C-M-Q and bacterial cells in the biointerface.

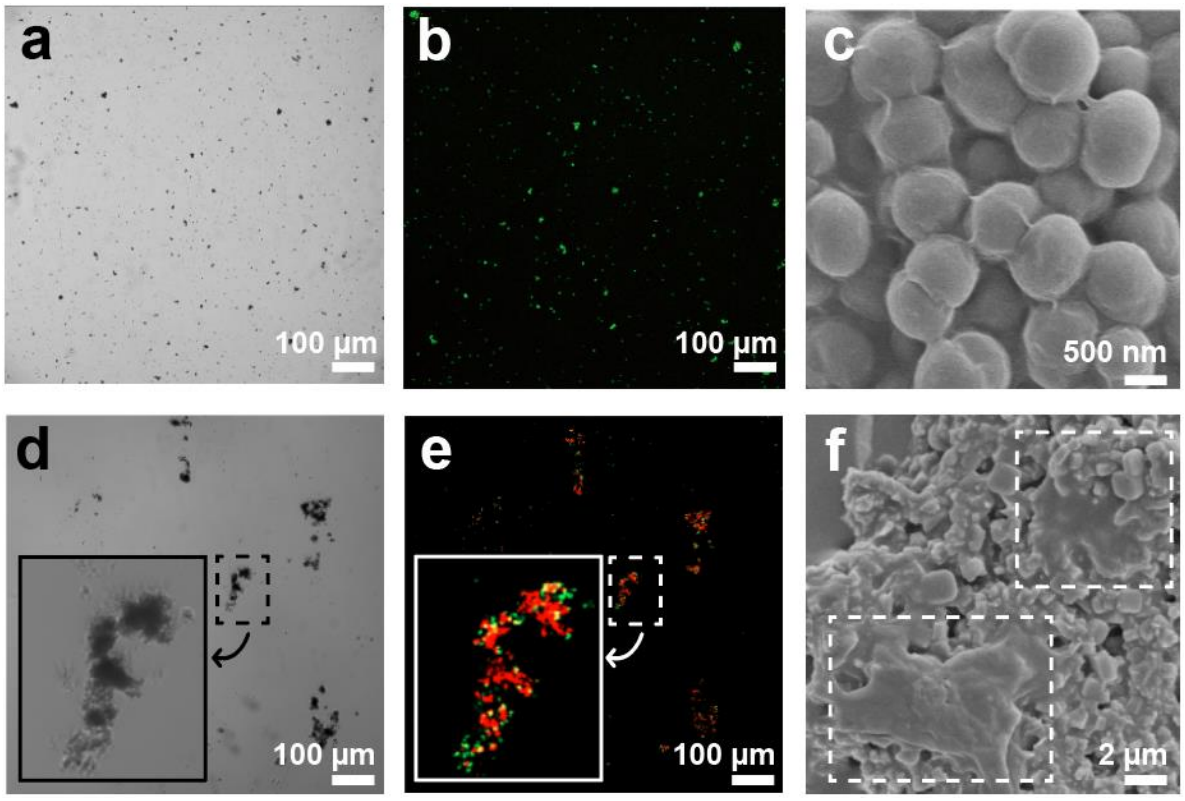

Figure 5.5 Optical (a, d), confocal (b, e), and SEM (c, f) images of interactions in the biointerface. C-M and *S. epidermidis*: (a-c); C-M-Q and *S. epidermidis* (d-f).

To investigate the bacterial behaviors in the biointerface, bacterial cells were stained by the STYO/PI dye, which was subsequently visualized along with the materials under the CLSM observation. **Figure 5.5** shows *S. epidermidis* cells interact with C-M (**Figure 5.5(a-c)**) and C-M-Q (**Figure 5.5(d-f)**) in dark for 1 hour. For C-M with a negative ζ-potential of -22.7 mV, the negatively charged *S. epidermidis* cells are uniformly dispersed along with C-M particles in the PBS solution, but without significant affinity towards the C-M surface, as shown in **Figure 5.5a**. This is because both *S. epidermidis* cells and C-M particles are negatively charged, which generates a repulsive electrostatic force to keep each other apart (**Figure 5.4c**). After 1 hour of interaction with C-M in the dark, most *S. epidermidis* cells are alive and emit green fluorescence (**Figure 5.5b**), which is in agreement with the above CFU counting results in **Figure 5.2a**. Moreover, the cell membranes of *S. epidermidis* are intact after C-M treatment under the SEM observation in **Figure 5.5c**, indicating the C-M, as well as its surface, cause little impact on the cell structures in the biointerface. For C-M-Q with a positive ζ-potential of +6.65 mV, strong hetero-aggregation in the mixtures of *S. epidermidis* cells and C-M-Q particles with opposite charge was observed in the biointerface, which is shown in **Figure 5.5d**. The QAC layer outside the C-M-Q cannot only attract bacterial cells moving towards its surface, but also can destroy the cell membranes via the strong electrostatic force. After 1 hour of treatment with the C-M-Q in the PBS solution, *S. epidermidis* cells in the biointerface but with closer contact on the C-M-Q surface (insect in **Figure 5.5e**) are mostly dead and emit red fluorescence.[188, 270] Exposed to the strong electrostatic force, the cell membranes are eventually destroyed and the cytoplasmatic is spread over the C-M-Q surface, as seen in **Figure 5.5f**. For those bacterial cells far away from the C-M-Q surface, most of them are still alive and emit green fluorescence because the relatively further distance dramatically reduced electrostatic interactions.

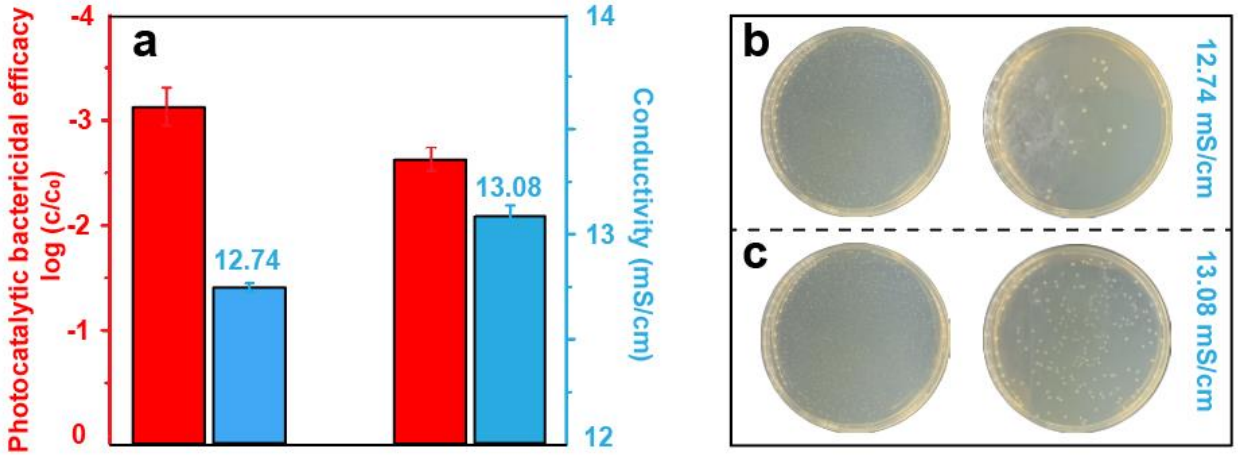

Figure 5.6. **(**a) Photocatalytic disinfection performance and conductivity of PBS solution with and without Ca^{2+} and Mg^{2+} addition. (b) CFU assays of *S. epidermidis* cells in PBS without Ca^{2+} and Mg^{2+}; (c) CFU assays of *S. epidermidis* cells in PBS containing Ca^{2+} and Mg^{2+}.

Besides the bacterial cells movement in the biointerface, we also explored how the positively charged QAC layer impacts photocatalytic bactericidal performance. In the photocatalytic disinfection system, C-M-Q particles and *S. epidermidis* cells contain the opposite charge. The hetero-aggregation process, namely the coagulation between C-M-Q particles and bacterial cells, is depressed by increasing the ionic strength according to the DLVO theory.[282, 283] To reduce the attractive interaction in the biointerface but maintain the viability of bacterial cells, we added extra Ca^{2+} (100 mg/L) and Mg^{2+} (100 mg/L) in the PBS solution to increase the ionic strength. The conductivity has increased from the original PBS solution of 12.74 mS/cm to the enhanced 13.08 mS/cm (**Figure 5.6a**). The existence of Ca^{2+} and Mg^{2+} in the new PBS solution (pH=7.4) are safe for bacterial cells, which can be reflected in the almost same level of CFU counting results in the control experiment (**Figure 5.6b**). However, the photocatalytic bactericidal efficacy has dropped from 3.2 log to the 2.7 log reduction in the new prepared PBS solution and fewer colonies with the same series dilution were observed on the nutrient agar. This is because the addition of Ca^{2+} and Mg^{2+} in the solution reduces the attraction in the

biointerface, which makes the ROS radicals on the C-M-Q surface travel a longer distance to inactivate bacterial cells.[282]

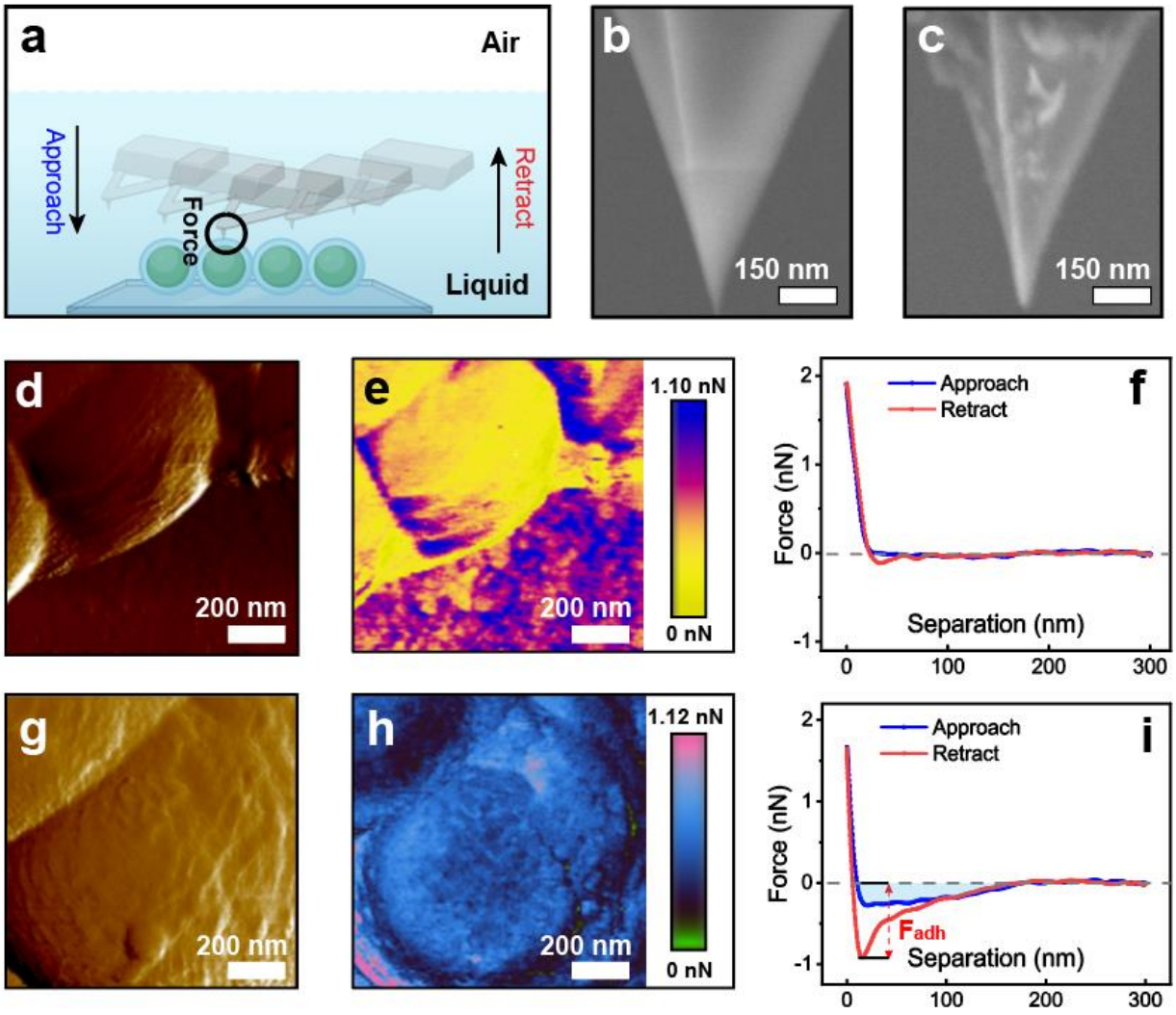

Figure 5.7 AFM force measurement in-between *S. epidermidis* cells and materials. (a) illustration for the AFM force measurement in PBS solution; SEM images of the pristine AFM Si probe (b) and C-M-Q coated AFM Si probe (c); Peak force error image (d), adhesion force mapping (e), and approach-retract force curves (f) of *S. epidermidis* cells using pristine AFM Si probe; Peak force error image (g), adhesion force mapping (h), and approach-retract force curves (i) of *S. epidermidis* cells using pristine AFM Si probe. Scale bar in (b, c): 150 nm.

To further probe the bacteria-photocatalyst interaction in the biointerface, the force between the *S. epidermidis* cells and C-M-Q was investigated via the AFM force spectroscopy in PBS solution (pH 7.4), as illustrated in **Figure 5.7a**. It should be noted that the measurement was carried out in the liquid rather than the air because the capillary forces that arise from the humid coverage of both sample and tip under ambient conditions are significant, which will lead to errors in force data interpretation.[280, 284] In a liquid environment, these capillary forces are absent.[280, 285]. For comparison, the pristine Si probe was functionalized with C-M-Q particles (**Figure 5.7(b, c)**) for the AFM measurement. Due to the presence of the poly-dopamine with a negative charge, the positively charged C-M-Q can be easily coated onto the Si probe (**Figure 5.7c**).[286] Herein, the pristine Si probe without modification was firstly used as a control to understand better the forces between bacterial cells and the AFM probe. **Figure 5.7d** shows the Peak force error image of the *S. epidermidis* cells using a pristine AFM Si probe. The adhesion force mapping was also recorded with a resolution of 128×128 pixels (**Figure 5.7e**). Under the PeakForce QNM mode, each pixel contains two force curves (*i.e.*, approach and retrace). Sixteen randomly collected pixel data sets were averaged for the force-curve imaging. As shown in **Figure 5.7f**, the separation (unit: nm) in the X-axis represents the distance of the AFM Si probe above the *S. epidermidis* surface. The force (unit: nN) in Y-axis represents the interactive force between the AFM Si probe and *S. epidermidis* cells, where the positive sign indicates repulsion and vice versa. During the approach, the interactive force remains zero until the separation distance reaches 25 nm. At this point, the pre-set 2.0 nN force was applied between the pristine Si probe and *S. epidermidis* surface until the separation distance became zero. The distance of 25 nm is also regarded as the deformation of the *S. epidermidis* cells. After the Si probe tip snapped into the bacterial surface, the system starts to retrace the probe from the contact point to far away

(separation = 300 nm). Typically, the value of the Y-axis at the lowest point in the retraction is defined as the adhesion force, which is the net effects of van der Waals force, acid-based interaction, and electrostatic interactions.[258] As shown in the blue line in **Figure 5.7f**, a minor attractive adhesion force of 115 pN was observed in the trace process, which indicates the overall adhesion force is attractive. However, the adhesion force mapping of the *S. epidermidis* cells and force curves measured with a C-M-Q coated Si probe are pretty different (**Figure 5.7(g-i)**). Due to a layer of positively charged QAC on C-M-Q, electrostatic attractive effects were observed earlier than the bare Si probe in the approach curve, which starts at a much higher separation distance from 180 nm (**Figure 5.7i**). Moreover, a significantly increased adhesion force of 972 pN was also obtained in the C-M-Q/bacteria retrace curve, which indicates that, compared to the bare Si probe, the system has to provide larger force to separate the C-M-Q particle and *S. epidermidis* cells at the biointerface. The adhesion force data probed by the AFM between C-M-Q particles and *S. epidermidis* cells is in good agreement with the results observed in confocal images. By bringing the photocatalyst and bacterial cells in close contact, ROS can be generated which can kill the bacteria on its surface.

5.4 Conclusions

In summary, we have successfully developed a C-M-Q photocatalyst with a layer of positively charged QAC polymer-coated outside to improve the photocatalytic bactericidal activity. Experiments demonstrate that the QAC can alter the surface charge into positive and promote the bacteria-photocatalyst adhesion via electrostatic attraction, thus shortening the distance between photogenerated ROS and bacterial cells. Due to the effective usage of photocatalytic ROS generation and bacteria-photocatalyst attraction in the biointerface, the photocatalytic disinfection performance is significantly improved. The as-synthesized C-M-Q

photocatalyst composite shows 3.20 logs of inactivation efficiency for Gram-positive (*S. epidermidis*) and 1.45 logs for Gram-negative (*E. coli*) bacteria within 60 min under the visible light irradiation. This study also provides a new avenue to strengthen the affinity between bacterial cells and photocatalyst in the biointerface via electrostatic attraction for photocatalytic antibacterial applications.

Chapter 6. Conclusions and Future Directions

6.1 Conclusions

In this dissertation, MOF-based functional materials were rationally designed to address air contamination issues, including VOC monitoring, PM removal, and airborne bacterial inactivation. Quantitative interactions between target air pollutants and the MOF-based functional materials were explored systematically with the assistance of advanced instruments, which has gained in-depth knowledge and understanding for future materials designed for better air quality. The detailed conclusions from this dissertation are listed below.

6.1.1 H_2S Sensing

In this dissertation, H_2S was selected as a model VOC for investigation. A novel bimetallic MOF (*i.e.*, Al/Fe-MIL-53-NH_2) was developed to significantly improve its sensing performance towards H_2S molecules based on the fluorescence "turn-on" effect. In Al/Fe-MIL-53-NH_2, Fe^{3+} was rationally incorporated into the parent MOF, that is, Al-MIL-53-NH_2. Because of the solid ligand for metal charge transfer between unpaired electrons in Fe^{3+} and π-conjugated BDC-NH_2 ligands, the Al/Fe-MIL-53-NH_2 showed no fluorescence emission. When exposed to H_2S, Fe^{3+} in the bimetallic MOF seized by S^{2-} facilitated the partial degradation and subsequent release of BDC-NH_2 ligands, which were determined to be real fluorophores that contributed to the fluorescence enhancement. The designed Al/Fe-MIL-53-NH_2 bimetallic MOF shows excellent sensing performance within the low H_2S concentration (0-38.46 μM).

Beyond the improved performance of MOF-based materials, fundamental understandings of interactions between H_2S and MOF-based materials were also discussed. More specifically, the mechanisms of H_2S detection were successfully unraveled, where nitro-MOFs (e.g., Al-MIL-53-NO_2) were used to achieve quantitative fluorescence sensing. The new insights based on the investigations in this dissertation are completely different from what has been reported in

previous studies. The results showed that it is the free BDC-NH_2 (2-aminobenzene-1,4-dicarboxylic acid) in the solution rather than the formation of Al-MIL-53-NH_2 that caused the fluorescence enhancement.

6.1.2 Airborne Microorganisms Inactivation

Airborne bacteria were selected as the presentative airborne microorganism pollutants for disinfection in this dissertation. Several novel antimicrobial MOF-based materials (e.g., UiO-QDMAEMA, C-M-Q) were rationally designed and fabricated to kill bacterial cells. Specifically, QAC polymer, a broad-spectrum antimicrobial agent, was carefully coated onto the surface of MOF-based materials such as UiO-66-NH_2 and g-C_3N_4/MIL-125-NH_2 to form active composites for airborne bacterial inactivation. These composites demonstrated great antibacterial activities where electrostatic contact-killing and photogenerated reactive oxygen species (ROS) are utilized for efficient disinfection. In-depth investigations on the biointerface were carried out with the aid of several advanced techniques, such as the Zeta-potential analyzer, fluorescence laser confocal microscope (CLSM), and atomic force microscope (AFM). The results showed that the adhesion of bacterial cells towards the photocatalyst surface leads to significantly enhanced photocatalytic bactericidal efficiencies.

6.2 Future Directions

Although several breakthroughs have been demonstrated in this dissertation and considerable related work has been reported in previous studies to improve the MOF-based functional materials for air quality control and improvement, additional work is still needed regarding the following aspects:

(1) The environment of the air pollutants is sometimes harsh. The physical and chemical stability, reliability, biocompatibility, and recycling capability of MOF-based functional materials or devices should be carefully examined and improved.

(2) Achieving multiple functions at the MOF-based materials to address air contamination is a promising approach, but it is also very challenging. For example, coating polymers around MOF-based materials will reduce the specific surface areas and occupies the pore volume, which will have adverse effects on the gas adsorption. Therefore, “trade-off” effects should be seriously considered in the material design.

(3) To design MOF-based materials with high performance on the specific air pollutants, the physical, chemical, and biological properties of the target pollutants should be always examined. Particularly, interfaces between MOF-based materials and targets should be always considered from the molecular or atomic level.

Appendix: Vita

EDUCATION

B.S., Materials Science, Huazhong University of Science and Technology, China, 2013
M.S., Optical Engineering, Beijing University of Technology, China, 2016
PhD student, Mechanical & Nuclear Engineering, Virginia Commonwealth University, 2017-2022.05.13 (Expected)

PUBLICATIONS (14 in total)

1. ***Zhu, Z.,*** Zhang, Y., Bao, L., Chen, J.P., Duan, S., Chen., S.C., Xu, P., & Wang, W. N. (2021). Self-Decontaminating Nanofibrous Filters for Efficient Particulate Matter Removal and Airborne Bacteria Inactivation. *Environmental Science: Nano. 8.4 (2021): 1081-1095.* ***(IF: 7.683)***
2. ***Zhu, Z.,*** He, X., & Wang, W. N. (2020). Unraveling the origin of the "Turn-On" effect of Al-MIL-53-NO_2 during H_2S detection. *CrystEngComm*, *22*(2), 195-204. ***(IF: 3.117)***
3. ***Zhu, Z.,*** Natarajan, V., & Wang, W. N. (2020). The role of Fe^{3+} ions in fluorescence detection of H_2S by a bimetallic metal-organic framework. *Journal of Solid-State Chemistry*, 288, 121434. (***IF: 2.726***)
4. ***Zhu, Z.,*** Bao, L., Xu, P., & Wang, W. N. (2022) Biointerface Matters: Smart Charge Integration on Heterogeneous Photocatalyst Surface to Boost Photocatalytic Disinfection Activity. (In submission)
5. ***Zhu, Z.,*** Liu, F. R., Wang, Z. M., Fan, Z. K., Liu, F., & Sun, N. X. (2015). Comparative study on crystallization characteristics of amorphous $Ge_2Sb_2Te_5$ films by an ultraviolet laser radiation and isothermal annealing. *Applied Surface Science*, 335, 184-188. (***IF: 6.182***)
6. ***Zhu, Z.,*** Liu, F. R., Yang, J. F., Fan, Z. K., Liu, F., & Sun, N. X. (2016). A cross sectional study on the crystallization of amorphous $Ge_2Sb_2Te_5$ films induced by a single-pulse ultraviolet laser. *Optics & Laser Technology*, 81, 100-106. (***IF: 3.233***)
7. Chen, J., ***Zhu, Z.,*** & Wang, W. N. (2021). Towards addressing environmental challenges: rational design of metal-organic frameworks-based photocatalysts via a microdroplet approach. *Journal of Physics: Energy*.
8. Zhang, Y., He, X., ***Zhu, Z.***, Wang, W. N., & Chen, S. C. (2021). Simultaneous removal of VOCs and PM2.5 by metal-organic framework coated electret filter media. *Journal of Membrane Science*, 618, 118629. **(*IF: 7.183*)**
9. He, X., Chen, J., Albin, S., ***Zhu, Z.,*** & Wang, W. N. (2021). Data-driven parameter optimization for the synthesis of high-quality zeolitic imidazolate frameworks via a microdroplet route. *Advanced Powder Technology*, 32(1), 266-271. ***(IF: 4.217)***
10. He, X., Nguyen, V., Jiang, Z., Wang, D., ***Zhu, Z.,*** & Wang, W. N. (2018). Highly-oriented one-dimensional MOF-semiconductor nanoarrays for efficient photodegradation of antibiotics. *Catalysis Science & Technology*, 8(8), 2117-2123. (***IF: 5.721***)
11. Wang, D., Zhu, B., He, X., ***Zhu, Z.,*** Hutchins, G., Xu, P., & Wang, W. N. (2018). Iron oxide nanowire-based filter for inactivation of airborne bacteria. *Environmental Science: Nano*, 5(5), 1096-1106. (***IF: 7.683***)
12. Bai, N., Liu, F. R., Han, X. X., ***Zhu, Z.***, Liu, F., Lin, X., & Sun, N. X. (2015). Effect of the Sn dopant on the crystallization of amorphous $Ge_2Sb_2Te_5$ films induced by an excimer laser.

Optics & Laser Technology, 74, 11-15. ***(IF: 3.233)***

13. Liu, F. R., Fan, Z. K., ***Zhu, Z.,*** Yang, J. F., Lin, X., Liu, F., & Sun, N. X. (2015). Modeling of the temperature field in the amorphous $Ge_2Sb_2Te_5$ film induced by a picosecond laser with a body heat source. *Applied Surface Science*, 343, 188-193. (***IF: 6.182***)
14. Bai, N., Liu, F. R., Han, X. X., ***Zhu, Z.,*** Liu, F., Lin, X., & Sun, N. X. (2014). A study on the crystallization behavior of Sn-doped amorphous $Ge_2Sb_2Te_5$ by ultraviolet laser radiation. *Applied Surface Science*, 316, 202-206. (***IF: 6.182***)
15. Zhao, J. J., Liu, F. R., Han, X. X., ***Zhu, Z.,*** Lin, X., Liu, F., & Sun, N. X. (2014). Transmission electron microscopy study of amorphous $Ge_2Sb_2Te_5$ films induced by an ultraviolet single-pulse laser. *Applied Surface Science*, 311, 83-88. (***IF: 6.182***)

BOOK Chapter

Zhu, Zan, Jianping Chen, and Wei-Ning Wang. "Artificial Photosynthesis by 3D Graphene-based Composite Photocatalysts." *Graphene-based 3D Macrostructures for Clean Energy and Environmental Applications*. 2021. 396-431.

CONFERENCE Presentations (* Speaker/Presenter)

1. ***Zan Zhu****, Jianping Chen, and Wei-Ning Wang, Rational Development of Metal-organic framework (MOF)-based Bioactive Filters to Combat Air Contamination, 2021 Virginia Academy of Science (VAS) Annual Meeting, May 19-21, 2021 (Virtual)
2. ***Z. Zhu****, W.N. Wang., Smart engineered antibacterial nanofibrous filters for efficient particulate removal and airborne pathogens disinfection. ACS Spring 2021, April 8, 2021 (Oral) Selected as online presentation.
3. ***Z. Zhu****, X. He, and W.N. Wang, Rational design of bimetallic metal-organic frameworks (MOFs) and their applications in environmental science and engineering, 2020 Virginia Academy of Science (VAS) Annual Meeting, James Madison University, Harrisonburg, VA, May 28-30, 2020
4. ***Z. Zhu****, X. He, and W.N. Wang., Did we really use the intrinsic fluorescent properties of nitro-functionalized metal-organic frameworks (MOFs) to realize H_2S detection in an aqueous system? ACS Spring 2020 National Meeting & Expo, Philadelphia, PA, March 22-26, 2020 (online)
5. ***Z. Zhu****, X. He, and W.N. Wang., Exploration of real fluorophores in nitro-functionalized metal-organic frameworks (MOFs) for H_2S detection, International Symposium on Clusters and Nanomaterials (ISCAN), Richmond, VA, November 3-7, 2019 (Poster)

HONORS AND AWARDS

- Outstanding Graduate Research Assistant, Virginia Commonwealth University, 2021
- National Scholarship (China), Beijing University of Technology, 2016
- Beijing Outstanding Graduates, Beijing University of Technology, 2016
- Outstanding Graduates of BJUT, Beijing University of Technology, 2016

SKILLS

- Nano-particles synthesis, characterization, and environmental application

- Experienced in SEM, TEM, AFM, XRD, EDX, XPS, FT-IR, UV-vis, GC, Raman, Fluorescence measurements
- Experienced in electrospinning technique and filter fabrication
- Experienced in particle filtration test

MENTORING EXPERIENCE

Gavin Telfer	Maggie L. Walker Governor's School	2020-2021
Varun Natarajan	Maggie L. Walker Governor's School	2019-2020
Jermaine Cort	VCU, VIP program	2020-2021
Jocelyn Trap	VCU, VIP program	2021-2022
Sydney Wojcieszak	VCU, VIP program	2020 fall
Shane Albin	VCU, VIP program	2019 fall
John Follis	VCU, DERI program	2019-2020
Zoe Manring	VCU, DERI program	2018-2019
Jamara Jones	VCU, summer intern	2019
London Hopkins	VCU, summer intern	2018

Reference:

1. Li, P.; Li, J.; Feng, X.; Li, J.; Hao, Y.; Zhang, J.; Wang, H.; Yin, A.; Zhou, J.; Ma, X.; Wang, B., Metal-organic frameworks with photocatalytic bactericidal activity for integrated air cleaning. *Nat. Commun.* **2019,** *10* (1), 2177.
2. Kroll, J. H.; Heald, C. L.; Cappa, C. D.; Farmer, D. K.; Fry, J. L.; Murphy, J. G.; Steiner, A. L., The complex chemical effects of COVID-19 shutdowns on air quality. *Nat. Chem.* **2020,** *12* (9), 777-779.
3. Prata, J. C.; Reis, V.; da Costa, J. P.; Mouneyrac, C.; Duarte, A. C.; Rocha-Santos, T., Contamination issues as a challenge in quality control and quality assurance in microplastics analytics. *J. Hazard. Mater.* **2021,** *403*, 123660.
4. Fowler, D.; Brimblecombe, P.; Burrows, J.; Heal, M. R.; Grennfelt, P.; Stevenson, D. S.; Jowett, A.; Nemitz, E.; Coyle, M.; Lui, X.; Chang, Y.; Fuller, G. W.; Sutton, M. A.; Klimont, Z.; Unsworth, M. H.; Vieno, M., A chronology of global air quality. **2020,** *378* (2183), 20190314.
5. Rodríguez-Urrego, D.; Rodríguez-Urrego, L., Air quality during the COVID-19: PM2.5 analysis in the 50 most polluted capital cities in the world. *Environ. Pollut.* **2020,** *266*, 115042.
6. Manisalidis, I.; Stavropoulou, E.; Stavropoulos, A.; Bezirtzoglou, E., Environmental and Health Impacts of Air Pollution: A Review. *Front Public Health* **2020,** *8*.
7. Organization, W. H., Ambient air pollution: A global assessment of exposure and burden of disease. *World Health Organization*

2016.
8. Lai, C.; Wang, Z.; Qin, L.; Fu, Y.; Li, B.; Zhang, M.; Liu, S.; Li, L.; Yi, H.; Liu, X.; Zhou, X.; An, N.; An, Z.; Shi, X.; Feng, C., Metal-organic frameworks as burgeoning materials for the capture and sensing of indoor VOCs and radon gases. *Coord. Chem. Rev.* **2021,** *427*, 213565.
9. Anderson, J. O.; Thundiyil, J. G.; Stolbach, A., Clearing the Air: A Review of the Effects of Particulate Matter Air Pollution on Human Health. *J. Med. Toxicol.* **2012,** *8* (2), 166-175.
10. Seaton, A.; Godden, D.; MacNee, W.; Donaldson, K., Particulate air pollution and acute health effects. *The Lancet* **1995,** *345* (8943), 176-178.
11. Giani, P.; Castruccio, S.; Anav, A.; Howard, D.; Hu, W.; Crippa, P., Short-term and long-term health impacts of air pollution reductions from COVID-19 lockdowns in China and Europe: a modelling study. *The Lancet Planetary Health* **2020,** *4* (10), e474-e482.
12. Eze, I. C.; Schaffner, E.; Fischer, E.; Schikowski, T.; Adam, M.; Imboden, M.; Tsai, M.; Carballo, D.; von Eckardstein, A.; Künzli, N.; Schindler, C.; Probst-Hensch, N., Long-term air pollution exposure and diabetes in a population-based Swiss cohort. *Environ. Int.* **2014,** *70*, 95-105.
13. Kelishadi, R.; Poursafa, P., Review paperAir pollution and non-respiratory health hazards for children. *Arch. Med. Sci.* **2010,** *6* (4), 483-495.
14. David, E.; Niculescu, V.-C., Volatile Organic Compounds (VOCs) as Environmental Pollutants: Occurrence and Mitigation Using Nanomaterials. *Int. J. Environ. Res. Public Health* **2021,** *18* (24).
15. Effah, E.; Holopainen, J. K.; McCormick, A. C., Potential roles of volatile organic compounds in plant competition. *Perspect. Plant Ecol. Evol. Syst.* **2019,** *38*, 58-63.

16. Lun, X.; Lin, Y.; Chai, F.; Fan, C.; Li, H.; Liu, J., Reviews of emission of biogenic volatile organic compounds (BVOCs) in Asia. *Journal of Environmental Sciences* **2020,** *95*, 266-277.
17. Britt, D.; Tranchemontagne, D.; Yaghi Omar, M., Metal-organic frameworks with high capacity and selectivity for harmful gases. *Proceedings of the National Academy of Sciences* **2008,** *105* (33), 11623-11627.
18. Bellat, J.-P.; Bezverkhyy, I.; Weber, G.; Royer, S.; Averlant, R.; Giraudon, J.-M.; Lamonier, J.-F., Capture of formaldehyde by adsorption on nanoporous materials. *J. Hazard. Mater.* **2015,** *300*, 711-717.
19. Krishnamurthy, A.; Thakkar, H.; Rownaghi, A. A.; Rezaei, F., Adsorptive Removal of Formaldehyde from Air Using Mixed-Metal Oxides. *Ind. Eng. Chem. Res.* **2018,** *57* (38), 12916-12925.
20. Guidotti, T. L., Hydrogen Sulfide: Advances in Understanding Human Toxicity. *Int. J. Toxicol.* **2010,** *29* (6), 569-581.
21. Zhang, N.; Wang, X.; Geng, L.; Liu, Z.; Zhang, X.; Li, C.; Zhang, D.; Wang, Z.; Zhao, G., Metallic Ni nanoparticles embedded in hierarchical mesoporous Ni(OH)2: A robust and magnetic recyclable catalyst for hydrogenation of 4-nitrophenol under mild conditions. *Polyhedron* **2019,** *164*, 7-12.
22. Luo, Y.; Zheng, Y.; Zuo, J.; Feng, X.; Wang, X.; Zhang, T.; Zhang, K.; Jiang, L., Insights into the high performance of Mn-Co oxides derived from metal-organic frameworks for total toluene oxidation. *J. Hazard. Mater.* **2018,** *349*, 119-127.
23. Héquet, V.; Raillard, C.; Debono, O.; Thévenet, F.; Locoge, N.; Le Coq, L., Photocatalytic oxidation of VOCs at ppb level using a closed-loop reactor: The mixture effect. *Applied Catalysis B: Environmental* **2018,** *226*, 473-486.
24. Bahri, M.; Haghighat, F.; Rohani, S.; Kazemian, H., Metal organic frameworks for gas-phase VOCs removal in a NTP-catalytic reactor. *Chem. Eng. J.* **2017,** *320*, 308-318.
25. Cui, J.; Wong, Y.-L.; Zeller, M.; Hunter, A. D.; Xu, Z., Pd Uptake and H2S Sensing by an Amphoteric Metal–Organic Framework with a Soft Core and Rigid Side Arms. *Angew. Chem. Int. Ed.* **2014,** *53* (52), 14438-14442.
26. Powell, C. R.; Dillon, K. M.; Matson, J. B., A review of hydrogen sulfide (H2S) donors: Chemistry and potential therapeutic applications. *Biochem. Pharmacol.* **2018,** *149*, 110-123.
27. Georgiadis, A. G.; Charisiou, N.; Yentekakis, I. V.; Goula, M. A., Hydrogen Sulfide (H2S) Removal via MOFs. *Materials* **2020,** *13* (16).
28. Nagarkar, S. S.; Desai, A. V.; Ghosh, S. K., A Nitro-Functionalized Metal–Organic Framework as a Reaction-Based Fluorescence Turn-On Probe for Rapid and Selective H2S Detection. *Chemistry – A European Journal* **2015,** *21* (28), 9994-9997.
29. Yu, F.; Han, X.; Chen, L., Fluorescent probes for hydrogen sulfide detection and bioimaging. *Chem. Commun.* **2014,** *50* (82), 12234-12249.
30. Zhang, X.; Hu, Q.; Xia, T.; Zhang, J.; Yang, Y.; Cui, Y.; Chen, B.; Qian, G., Turn-on and Ratiometric Luminescent Sensing of Hydrogen Sulfide Based on Metal–Organic Frameworks. *ACS Appl. Mater. Interfaces* **2016,** *8* (47), 32259-32265.
31. Pandey, S. K.; Kim, K.-H.; Tang, K.-T., A review of sensor-based methods for monitoring hydrogen sulfide. *TrAC Trends in Analytical Chemistry* **2012,** *32*, 87-99.
32. Shin, H.; Kim, D.-H.; Jung, W.; Jang, J.-S.; Kim, Y. H.; Lee, Y.; Chang, K.; Lee, J.; Park, J.; Namkoong, K.; Kim, I.-D., Surface Activity-Tuned Metal Oxide Chemiresistor: Toward Direct and Quantitative Halitosis Diagnosis. *ACS Nano* **2021,** *15* (9), 14207-14217.

33. Bao, J.; Zhang, Z.; Zheng, Y., H2S sensor based on two-dimensional MoO3 nanoflakes: Transition between sulfidation and oxidation. *Sensors and Actuators B: Chemical* **2021,** *345*, 130408.
34. Yamada, T.; Sugiura, H.; Mimura, H.; Kamiya, K.; Osaki, T.; Takeuchi, S., Highly sensitive VOC detectors using insect olfactory receptors reconstituted into lipid bilayers. *Science Advances 7* (3), eabd2013.
35. Yang, L.; Li, C.; Tang, X., The Impact of PM2.5 on the Host Defense of Respiratory System. *Frontiers in Cell and Developmental Biology* **2020,** *8*.
36. Bian, Y.; Chen, C.; Wang, R.; Wang, S.; Pan, Y.; Zhao, B.; Chen, C.; Zhang, L., Effective removal of particles down to 15 nm using scalable metal-organic framework-based nanofiber filters. *Applied Materials Today* **2020,** *20*, 100653.
37. Tang, M.; Thompson, D.; Chen, S.-C.; Liang, Y.; Pui, D. Y. H., Evaluation of different discharging methods on HVAC electret filter media. *Build. Environ.* **2018,** *141*, 206-214.
38. Tien, C.-Y.; Chen, J.-P.; Li, S.; Li, Z.; Zheng, Y.-M.; Peng, A. S.; Zhou, F.; Tsai, C.-J.; Chen, S.-C., Experimental and theoretical analysis of loading characteristics of different electret media with various properties toward the design of ideal depth filtration for nanoparticles and fine particles. *Sep. Purif. Technol.* **2020,** *233*, 116002.
39. Li, S.; Chen, D.-R.; Zhou, F.; Chen, S.-C., Effects of relative humidity and particle hygroscopicity on the initial efficiency and aging characteristics of electret HVAC filter media. *Build. Environ.* **2020,** *171*, 106669.
40. Chang, D.-Q.; Liu, J.-X.; Chen, S.-C., Factors Affecting Particle Depositions on Electret Filters Used in Residential HVAC Systems and Indoor Air Cleaners. *Aerosol and Air Quality Research* **2018,** *18* (12), 3211-3219.
41. Johnston, F. H.; Borchers-Arriagada, N.; Morgan, G. G.; Jalaludin, B.; Palmer, A. J.; Williamson, G. J.; Bowman, D. M. J. S., Unprecedented health costs of smoke-related PM2.5 from the 2019–20 Australian megafires. *Nature Sustainability* **2020**.
42. Yue, H.; He, C.; Huang, Q.; Yin, D.; Bryan, B. A., Stronger policy required to substantially reduce deaths from PM2.5 pollution in China. *Nat. Commun.* **2020,** *11* (1), 1462.
43. Hajizadeh, Y.; Jafari, N.; Mohammadi, A.; Momtaz, S. M.; Fanaei, F.; Abdolahnejad, A., Concentrations and mortality due to short- and long-term exposure to PM2.5 in a megacity of Iran (2014–2019). *Environmental Science and Pollution Research* **2020,** *27* (30), 38004-38014.
44. Lee, W.-J.; Liu, C.-Y.; Peng, L.-N.; Lin, C.-H.; Lin, H.-P.; Chen, L.-K., PM2.5 air pollution contributes to the burden of frailty. *Sci. Rep.* **2020,** *10* (1), 14478.
45. Zoran, M. A.; Savastru, R. S.; Savastru, D. M.; Tautan, M. N., Assessing the relationship between surface levels of PM2.5 and PM10 particulate matter impact on COVID-19 in Milan, Italy. *Sci. Total Environ.* **2020,** *738*, 139825.
46. Singh, V.; Biswal, A.; Kesarkar, A. P.; Mor, S.; Ravindra, K., High resolution vehicular PM10 emissions over megacity Delhi: Relative contributions of exhaust and non-exhaust sources. *Sci. Total Environ.* **2020,** *699*, 134273.
47. Wang, W.; Wen, C.; Liu, T.; Li, C.; Chen, L.; Wu, J.; Shao, Y.; Liu, E., Effects of various occurrence modes of inorganic components on the emissions of PM10 during torrefied biomass combustion under air and oxy-fuel conditions. *Appl. Energy* **2020,** *259*, 114153.
48. Xiao, J.; Liang, J.; Zhang, C.; Tao, Y.; Ling, G.-W.; Yang, Q.-H., Advanced Materials for Capturing Particulate Matter: Progress and Perspectives. *Small Methods* **2018,** *2* (7), 1800012.

49. Wan, H.; Wang, N.; Yang, J.; Si, Y.; Chen, K.; Ding, B.; Sun, G.; El-Newehy, M.; Al-Deyab, S. S.; Yu, J., Hierarchically structured polysulfone/titania fibrous membranes with enhanced air filtration performance. *J. Colloid Interface Sci.* **2014,** *417*, 18-26.
50. Zhu, M.; Han, J.; Wang, F.; Shao, W.; Xiong, R.; Zhang, Q.; Pan, H.; Yang, Y.; Samal, S. K.; Zhang, F.; Huang, C., Electrospun Nanofibers Membranes for Effective Air Filtration. **2017,** *302* (1), 1600353.
51. Liu, C.; Hsu, P.-C.; Lee, H.-W.; Ye, M.; Zheng, G.; Liu, N.; Li, W.; Cui, Y., Transparent air filter for high-efficiency PM2.5 capture. *Nat. Commun.* **2015,** *6* (1), 6205.
52. Wang, N.; Yang, Y.; Al-Deyab, S. S.; El-Newehy, M.; Yu, J.; Ding, B., Ultra-light 3D nanofibre-nets binary structured nylon 6–polyacrylonitrile membranes for efficient filtration of fine particulate matter. *Journal of Materials Chemistry A* **2015,** *3* (47), 23946-23954.
53. Hinds, W. C.; Hinds, W. C., *Aerosol Technology: Properties, Behavior, and Measurement of Airborne Particles*. Wiley: 1999.
54. Dai, X.; Li, X.; Wang, X., Morphology controlled porous poly(lactic acid)/zeolitic imidazolate framework-8 fibrous membranes with superior PM2.5 capture capacity. *Chem. Eng. J.* **2018,** *338*, 82-91.
55. Kao, T.-H.; Su, S.-K.; Su, C.-I.; Lee, A.-W.; Chen, J.-K., Polyacrylonitrile microscaffolds assembled from mesh structures of aligned electrospun nanofibers as high-efficiency particulate air filters. *Aerosol Sci. Technol.* **2016,** *50* (6), 615-625.
56. Leung, W. W.-F.; Hung, C.-H.; Yuen, P.-T., Effect of face velocity, nanofiber packing density and thickness on filtration performance of filters with nanofibers coated on a substrate. *Sep. Purif. Technol.* **2010,** *71* (1), 30-37.
57. Qiu, S.; Xue, M.; Zhu, G., Metal–organic framework membranes: from synthesis to separation application. *Chem. Soc. Rev.* **2014,** *43* (16), 6116-6140.
58. Wang, C.-s.; Otani, Y., Removal of Nanoparticles from Gas Streams by Fibrous Filters: A Review. *Ind. Eng. Chem. Res.* **2013,** *52* (1), 5-17.
59. Zhai, Y.; Li, X.; Wang, T.; Wang, B.; Li, C.; Zeng, G., A review on airborne microorganisms in particulate matters: Composition, characteristics and influence factors. *Environ. Int.* **2018,** *113*, 74-90.
60. Efsa Panel on Food Contact Materials, E.; Processing, A.; Silano, V.; Barat Baviera, J. M.; Bolognesi, C.; Cocconcelli, P. S.; Crebelli, R.; Gott, D. M.; Grob, K.; Lampi, E.; Mortensen, A.; Rivière, G.; Steffensen, I.-L.; Tlustos, C.; van Loveren, H.; Vernis, L.; Zorn, H.; Glandorf, B.; Herman, L.; Aguilera, J.; Andryszkiewicz, M.; Liu, Y.; Chesson, A., Safety evaluation of the food enzyme α-amylase from the genetically modified Pseudomonas fluorescens strain BD15754. *EFSA Journal* **2020,** *18* (3), e06043.
61. Falzone, L.; Gattuso, G.; Lombardo, C.; Lupo, G.; Grillo, C. M.; Spandidos, D. A.; Libra, M.; Salmeri, M., Droplet digital PCR for the detection and monitoring of Legionella pneumophila. *Int. J. Mol. Med.* **2020,** *46* (5), 1777-1782.
62. Adhikari, A.; Gupta, J.; Wilkins, J. R., III; Olds, R. L.; Indugula, R.; Cho, K. J.; Li, C.; Yermakov, M., Airborne Microorganisms, Endotoxin, and (1→3)-β-D-Glucan Exposure in Greenhouses and Assessment of Respiratory Symptoms Among Workers. *The Annals of Occupational Hygiene* **2011,** *55* (3), 272-285.
63. Nilsson, S.; Merritt, A. S.; Bellander, T., Endotoxins in urban air in Stockholm, Sweden. *Atmos. Environ.* **2011,** *45* (1), 266-270.

64. Lenart-Boroń, A.; Drab, D.; Chrobak, J., Microbiological Aerosol, Particulate Matter Concentrations and Antibiotic Resistant Staphylococcus spp. in the Premises of Poland's Oldest Agricultural School. *Atmosphere* **2021,** *12* (8).
65. Li, Y.; Zheng, Z.; Zhu, S.; Ramaswamy, H. S.; Yu, Y., Effect of Low-Temperature-High-Pressure Treatment on the Reduction of Escherichia coli in Milk. *Foods* **2020,** *9* (12).
66. Vu, T. V.; Ondracek, J.; Zdímal, V.; Schwarz, J.; Delgado-Saborit, J. M.; Harrison, R. M., Physical properties and lung deposition of particles emitted from five major indoor sources. *Air Quality, Atmosphere & Health* **2017,** *10* (1), 1-14.
67. Sutton, T. C., The Pandemic Threat of Emerging H5 and H7 Avian Influenza Viruses. *Viruses* **2018,** *10* (9).
68. Song, L.; Zhou, J.; Wang, C.; Meng, G.; Li, Y.; Jarin, M.; Wu, Z.; Xie, X., Airborne pathogenic microorganisms and air cleaning technology development: A review. *J. Hazard. Mater.* **2022,** *424*, 127429.
69. Zhiqing, L.; Yongyun, C.; Wenxiang, C.; Mengning, Y.; Yuanqing, M.; Zhenan, Z.; Haishan, W.; Jie, Z.; Kerong, D.; Huiwu, L.; Fengxiang, L.; Zanjing, Z., Surgical masks as source of bacterial contamination during operative procedures. *J Orthop Translat* **2018,** *14*, 57-62.
70. Jeong, S. B.; Ko, H. S.; Seo, S. C.; Jung, J. H., Evaluation of filtration characteristics and microbial recovery rates of commercial filtering facepiece respirators against airborne bacterial particles. *Sci. Total Environ.* **2019,** *682*, 729-736.
71. Howarth, A. J.; Peters, A. W.; Vermeulen, N. A.; Wang, T. C.; Hupp, J. T.; Farha, O. K., Best Practices for the Synthesis, Activation, and Characterization of Metal–Organic Frameworks. *Chem. Mater.* **2017,** *29* (1), 26-39.
72. Kang, X.; Zhu, M., Tailoring the photoluminescence of atomically precise nanoclusters. *Chem. Soc. Rev.* **2019,** *48* (8), 2422-2457.
73. Lustig, W. P.; Mukherjee, S.; Rudd, N. D.; Desai, A. V.; Li, J.; Ghosh, S. K., Metal–organic frameworks: functional luminescent and photonic materials for sensing applications. *Chem. Soc. Rev.* **2017,** *46* (11), 3242-3285.
74. Schneemann, A.; Bon, V.; Schwedler, I.; Senkovska, I.; Kaskel, S.; Fischer, R. A., Flexible metal–organic frameworks. *Chem. Soc. Rev.* **2014,** *43* (16), 6062-6096.
75. Zhu, Q.-L.; Xu, Q., Metal–organic framework composites. *Chem. Soc. Rev.* **2014,** *43* (16), 5468-5512.
76. Li, Y.-z.; Fu, Z.-h.; Xu, G., Metal-organic framework nanosheets: Preparation and applications. *Coord. Chem. Rev.* **2019,** *388*, 79-106.
77. Moghadam, P. Z.; Li, A.; Wiggin, S. B.; Tao, A.; Maloney, A. G. P.; Wood, P. A.; Ward, S. C.; Fairen-Jimenez, D., Development of a Cambridge Structural Database Subset: A Collection of Metal–Organic Frameworks for Past, Present, and Future. *Chem. Mater.* **2017,** *29* (7), 2618-2625.
78. Stoeck, U.; Krause, S.; Bon, V.; Senkovska, I.; Kaskel, S., A highly porous metal–organic framework, constructed from a cuboctahedral super-molecular building block, with exceptionally high methane uptake. *Chem. Commun.* **2012,** *48* (88), 10841-10843.
79. Zhang, Y.; He, X.; Zhu, Z.; Wang, W.-N.; Chen, S.-C., Simultaneous removal of VOCs and PM2.5 by metal-organic framework coated electret filter media. *J. Membr. Sci.* **2021,** *618*, 118629.

80. He, Y.; Wang, Z.; Wang, H.; Wang, Z.; Zeng, G.; Xu, P.; Huang, D.; Chen, M.; Song, B.; Qin, H.; Zhao, Y., Metal-organic framework-derived nanomaterials in environment related fields: Fundamentals, properties and applications. *Coord. Chem. Rev.* **2021,** *429*, 213618.
81. He, X.; Chen, D.-R.; Wang, W.-N., Bimetallic Metal-Organic Frameworks (MOFs) Synthesized Using the Spray Method for Tunable CO2 Adsorption. *Chem. Eng. J.* **2019**, 122825.
82. Zhang, W.; Hu, Y.; Ge, J.; Jiang, H.-L.; Yu, S.-H., A Facile and General Coating Approach to Moisture/Water-Resistant Metal–Organic Frameworks with Intact Porosity. *J. Am. Chem. Soc.* **2014,** *136* (49), 16978-16981.
83. Zhu, Z.; He, X.; Wang, W.-N., Unraveling the origin of the "Turn-On" effect of Al-MIL-53-NO2 during H2S detection. *CrystEngComm* **2020,** *22* (2), 195-204.
84. Nandi, S.; Banesh, S.; Trivedi, V.; Biswas, S., A dinitro-functionalized metal–organic framework featuring visual and fluorogenic sensing of H2S in living cells, human blood plasma and environmental samples. *Analyst* **2018,** *143* (6), 1482-1491.
85. Lin, G.; Meng, W.; Dapeng, C., A Novel Zr-MOF as Fluorescence Turn-On Probe for Real-Time Detecting H2S Gas and Fingerprint Identification. *Small* **2018,** *14* (17), 1703822.
86. Kumar, N.; Bhalla, V.; Kumar, M., Recent developments of fluorescent probes for the detection of gasotransmitters (NO, CO and H2S). *Coord. Chem. Rev.* **2013,** *257* (15), 2335-2347.
87. Ma, Y.; Li, X.; Li, A.; Yang, P.; Zhang, C.; Tang, B., H2S-Activable MOF Nanoparticle Photosensitizer for Effective Photodynamic Therapy against Cancer with Controllable Singlet-Oxygen Release. *Angewandte Chemie International Edition* **2017,** *56* (44), 13752-13756.
88. Yan, B., Photofunctional MOF-based hybrid materials for the chemical sensing of biomarkers. *Journal of Materials Chemistry C* **2019,** *7* (27), 8155-8175.
89. Duan, X.; Lv, R.; Shi, Z.; Wang, C.; Li, H.; Ge, J.; Ji, Z.; Yang, Y.; Li, B.; Qian, G., A new metal-organic framework with suitable pore size and ttd-type topology revealing highly selective adsorption and separation of organic dyes. *J. Solid State Chem.* **2019,** *277*, 159-162.
90. Shayegan, H.; Farahani, Y. D.; Safarifard, V., A pillar-layer metal-organic framework as a turn-on luminescent sensor for highly selective and sensitive detection of Zn(II) ion. *J. Solid State Chem.* **2019,** *279*, 120968.
91. Jiang, J.; Lu, Y.; Liu, J.; Zhou, Y.; Zhao, D.; Li, C., An acid-base resistant Zn-based metal-organic framework as a luminescent sensor for mercury(II). *J. Solid State Chem.* **2020,** *283*, 121153.
92. Zheng, X.; Fan, R.; Song, Y.; Wang, A.; Xing, K.; Du, X.; Wang, P.; Yang, Y., A highly sensitive turn-on ratiometric luminescent probe based on postsynthetic modification of Tb3+@Cu-MOF for H2S detection. *Journal of Materials Chemistry C* **2017,** *5* (38), 9943-9951.
93. Yan, Y.; Yu, H.; Zhang, Y.; Zhang, K.; Zhu, H.; Yu, T.; Jiang, H.; Wang, S., Molecularly Engineered Quantum Dots for Visualization of Hydrogen Sulfide. *ACS Appl. Mater. Interfaces* **2015,** *7* (6), 3547-3553.
94. Li, S.; Feng, J.; Huang, P.; Wu, F., Cu2+-Mediated turn-on fluorescence assay for sulfide ions using glutathione-protected gold nanoclusters: enhanced sensitivity, good reusability, and cell imaging. *New J. Chem.* **2017,** *41* (21), 12930-12936.
95. Zhang, Y.; Yuan, S.; Day, G.; Wang, X.; Yang, X.; Zhou, H.-C., Luminescent sensors based on metal-organic frameworks. *Coord. Chem. Rev.* **2018,** *354*, 28-45.
96. Cui, Y.; Zhang, J.; He, H.; Qian, G., Photonic functional metal–organic frameworks. *Chem. Soc. Rev.* **2018,** *47* (15), 5740-5785.

97. Zhao, J.; Wang, Y.-N.; Dong, W.-W.; Wu, Y.-P.; Li, D.-S.; Zhang, Q.-C., A Robust Luminescent Tb(III)-MOF with Lewis Basic Pyridyl Sites for the Highly Sensitive Detection of Metal Ions and Small Molecules. *Inorg. Chem.* **2016,** *55* (7), 3265-3271.
98. Qin, Z.-S.; Dong, W.-W.; Zhao, J.; Wu, Y.-P.; Zhang, Q.; Li, D.-S., A water-stable Tb(iii)-based metal–organic gel (MOG) for detection of antibiotics and explosives. *Inorganic Chemistry Frontiers* **2018,** *5* (1), 120-126.
99. Nandi, S.; Reinsch, H.; Banesh, S.; Stock, N.; Trivedi, V.; Biswas, S., Rapid and highly sensitive detection of extracellular and intracellular H2S by an azide-functionalized Al(iii)-based metal-organic framework. *Dalton Trans.* **2017,** *46* (38), 12856-12864.
100. Zhang, X.; Fang, L.; Jiang, K.; He, H.; Yang, Y.; Cui, Y.; Li, B.; Qian, G., Nanoscale fluorescent metal–organic framework composites as a logic platform for potential diagnosis of asthma. *Biosens. Bioelectron.* **2019,** *130*, 65-72.
101. Depauw, H.; Nevjestić, I.; De Winne, J.; Wang, G.; Haustraete, K.; Leus, K.; Verberckmoes, A.; Detavernier, C.; Callens, F.; De Canck, E.; Vrielinck, H.; Van Der Voort, P., Microwave induced "egg yolk" structure in Cr/V-MIL-53. *Chem. Commun.* **2017,** *53* (60), 8478-8481.
102. Nouar, F.; Devic, T.; Chevreau, H.; Guillou, N.; Gibson, E.; Clet, G.; Daturi, M.; Vimont, A.; Grenèche, J. M.; Breeze, M. I.; Walton, R. I.; Llewellyn, P. L.; Serre, C., Tuning the breathing behaviour of MIL-53 by cation mixing. *Chem. Commun.* **2012,** *48* (82), 10237-10239.
103. Xu, S.; Ni, Y., NH2-MIL-53(Al) nanocrystals: a fluorescent probe for the fast detection of aromatic nitro-compounds and ions in aqueous systems. *Analyst* **2019,** *144* (5), 1687-1695.
104. Zhao, D.; Liu, X.-H.; Zhao, Y.; Wang, P.; Liu, Y.; Azam, M.; Al-Resayes, S. I.; Lu, Y.; Sun, W.-Y., Luminescent Cd(ii)–organic frameworks with chelating NH2 sites for selective detection of Fe(iii) and antibiotics. *Journal of Materials Chemistry A* **2017,** *5* (30), 15797-15807.
105. Yang, C.-X.; Ren, H.-B.; Yan, X.-P., Fluorescent Metal–Organic Framework MIL-53(Al) for Highly Selective and Sensitive Detection of Fe3+ in Aqueous Solution. *Analytical Chemistry* **2013,** *85* (15), 7441-7446.
106. Zhang, D.; Guan, Y.; Hensen, E. J. M.; Xue, T.; Wang, Y., Tuning the hydrogenation activity of Pd NPs on Al–MIL-53 by linker modification. *Catalysis Science & Technology* **2014,** *4* (3), 795-802.
107. Devic, T.; Horcajada, P.; Serre, C.; Salles, F.; Maurin, G.; Moulin, B.; Heurtaux, D.; Clet, G.; Vimont, A.; Grenèche, J.-M.; Ouay, B. L.; Moreau, F.; Magnier, E.; Filinchuk, Y.; Marrot, J.; Lavalley, J.-C.; Daturi, M.; Férey, G., Functionalization in Flexible Porous Solids: Effects on the Pore Opening and the Host−Guest Interactions. *J. Am. Chem. Soc.* **2010,** *132* (3), 1127-1136.
108. Hartle, M. D.; Pluth, M. D., A practical guide to working with H2S at the interface of chemistry and biology. *Chemical Society Reviews* **2016,** *45* (22), 6108-6117.
109. Ahnfeldt, T.; Gunzelmann, D.; Loiseau, T.; Hirsemann, D.; Senker, J.; Férey, G.; Stock, N., Synthesis and Modification of a Functionalized 3D Open-Framework Structure with MIL-53 Topology. *Inorg. Chem.* **2009,** *48* (7), 3057-3064.
110. Osadchii, D. Y.; Olivos-Suarez, A. I.; Szécsényi, Á.; Li, G.; Nasalevich, M. A.; Dugulan, I. A.; Crespo, P. S.; Hensen, E. J. M.; Veber, S. L.; Fedin, M. V.; Sankar, G.; Pidko, E. A.; Gascon, J., Isolated Fe Sites in Metal Organic Frameworks Catalyze the Direct Conversion of Methane to Methanol. *ACS Catalysis* **2018,** *8* (6), 5542-5548.

111. Han, Y.; Zhai, J.; Zhang, L.; Dong, S., Direct carbonization of cobalt-doped NH2-MIL-53(Fe) for electrocatalysis of oxygen evolution reaction. *Nanoscale* **2016,** *8* (2), 1033-1039.
112. Slater, J. C., Atomic Radii in Crystals. *The Journal of Chemical Physics* **1964,** *41* (10), 3199-3204.
113. Zhang, Y.-y.; Liu, Q.; Yang, C.; Wu, S.-c.; Cheng, J.-h., Magnetic aluminum-based metal organic framework as a novel magnetic adsorbent for the effective removal of minocycline from aqueous solutions. *Environ. Pollut.* **2019**, 113226.
114. Moran, C. M.; Joshi, J. N.; Marti, R. M.; Hayes, S. E.; Walton, K. S., Structured Growth of Metal–Organic Framework MIL-53(Al) from Solid Aluminum Carbide Precursor. *J. Am. Chem. Soc.* **2018,** *140* (29), 9148-9153.
115. Guo, W.; Sun, W.; Lv, L.-P.; Kong, S.; Wang, Y., Microwave-Assisted Morphology Evolution of Fe-Based Metal–Organic Frameworks and Their Derived Fe2O3 Nanostructures for Li-Ion Storage. *ACS Nano* **2017,** *11* (4), 4198-4205.
116. Shen, L.; Liang, S.; Wu, W.; Liang, R.; Wu, L., Multifunctional NH2-mediated zirconium metal–organic framework as an efficient visible-light-driven photocatalyst for selective oxidation of alcohols and reduction of aqueous Cr(vi). *Dalton Trans.* **2013,** *42* (37), 13649-13657.
117. Bordiga, S.; Lamberti, C.; Ricchiardi, G.; Regli, L.; Bonino, F.; Damin, A.; Lillerud, K. P.; Bjorgen, M.; Zecchina, A., Electronic and vibrational properties of a MOF-5 metal–organic framework: ZnO quantum dot behaviour. *Chem. Commun.* **2004,** (20), 2300-2301.
118. Vuong, G.-T.; Pham, M.-H.; Do, T.-O., Direct synthesis and mechanism of the formation of mixed metal Fe2Ni-MIL-88B. *CrystEngComm* **2013,** *15* (45), 9694-9703.
119. Vuong, G.-T.; Pham, M.-H.; Do, T.-O., Synthesis and engineering porosity of a mixed metal Fe2Ni MIL-88B metal–organic framework. *Dalton Trans.* **2013,** *42* (2), 550-557.
120. Yu, H.; Liu, C.; Li, Y.; Huang, A., Functionalized Metal–Organic Framework UiO-66-NH-BQB for Selective Detection of Hydrogen Sulfide and Cysteine. *ACS Appl. Mater. Interfaces* **2019,** *11* (45), 41972-41978.
121. Zhan, Y.; Shen, L.; Xu, C.; Zhao, W.; Cao, Y.; Jiang, L., MOF-derived porous Fe2O3 with controllable shapes and improved catalytic activities in H2S selective oxidation. *CrystEngComm* **2018,** *20* (25), 3449-3454.
122. Liu, C.; Pan, J.; Li, S.; Zhao, Y.; Wu, L. Y.; Berkman, C. E.; Whorton, A. R.; Xian, M., Capture and Visualization of Hydrogen Sulfide by a Fluorescent Probe. **2011,** *50* (44), 10327-10329.
123. Mao, G.-J.; Wei, T.-T.; Wang, X.-X.; Huan, S.-y.; Lu, D.-Q.; Zhang, J.; Zhang, X.-B.; Tan, W.; Shen, G.-L.; Yu, R.-Q., High-Sensitivity Naphthalene-Based Two-Photon Fluorescent Probe Suitable for Direct Bioimaging of H2S in Living Cells. *Anal. Chem.* **2013,** *85* (16), 7875-7881.
124. Qian, Y.; Karpus, J.; Kabil, O.; Zhang, S.-Y.; Zhu, H.-L.; Banerjee, R.; Zhao, J.; He, C., Selective fluorescent probes for live-cell monitoring of sulphide. *Nat. Commun.* **2011,** *2*, 495.
125. Bae, S. K.; Heo, C. H.; Choi, D. J.; Sen, D.; Joe, E.-H.; Cho, B. R.; Kim, H. M., A Ratiometric Two-Photon Fluorescent Probe Reveals Reduction in Mitochondrial H2S Production in Parkinson's Disease Gene Knockout Astrocytes. *J. Am. Chem. Soc.* **2013,** *135* (26), 9915-9923.
126. Yaghi, O. M.; O'Keeffe, M.; Ockwig, N. W.; Chae, H. K.; Eddaoudi, M.; Kim, J., Reticular synthesis and the design of new materials. *Nature* **2003,** *423* (6941), 705-714.

127. Tian, T.; Zeng, Z.; Vulpe, D.; Casco, M. E.; Divitini, G.; Midgley, P. A.; Silvestre-Albero, J.; Tan, J.-C.; Moghadam, P. Z.; Fairen-Jimenez, D., A sol–gel monolithic metal–organic framework with enhanced methane uptake. *Nat. Mater.* **2017,** *17*, 174.
128. Wang, H.; Dong, X.; Velasco, E.; Olson, D. H.; Han, Y.; Li, J., One-of-a-kind: a microporous metal–organic framework capable of adsorptive separation of linear, mono- and di-branched alkane isomers via temperature- and adsorbate-dependent molecular sieving. *Energy Environ. Sci.* **2018,** *11* (5), 1226-1231.
129. Xu, X.-Y.; Lian, X.; Hao, J.-N.; Zhang, C.; Yan, B., A Double-Stimuli-Responsive Fluorescent Center for Monitoring of Food Spoilage based on Dye Covalently Modified EuMOFs: From Sensory Hydrogels to Logic Devices. **2017,** *29* (37), 1702298.
130. Abánades Lázaro, I.; Forgan, R. S., Application of zirconium MOFs in drug delivery and biomedicine. *Coord. Chem. Rev.* **2019,** *380*, 230-259.
131. Nagarkar, S. S.; Saha, T.; Desai, A. V.; Talukdar, P.; Ghosh, S. K., Metal-organic framework based highly selective fluorescence turn-on probe for hydrogen sulphide. *Sci. Rep.* **2014,** *4*, 7053.
132. Buragohain, A.; Biswas, S., Cerium-based azide- and nitro-functionalized UiO-66 frameworks as turn-on fluorescent probes for the sensing of hydrogen sulphide. *CrystEngComm* **2016,** *18* (23), 4374-4381.
133. Cao, Y.-Y.; Guo, X.-F.; Wang, H., High sensitive luminescence metal-organic framework sensor for hydrogen sulfide in aqueous solution: A trial of novel turn-on mechanism. *Sensors and Actuators B: Chemical* **2017,** *243*, 8-13.
134. Dalapati, R.; Balaji, S. N.; Trivedi, V.; Khamari, L.; Biswas, S., A dinitro-functionalized Zr(IV)-based metal-organic framework as colorimetric and fluorogenic probe for highly selective detection of hydrogen sulphide. *Sensors and Actuators B: Chemical* **2017,** *245*, 1039-1049.
135. Li, Y.; Zhang, X.; Zhang, L.; Jiang, K.; Cui, Y.; Yang, Y.; Qian, G., A nanoscale Zr-based fluorescent metal-organic framework for selective and sensitive detection of hydrogen sulfide. *J. Solid State Chem.* **2017,** *255*, 97-101.
136. Gao, Q.; Xu, S.; Guo, C.; Chen, Y.; Wang, L., Embedding Nanocluster in MOF via Crystalline Ion-Triggered Growth Strategy for Improved Emission and Selective Sensing. *ACS Appl. Mater. Interfaces* **2018,** *10* (18), 16059-16065.
137. Wang, H.; Cui, J.; Arshad, A.; Xu, S.; Wang, L., A visual photothermal paper sensor for H2S recognition through rational modulation LSPR wavelength of plasmonics. *Science China Chemistry* **2018,** *61* (3), 368-374.
138. Zhang, X.; Zhang, Q.; Yue, D.; Zhang, J.; Wang, J.; Li, B.; Yang, Y.; Cui, Y.; Qian, G., Flexible Metal–Organic Framework-Based Mixed-Matrix Membranes: A New Platform for H2S Sensors. *Small* **2018,** *14* (37), 1801563.
139. Zheng, X.; Fan, R.; Song, Y.; Xing, K.; Wang, P.; Yang, Y., Dual-Emitting Eu(III)–Cu(II) Heterometallic–Organic Framework: Simultaneous, Selective, and Sensitive Detection of Hydrogen Sulfide and Ascorbic Acid in a Wide Range. *ACS Appl. Mater. Interfaces* **2018,** *10* (38), 32698-32706.
140. Biswas, S.; Ahnfeldt, T.; Stock, N., New Functionalized Flexible Al-MIL-53-X (X = -Cl, -Br, -CH3, -NO2, -(OH)2) Solids: Syntheses, Characterization, Sorption, and Breathing Behavior. *Inorg. Chem.* **2011,** *50* (19), 9518-9526.
141. Munn, A. S.; Pillai, R. S.; Biswas, S.; Stock, N.; Maurin, G.; Walton, R. I., The flexibility of modified-linker MIL-53 materials. *Dalton Trans.* **2016,** *45* (10), 4162-4168.

142. Walton, K. S.; Snurr, R. Q., Applicability of the BET Method for Determining Surface Areas of Microporous Metal−Organic Frameworks. *J. Am. Chem. Soc.* **2007,** *129* (27), 8552-8556.
143. Xu, T.; Jiang, Z.; He, M.; Gao, X.; He, Y., Effect of arrangement of functional groups on stability and gas adsorption properties in two regioisomeric copper bent diisophthalate frameworks. *CrystEngComm* **2019,** *21* (32), 4820-4827.
144. Yuan, S.; Feng, L.; Wang, K.; Pang, J.; Bosch, M.; Lollar, C.; Sun, Y.; Qin, J.; Yang, X.; Zhang, P.; Wang, Q.; Zou, L.; Zhang, Y.; Zhang, L.; Fang, Y.; Li, J.; Zhou, H.-C., Stable Metal–Organic Frameworks: Design, Synthesis, and Applications. **2018,** *30* (37), 1704303.
145. Zheng, X.-X.; Shen, L.-J.; Chen, X.-P.; Zheng, X.-H.; Au, C.-T.; Jiang, L.-L., Amino-Modified Fe-Terephthalate Metal–Organic Framework as an Efficient Catalyst for the Selective Oxidation of H2S. *Inorg. Chem.* **2018,** *57* (16), 10081-10089.
146. Li, W.; Li, M.; Liu, Y.; Pan, D.; Li, Z.; Wang, L.; Wu, M., Three Minute Ultrarapid Microwave-Assisted Synthesis of Bright Fluorescent Graphene Quantum Dots for Live Cell Staining and White LEDs. *ACS Applied Nano Materials* **2018,** *1* (4), 1623-1630.
147. Sienkiewicz-Gromiuk, J.; Mazur, L.; Bartyzel, A.; Rzączyńska, Z., Synthesis, Crystal Structure, Spectroscopic and Thermal Investigations of a Novel 2D Sodium(I) Coordination Polymer Based on 2-Aminoterephthalic Ligand. *J. Inorg. Organomet. Polym. Mater.* **2012,** *22* (6), 1325-1331.
148. Oliveira, G. F.; Andrade, R. C.; Fortunato, A. B.; Camargo, E. S.; De Carvalho, C. T., 2-aminoterephthalate compounds: a thermal and spectroscopic approach. *Brazilian Journal of Thermal Analysis* **2015,** *4* (3).
149. Qian, X.; Yadian, B.; Wu, R.; Long, Y.; Zhou, K.; Zhu, B.; Huang, Y., Structure stability of metal-organic framework MIL-53 (Al) in aqueous solutions. *Int. J. Hydrogen Energy* **2013,** *38* (36), 16710-16715.
150. Baldini, F. J. A.; Chemistry, B., Alexander P. Demchenko: Introduction to fluorescence sensing. **2009,** *395* (5), 1195.
151. Peleg, A. Y.; Hooper, D. C., Hospital-Acquired Infections Due to Gram-Negative Bacteria. *N. Engl. J. Med.* **2010,** *362* (19), 1804-1813.
152. Magill, S. S.; O'Leary, E.; Janelle, S. J.; Thompson, D. L.; Dumyati, G.; Nadle, J.; Wilson, L. E.; Kainer, M. A.; Lynfield, R.; Greissman, S.; Ray, S. M.; Beldavs, Z.; Gross, C.; Bamberg, W.; Sievers, M.; Concannon, C.; Buhr, N.; Warnke, L.; Maloney, M.; Ocampo, V.; Brooks, J.; Oyewumi, T.; Sharmin, S.; Richards, K.; Rainbow, J.; Samper, M.; Hancock, E. B.; Leaptrot, D.; Scalise, E.; Badrun, F.; Phelps, R.; Edwards, J. R., Changes in Prevalence of Health Care–Associated Infections in U.S. Hospitals. *N. Engl. J. Med.* **2018,** *379* (18), 1732-1744.
153. Magill, S. S.; Edwards, J. R.; Bamberg, W.; Beldavs, Z. G.; Dumyati, G.; Kainer, M. A.; Lynfield, R.; Maloney, M.; McAllister-Hollod, L.; Nadle, J.; Ray, S. M.; Thompson, D. L.; Wilson, L. E.; Fridkin, S. K., Multistate Point-Prevalence Survey of Health Care–Associated Infections. *N. Engl. J. Med.* **2014,** *370* (13), 1198-1208.
154. Stone, P. W., Economic burden of healthcare-associated infections: an American perspective. *Expert Rev. Pharmacoecon. Outcomes Res.* **2009,** *9* (5), 417-422.
155. Marchetti, A.; Rossiter, R., Economic burden of healthcare-associated infection in US acute care hospitals: societal perspective. *J. Med. Econ.* **2013,** *16* (12), 1399-1404.
156. Carter, B.; Collins, J. T.; Barlow-Pay, F.; Rickard, F.; Bruce, E.; Verduri, A.; Quinn, T. J.; Mitchell, E.; Price, A.; Vilches-Moraga, A.; Stechman, M. J.; Short, R.; Einarsson, A.;

Braude, P.; Moug, S.; Myint, P. K.; Hewitt, J.; Pearce, L.; McCarthy, K.; Collaborators, C. S., Nosocomial COVID-19 infection: examining the risk of mortality. The COPE-Nosocomial Study (COVID in Older PEople). *The Journal of hospital infection* **2020,** *106* (2), 376-384.
157. Rosenstock, L., 42 CFR Part 84: Respiratory Protective Devices Implications for Tuberculosis Protection. *Infect. Control Hosp. Epidemiol.* **1995,** *16* (9), 529-531.
158. Laboratory performance evaluation of N95 filtering facepiece respirators, 1996. *MMWR Morb. Mortal. Wkly. Rep.* **1998,** *47* (48), 1045-9.
159. Liao, L.; Xiao, W.; Zhao, M.; Yu, X.; Wang, H.; Wang, Q.; Chu, S.; Cui, Y., Can N95 Respirators Be Reused after Disinfection? How Many Times? *ACS Nano* **2020,** *14* (5), 6348-6356.
160. Zhang, G.-H.; Zhu, Q.-H.; Zhang, L.; Yong, F.; Zhang, Z.; Wang, S.-L.; Wang, Y.; He, L.; Tao, G.-H., High-performance particulate matter including nanoscale particle removal by a self-powered air filter. *Nat. Commun.* **2020,** *11* (1), 1653.
161. Zhong, H.; Zhu, Z.; You, P.; Lin, J.; Cheung, C. F.; Lu, V. L.; Yan, F.; Chan, C.-Y.; Li, G., Plasmonic and Superhydrophobic Self-Decontaminating N95 Respirators. *ACS Nano* **2020,** *14* (7), 8846-8854.
162. Bai, Y.; Han, C. B.; He, C.; Gu, G. Q.; Nie, J. H.; Shao, J. J.; Xiao, T. X.; Deng, C. R.; Wang, Z. L., Washable Multilayer Triboelectric Air Filter for Efficient Particulate Matter PM2.5 Removal. *Adv. Funct. Mater.* **2018,** *28* (15), 1706680.
163. Charvet, A.; Gonthier, Y.; Gonze, E.; Bernis, A., Experimental and modelled efficiencies during the filtration of a liquid aerosol with a fibrous medium. *Chem. Eng. Sci.* **2010,** *65* (5), 1875-1886.
164. Tebyetekerwa, M.; Xu, Z.; Yang, S.; Ramakrishna, S., Electrospun Nanofibers-Based Face Masks. *Advanced Fiber Materials* **2020,** *2* (3), 161-166.
165. Cheng, Y.; Wang, C.; Zhong, J.; Lin, S.; Xiao, Y.; Zhong, Q.; Jiang, H.; Wu, N.; Li, W.; Chen, S.; Wang, B.; Zhang, Y.; Zhou, J., Electrospun polyetherimide electret nonwoven for bi-functional smart face mask. *Nano Energy* **2017,** *34*, 562-569.
166. Barhate, R. S.; Ramakrishna, S., Nanofibrous filtering media: Filtration problems and solutions from tiny materials. *J. Membr. Sci.* **2007,** *296* (1), 1-8.
167. Ullah, S.; Ullah, A.; Lee, J.; Jeong, Y.; Hashmi, M.; Zhu, C.; Joo, K. I.; Cha, H. J.; Kim, I. S., Reusability Comparison of Melt-Blown vs Nanofiber Face Mask Filters for Use in the Coronavirus Pandemic. *ACS Applied Nano Materials* **2020,** *3* (7), 7231-7241.
168. Wang, N.; Wang, X.; Ding, B.; Yu, J.; Sun, G., Tunable fabrication of three-dimensional polyamide-66 nano-fiber/nets for high efficiency fine particulate filtration. *J. Mater. Chem.* **2012,** *22* (4), 1445-1452.
169. Zhang, Y.; Yuan, S.; Feng, X.; Li, H.; Zhou, J.; Wang, B., Preparation of Nanofibrous Metal–Organic Framework Filters for Efficient Air Pollution Control. *J. Am. Chem. Soc.* **2016,** *138* (18), 5785-5788.
170. Bian, Y.; Wang, R.; Wang, S.; Yao, C.; Ren, W.; Chen, C.; Zhang, L., Metal–organic framework-based nanofiber filters for effective indoor air quality control. *Journal of Materials Chemistry A* **2018,** *6* (32), 15807-15814.
171. Wen, M.; Li, G.; Liu, H.; Chen, J.; An, T.; Yamashita, H., Metal–organic framework-based nanomaterials for adsorption and photocatalytic degradation of gaseous pollutants: recent progress and challenges. *Environmental Science: Nano* **2019,** *6* (4), 1006-1025.

172. Feng, S.; Li, X.; Zhao, S.; Hu, Y.; Zhong, Z.; Xing, W.; Wang, H., Multifunctional metal organic framework and carbon nanotube-modified filter for combined ultrafine dust capture and SO2 dynamic adsorption. *Environmental Science: Nano* **2018,** *5* (12), 3023-3031.
173. Weinstein, R. A.; Gaynes, R.; Edwards, J. R.; System, N. N. I. S., Overview of Nosocomial Infections Caused by Gram-Negative Bacilli. *Clin. Infect. Dis.* **2005,** *41* (6), 848-854.
174. Siegel, J. D.; Rhinehart, E.; Jackson, M.; Chiarello, L., 2007 Guideline for Isolation Precautions: Preventing Transmission of Infectious Agents in Health Care Settings. *Am. J. Infect. Control* **2007,** *35* (10, Supplement 2), S65-S164.
175. Wu, M.; Ma, B.; Pan, T.; Chen, S.; Sun, J., Silver-Nanoparticle-Colored Cotton Fabrics with Tunable Colors and Durable Antibacterial and Self-Healing Superhydrophobic Properties. *Adv. Funct. Mater.* **2016,** *26* (4), 569-576.
176. Mazurkow, J. M.; Yüzbasi, N. S.; Domagala, K. W.; Pfeiffer, S.; Kata, D.; Graule, T., Nano-Sized Copper (Oxide) on Alumina Granules for Water Filtration: Effect of Copper Oxidation State on Virus Removal Performance. *Environ. Sci. Technol.* **2020,** *54* (2), 1214-1222.
177. Lv, D.; Wang, R.; Tang, G.; Mou, Z.; Lei, J.; Han, J.; De Smedt, S.; Xiong, R.; Huang, C., Ecofriendly Electrospun Membranes Loaded with Visible-Light-Responding Nanoparticles for Multifunctional Usages: Highly Efficient Air Filtration, Dye Scavenging, and Bactericidal Activity. *ACS Appl. Mater. Interfaces* **2019,** *11* (13), 12880-12889.
178. Tong, W.; Xiong, Y.; Duan, S.; Ding, X.; Xu, F.-J., Phthalocyanine functionalized poly(glycidyl methacrylate) nano-assemblies for photodynamic inactivation of bacteria. *Biomaterials Science* **2019,** *7* (5), 1905-1918.
179. Roberge, R. J.; Bayer, E.; Powell, J. B.; Coca, A.; Roberge, M. R.; Benson, S. M., Effect of Exhaled Moisture on Breathing Resistance of N95 Filtering Facepiece Respirators. *The Annals of Occupational Hygiene* **2010,** *54* (6), 671-677.
180. Haider, A.; Kwak, S.; Gupta, K. C.; Kang, I.-K., Antibacterial Activity and Cytocompatibility of PLGA/CuO Hybrid Nanofiber Scaffolds Prepared by Electrospinning. *Journal of Nanomaterials* **2015,** *2015*, 832762.
181. Zhang, Y.; Zhang, X.; Zhao, Y.-Q.; Zhang, X.-Y.; Ding, X.; Ding, X.; Yu, B.; Duan, S.; Xu, F.-J., Self-adaptive antibacterial surfaces with bacterium-triggered antifouling-bactericidal switching properties. *Biomaterials Science* **2020,** *8* (3), 997-1006.
182. Sun, H.; Du, Y.; Gao, C.; Iftikhar; Long, J.; Li, S.; Shao, L., Pressure-assisted in-depth hydrophilic tailoring of porous membranes achieving high water permeability, excellent fouling resistance and superior antimicrobial ability. *J. Membr. Sci.* **2020,** *604*, 118071.
183. Ping, M.; Zhang, X.; Liu, M.; Wu, Z.; Wang, Z., Surface modification of polyvinylidene fluoride membrane by atom-transfer radical-polymerization of quaternary ammonium compound for mitigating biofouling. *J. Membr. Sci.* **2019,** *570-571*, 286-293.
184. Zander, Z. K.; Chen, P.; Hsu, Y.-H.; Dreger, N. Z.; Savariau, L.; McRoy, W. C.; Cerchiari, A. E.; Chambers, S. D.; Barton, H. A.; Becker, M. L., Post-fabrication QAC-functionalized thermoplastic polyurethane for contact-killing catheter applications. *Biomaterials* **2018,** *178*, 339-350.
185. Wilson, W. W.; Wade, M. M.; Holman, S. C.; Champlin, F. R., Status of methods for assessing bacterial cell surface charge properties based on zeta potential measurements. *J. Microbiol. Methods* **2001,** *43* (3), 153-164.

186. Jennings, M. C.; Minbiole, K. P. C.; Wuest, W. M., Quaternary Ammonium Compounds: An Antimicrobial Mainstay and Platform for Innovation to Address Bacterial Resistance. *ACS Infectious Diseases* **2015,** *1* (7), 288-303.
187. Gozzelino, G.; Lisanti, C.; Beneventi, S., Quaternary ammonium monomers for UV crosslinked antibacterial surfaces. *Colloids Surf. Physicochem. Eng. Aspects* **2013,** *430*, 21-28.
188. Jiao, Y.; Niu, L.-n.; Ma, S.; Li, J.; Tay, F. R.; Chen, J.-h., Quaternary ammonium-based biomedical materials: State-of-the-art, toxicological aspects and antimicrobial resistance. *Prog. Polym. Sci.* **2017,** *71*, 53-90.
189. Chua, M. H.; Cheng, W.; Goh, S. S.; Kong, J.; Li, B.; Lim, J. Y. C.; Mao, L.; Wang, S.; Xue, K.; Yang, L.; Ye, E.; Zhang, K.; Cheong, W. C. D.; Tan, B. H.; Li, Z.; Tan, B. H.; Loh, X. J., Face Masks in the New COVID-19 Normal: Materials, Testing, and Perspectives. *Research* **2020,** *2020*, 7286735.
190. Xie, K.; Fu, Q.; He, Y.; Kim, J.; Goh, S. J.; Nam, E.; Qiao, G. G.; Webley, P. A., Synthesis of well dispersed polymer grafted metal–organic framework nanoparticles. *Chem. Commun.* **2015,** *51* (85), 15566-15569.
191. Sun, H.; Tang, B.; Wu, P., Development of Hybrid Ultrafiltration Membranes with Improved Water Separation Properties Using Modified Superhydrophilic Metal–Organic Framework Nanoparticles. *ACS Appl. Mater. Interfaces* **2017,** *9* (25), 21473-21484.
192. Shen, L.; Liang, S.; Wu, W.; Liang, R.; Wu, L., CdS-decorated UiO–66(NH2) nanocomposites fabricated by a facile photodeposition process: an efficient and stable visible-light-driven photocatalyst for selective oxidation of alcohols. *Journal of Materials Chemistry A* **2013,** *1* (37), 11473-11482.
193. Xue, J.; Wu, T.; Dai, Y.; Xia, Y., Electrospinning and Electrospun Nanofibers: Methods, Materials, and Applications. *Chem. Rev.* **2019,** *119* (8), 5298-5415.
194. EN, ISO 21083-1:2018, Test method to measure the efficiency of air filtration media against spherical nanomaterials — Part 1: Size range from 20 nm to 500 nm, 2018.
195. NIOSH, Approval of Respiratory Protective Devices, Code of Federal Regulations Title 42, Part 84. NIOSH, Cincinnati, OH, USA. **1995,** *16* (9), 529-531.
196. Hao, W.; Xu, G.; Wang, Y., Factors influencing the filtration performance of homemade face masks. *J. Occup. Environ. Hyg.* **2021,** *18* (3), 128-138.
197. Saebo, S.; Farnell, L.; Riggs, N. V.; Radom, L., Molecular structure, rotational constants, and vibrational frequencies for ethynamine (NH2-C.tplbond.CH): a possible interstellar molecule. *J. Am. Chem. Soc.* **1984,** *106* (18), 5047-5051.
198. Tang, X.; Wei, J.; Kong, Z.; Zhang, H.; Tian, J., Introduction of amino and rGO into PP nonwoven surface for removal of gaseous aromatic pollutants and particulate matter from air. *Appl. Surf. Sci.* **2020,** *511*, 145631.
199. Greve, C.; Preketes, N. K.; Costard, R.; Koeppe, B.; Fidder, H.; Nibbering, E. T. J.; Temps, F.; Mukamel, S.; Elsaesser, T., N–H Stretching Modes of Adenosine Monomer in Solution Studied by Ultrafast Nonlinear Infrared Spectroscopy and Ab Initio Calculations. *The Journal of Physical Chemistry A* **2012,** *116* (29), 7636-7644.
200. Schaate, A.; Roy, P.; Godt, A.; Lippke, J.; Waltz, F.; Wiebcke, M.; Behrens, P., Modulated Synthesis of Zr-Based Metal–Organic Frameworks: From Nano to Single Crystals. *Chemistry – A European Journal* **2011,** *17* (24), 6643-6651.
201. Xiao, Q.; Liang, Y.; Zhu, F.; Lu, S.; Huang, S., Microwave-assisted one-pot synthesis of highly luminescent N-doped carbon dots for cellular imaging and multi-ion probing. *Microchim. Acta* **2017,** *184* (7), 2429-2438.

202. Xu, J.-W.; Wang, Y.; Yang, Y.-F.; Ye, X.-Y.; Yao, K.; Ji, J.; Xu, Z.-K., Effects of quaternization on the morphological stability and antibacterial activity of electrospun poly(DMAEMA-co-AMA) nanofibers. *Colloids Surf. B. Biointerfaces* **2015,** *133*, 148-155.
203. Fridrikh, S. V.; Yu, J. H.; Brenner, M. P.; Rutledge, G. C., Controlling the Fiber Diameter during Electrospinning. *Phys. Rev. Lett.* **2003,** *90* (14), 144502.
204. Adam, N. K., *The Physics and Chemistry of Surfaces*. Oxford University Press: 1941.
205. Wang, X.; Ding, B.; Yu, J.; Yang, J., Large-scale fabrication of two-dimensional spider-web-like gelatin nano-nets via electro-netting. *Colloids Surf. B. Biointerfaces* **2011,** *86* (2), 345-352.
206. Lowell, S.; Shields, J. E.; Thomas, M. A.; Thommes, M., *Characterization of porous solids and powders: surface area, pore size and density*. Springer Science & Business Media: 2012; Vol. 16.
207. Chang, D.-Q.; Chen, S.-C.; Pui, D. Y. H., Capture of Sub-500 nm Particles Using Residential Electret HVAC Filter Media-Experiments and Modeling. *Aerosol and Air Quality Research* **2017,** *16* (12), 3349-3357.
208. Chen, S.-C.; Wang, J.; Bahk, Y. K.; Fissan, H.; Pui, D. Y. H., Carbon Nanotube Penetration Through Fiberglass and Electret Respirator Filter and Nuclepore Filter Media: Experiments and Models. *Aerosol Sci. Technol.* **2014,** *48* (10), 997-1008.
209. Mainelis, G., Bioaerosol sampling: Classical approaches, advances, and perspectives. *Aerosol Sci. Technol.* **2020,** *54* (5), 496-519.
210. Haig, C. W.; Mackay, W. G.; Walker, J. T.; Williams, C., Bioaerosol sampling: sampling mechanisms, bioefficiency and field studies. *The Journal of hospital infection* **2016,** *93* (3), 242-255.
211. Rengasamy, S.; Shaffer, R.; Williams, B.; Smit, S., A comparison of facemask and respirator filtration test methods. *J. Occup. Environ. Hyg.* **2017,** *14* (2), 92-103.
212. Li, J.; Leavey, A.; Wang, Y.; O'Neil, C.; Wallace, M. A.; Burnham, C.-A. D.; Boon, A. C. M.; Babcock, H.; Biswas, P., Comparing the performance of 3 bioaerosol samplers for influenza virus. *J. Aerosol Sci* **2018,** *115*, 133-145.
213. Wessels, S.; Ingmer, H., Modes of action of three disinfectant active substances: A review. *Regul. Toxicol. Pharm.* **2013,** *67* (3), 456-467.
214. Kaur, R.; Liu, S., Antibacterial surface design – Contact kill. *Prog. Surf. Sci.* **2016,** *91* (3), 136-153.
215. Krieger, R., *Hayes' handbook of pesticide toxicology*. Academic press: 2010; Vol. 1.
216. Wickham, G., An investigation into the relative resistances of common bacterial pathogens to quaternary ammonium cation disinfectants. *Bioscience Horizons: The International Journal of Student Research* **2017,** *10*.
217. Koufakis, E.; Manouras, T.; Anastasiadis, S. H.; Vamvakaki, M., Film Properties and Antimicrobial Efficacy of Quaternized PDMAEMA Brushes: Short vs Long Alkyl Chain Length. *Langmuir* **2020,** *36* (13), 3482-3493.
218. Kügler, R.; Bouloussa, O.; Rondelez, F., Evidence of a charge-density threshold for optimum efficiency of biocidal cationic surfaces. *Microbiology* **2005,** *151* (5), 1341-1348.
219. Mercury, M., International programme on chemical safety. **1990,** *118*.
220. Zhou, J.; Hu, Z.; Zabihi, F.; Chen, Z.; Zhu, M., Progress and Perspective of Antiviral Protective Material. *Advanced Fiber Materials* **2020,** *2* (3), 123-139.
221. Sia, S. F.; Yan, L. M.; Chin, A. W. H.; Fung, K.; Choy, K. T.; Wong, A. Y. L.; Kaewpreedee, P.; Perera, R.; Poon, L. L. M.; Nicholls, J. M.; Peiris, M.; Yen, H. L.,

Pathogenesis and transmission of SARS-CoV-2 in golden hamsters. *Nature* **2020,** *583* (7818), 834-+.
222. Chang, S.; Pierson, E.; Koh, P. W.; Gerardin, J.; Redbird, B.; Grusky, D.; Leskovec, J., Mobility network models of COVID-19 explain inequities and inform reopening. *Nature* **2021,** *589* (7840), 82-U54.
223. Williamson, E. J.; Walker, A. J.; Bhaskaran, K.; Bacon, S.; Bates, C.; Morton, C. E.; Curtis, H. J.; Mehrkar, A.; Evans, D.; Inglesby, P.; Cockburn, J.; McDonald, H. I.; MacKenna, B.; Tomlinson, L.; Douglas, I. J.; Rentsch, C. T.; Mathur, R.; Wong, A. Y. S.; Grieve, R.; Harrison, D.; Forbes, H.; Schultze, A.; Croker, R.; Parry, J.; Hester, F.; Harper, S.; Perera, R.; Evans, S. J. W.; Smeeth, L.; Ben, G., Factors associated with COVID-19-related death using OpenSAFELY. *Nature* **2020,** *584* (7821), 430-+.
224. Murray, C. J. L.; Ikuta, K. S.; Sharara, F.; Swetschinski, L.; Robles Aguilar, G.; Gray, A.; Han, C.; Bisignano, C.; Rao, P.; Wool, E.; Johnson, S. C.; Browne, A. J.; Chipeta, M. G.; Fell, F.; Hackett, S.; Haines-Woodhouse, G.; Kashef Hamadani, B. H.; Kumaran, E. A. P.; McManigal, B.; Agarwal, R.; Akech, S.; Albertson, S.; Amuasi, J.; Andrews, J.; Aravkin, A.; Ashley, E.; Bailey, F.; Baker, S.; Basnyat, B.; Bekker, A.; Bender, R.; Bethou, A.; Bielicki, J.; Boonkasidecha, S.; Bukosia, J.; Carvalheiro, C.; Castañeda-Orjuela, C.; Chansamouth, V.; Chaurasia, S.; Chiurchiù, S.; Chowdhury, F.; Cook, A. J.; Cooper, B.; Cressey, T. R.; Criollo-Mora, E.; Cunningham, M.; Darboe, S.; Day, N. P. J.; De Luca, M.; Dokova, K.; Dramowski, A.; Dunachie, S. J.; Eckmanns, T.; Eibach, D.; Emami, A.; Feasey, N.; Fisher-Pearson, N.; Forrest, K.; Garrett, D.; Gastmeier, P.; Giref, A. Z.; Greer, R. C.; Gupta, V.; Haller, S.; Haselbeck, A.; Hay, S. I.; Holm, M.; Hopkins, S.; Iregbu, K. C.; Jacobs, J.; Jarovsky, D.; Javanmardi, F.; Khorana, M.; Kissoon, N.; Kobeissi, E.; Kostyanev, T.; Krapp, F.; Krumkamp, R.; Kumar, A.; Kyu, H. H.; Lim, C.; Limmathurotsakul, D.; Loftus, M. J.; Lunn, M.; Ma, J.; Mturi, N.; Munera-Huertas, T.; Musicha, P.; Mussi-Pinhata, M. M.; Nakamura, T.; Nanavati, R.; Nangia, S.; Newton, P.; Ngoun, C.; Novotney, A.; Nwakanma, D.; Obiero, C. W.; Olivas-Martinez, A.; Olliaro, P.; Ooko, E.; Ortiz-Brizuela, E.; Peleg, A. Y.; Perrone, C.; Plakkal, N.; Ponce-de-Leon, A.; Raad, M.; Ramdin, T.; Riddell, A.; Roberts, T.; Robotham, J. V.; Roca, A.; Rudd, K. E.; Russell, N.; Schnall, J.; Scott, J. A. G.; Shivamallappa, M.; Sifuentes-Osornio, J.; Steenkeste, N.; Stewardson, A. J.; Stoeva, T.; Tasak, N.; Thaiprakong, A.; Thwaites, G.; Turner, C.; Turner, P.; van Doorn, H. R.; Velaphi, S.; Vongpradith, A.; Vu, H.; Walsh, T.; Waner, S.; Wangrangsimakul, T.; Wozniak, T.; Zheng, P.; Sartorius, B.; Lopez, A. D.; Stergachis, A.; Moore, C.; Dolecek, C.; Naghavi, M., Global burden of bacterial antimicrobial resistance in 2019: a systematic analysis. *The Lancet* **2022,** *399* (10325), 629-655.
225. Anderson, D. J.; Chen, L. F.; Weber, D. J.; Moehring, R. W.; Lewis, S. S.; Triplett, P. F.; Blocker, M.; Becherer, P.; Schwab, J. C.; Knelson, L. P.; Lokhnygina, Y.; Rutala, W. A.; Kanamori, H.; Gergen, M. F.; Sexton, D. J., Enhanced terminal room disinfection and acquisition and infection caused by multidrug-resistant organisms and Clostridium difficile (the Benefits of Enhanced Terminal Room Disinfection study): a cluster-randomised, multicentre, crossover study. *The Lancet* **2017,** *389* (10071), 805-814.
226. Leavitt, J. W., *Typhoid Mary: captive to the public's health*. Beacon Press: 1997.
227. Pitol, A. K.; Julian, T. R., Community Transmission of SARS-CoV-2 by Surfaces: Risks and Risk Reduction Strategies. *ENVIRONMENTAL SCIENCE & TECHNOLOGY LETTERS* **2021,** *8* (3), 263-269.

228. Remington, P. L.; Hall, W. N.; Davis, I. H.; Herald, A.; Gunn, R. A., Airborne Transmission of Measles in a Physician's Office. *JAMA* **1985,** *253* (11), 1574-1577.
229. Kitagawa, H.; Nomura, T.; Nazmul, T.; Omori, K.; Shigemoto, N.; Sakaguchi, T.; Ohge, H., Effectiveness of 222-nm ultraviolet light on disinfecting SARS-CoV-2 surface contamination. *Am. J. Infect. Control* **2021,** *49* (3), 299-301.
230. Yang, Y.; Wu, X. Z.; Ma, L.; He, C.; Cao, S. J.; Long, Y. P.; Huang, J. B.; Rodriguez, R. D.; Cheng, C.; Zhao, C. S.; Qiu, L., Bioinspired Spiky Peroxidase-Mimics for Localized Bacterial Capture and Synergistic Catalytic Sterilization. *Adv. Mater.* **2021,** *33* (8).
231. Liao, L.; Xiao, W.; Zhao, M. V.; Yu, X. Z.; Wang, H. T.; Wang, Q. Q.; Chu, S.; Cui, Y., Can N95 Respirators Be Reused after Disinfection? How Many Times? *ACS Nano* **2020,** *14* (5), 6348-6356.
232. Weiss, C.; Carriere, M.; Fusco, L.; Capua, I.; Regla-Nava, J. A.; Pasquali, M.; Scott, A. A.; Vitale, F.; Unal, M. A.; Mattevi, C.; Bedognetti, D.; Merkoci, A.; Tasciotti, E.; Yilmazer, A.; Gogotsi, Y.; Stellacci, F.; Delogu, L. G., Toward Nanotechnology-Enabled Approaches against the COVID-19 Pandemic. *ACS Nano* **2020,** *14* (6), 6383-6406.
233. Teng, Z. Y.; Yang, N. L.; Lv, H. Y.; Wang, S. C.; Hu, M. Z.; Wang, C. Y.; Wang, D.; Wang, G. X., Edge-Functionalized g-C3N4 Nanosheets as a Highly Efficient Metal-free Photocatalyst for Safe Drinking Water. *CHEM* **2019,** *5* (3), 664-680.
234. Wang, W. J.; Yu, J. C.; Xia, D. H.; Wong, P. K.; Li, Y. C., Graphene and g-C3N4 Nanosheets Cowrapped Elemental alpha-Sulfur As a Novel Metal-Free Heterojunction Photocatalyst for Bacterial Inactivation under Visible-Light. *Environ. Sci. Technol.* **2013,** *47* (15), 8724-8732.
235. Kim, Y.; Coy, E.; Kim, H.; Mrowczynski, R.; Torruella, P.; Jeong, D. W.; Choi, K. S.; Jang, J. H.; Song, M. Y.; Jang, D. J.; Peiro, F.; Jurga, S.; Kim, H. J., Efficient photocatalytic production of hydrogen by exploiting the polydopamine-semiconductor interface. *APPLIED CATALYSIS B-ENVIRONMENTAL* **2021,** *280*.
236. Wang, W. J.; Zhou, C. Y.; Yang, Y.; Zeng, G. M.; Zhang, C.; Zhou, Y.; Yang, J. N.; Huang, D. L.; Wang, H.; Xiong, W. P.; Li, X. P.; Fu, Y. K.; Wang, Z. W.; He, Q. Y.; Jia, M. Y.; Luo, H. Z., Carbon nitride based photocatalysts for solar photocatalytic disinfection, can we go further? *Chem. Eng. J.* **2021,** *404*.
237. Shi, H. X.; Fan, J.; Zhao, Y. Y.; Hu, X. Y.; Zhang, X.; Tang, Z. S., Visible light driven CuBi2O4/Bi2MoO6 p-n heterojunction with enhanced photocatalytic inactivation of E. coli and mechanism insight. *J. Hazard. Mater.* **2020,** *381*.
238. Orooji, Y.; Ghanbari, M.; Amiri, O.; Salavati-Niasari, M., Facile fabrication of silver iodide/graphitic carbon nitride nanocomposites by notable photo-catalytic performance through sunlight and antimicrobial activity. *J. Hazard. Mater.* **2020,** *389*.
239. Horikoshi, S.; Serpone, N., Can the photocatalyst TiO2 be incorporated into a wastewater treatment method? Background and prospects. *Catal. Today* **2020,** *340*, 334-346.
240. Zhang, C.; Li, Y.; Shuai, D. M.; Shen, Y.; Xiong, W.; Wang, L. Q., Graphitic carbon nitride (g-C3N4)-based photocatalysts for water disinfection and microbial control: A review. *Chemosphere* **2019,** *214*, 462-479.
241. You, J. H.; Guo, Y. Z.; Guo, R.; Liu, X. W., A review of visible light-active photocatalysts for water disinfection: Features and prospects. *Chem. Eng. J.* **2019,** *373*, 624-641.
242. Zeng, X. K.; Wang, Z. Y.; Wang, G.; Gengenbach, T. R.; McCarthy, D. T.; Deletic, A.; Yu, J. G.; Zhang, X. W., Highly dispersed TiO2 nanocrystals and WO3 nanorods on reduced

graphene oxide: Z-scheme photocatalysis system for accelerated photocatalytic water disinfection. *APPLIED CATALYSIS B-ENVIRONMENTAL* **2017,** *218*, 163-173.
243. Song, J.; Kong, H.; Jang, J., Bacterial adhesion inhibition of the quaternary ammonium functionalized silica nanoparticles. *Colloids Surf. B. Biointerfaces* **2011,** *82* (2), 651-656.
244. Sharma, P.; Jha, A. B.; Dubey, R. S.; Pessarakli, M., Reactive Oxygen Species, Oxidative Damage, and Antioxidative Defense Mechanism in Plants under Stressful Conditions. *Journal of Botany* **2012,** *2012*, 217037.
245. Xu, D.; Liu, D.; Wang, B.; Chen, C.; Chen, Z.; Li, D.; Yang, Y.; Chen, H.; Kong, M. G., In Situ OH Generation from O2− and H2O2 Plays a Critical Role in Plasma-Induced Cell Death. *PLoS One* **2015,** *10* (6), e0128205.
246. Nosaka, Y.; Nosaka, A. Y., Generation and Detection of Reactive Oxygen Species in Photocatalysis. *Chem. Rev.* **2017,** *117* (17), 11302-11336.
247. Nguyen, J. V. L.; Ghafar-Zadeh, E., Biointerface Materials for Cellular Adhesion: Recent Progress and Future Prospects. *Actuators* **2020,** *9* (4).
248. Nasir, A. M.; Awang, N.; Hubadillah, S. K.; Jaafar, J.; Othman, M. H. D.; Wan Salleh, W. N.; Ismail, A. F., A review on the potential of photocatalysis in combatting SARS-CoV-2 in wastewater. *Journal of Water Process Engineering* **2021,** *42*, 102111-102111.
249. Kumar, A.; Raizada, P.; Singh, P.; Saini, R. V.; Saini, A. K.; Hosseini-Bandegharaei, A., Perspective and status of polymeric graphitic carbon nitride based Z-scheme photocatalytic systems for sustainable photocatalytic water purification. *Chem. Eng. J.* **2020,** *391*.
250. Kusiak-Nejman, E.; Morawski, A. W., TiO2/graphene-based nanocomposites for water treatment: A brief overview of charge carrier transfer, antimicrobial and photocatalytic performance. *Applied Catalysis B: Environmental* **2019,** *253*, 179-186.
251. Das, K.; Roychoudhury, A., Reactive oxygen species (ROS) and response of antioxidants as ROS-scavengers during environmental stress in plants. *Frontiers in Environmental Science* **2014,** *2*.
252. Hippeli, S.; Elstner, E. F., OH-Radical-Type Reactive Oxygen Species: A Short Review on the Mechanisms of OH-Radical-and Peroxynitrite Toxicity. *Zeitschrift für Naturforschung C* **1997,** *52* (9-10), 555-563.
253. Dufrêne, Y. F.; Persat, A., Mechanomicrobiology: how bacteria sense and respond to forces. *Nat. Rev. Microbiol.* **2020,** *18* (4), 227-240.
254. Zeng, X.; Liu, Y.; Xia, Y.; Uddin, M. H.; Xia, D.; McCarthy, D. T.; Deletic, A.; Yu, J.; Zhang, X., Cooperatively modulating reactive oxygen species generation and bacteria-photocatalyst contact over graphitic carbon nitride by polyethylenimine for rapid water disinfection. *Applied Catalysis B: Environmental* **2020,** *274*, 119095.
255. Zhu, Z.; Zhang, Y.; Bao, L.; Chen, J.; Duan, S.; Chen, S.-C.; Xu, P.; Wang, W.-N., Self-decontaminating nanofibrous filters for efficient particulate matter removal and airborne bacteria inactivation. *Environmental Science: Nano* **2021**.
256. Venkata Mohan, S.; Chiranjeevi, P.; Chandrasekhar, K.; Babu, P. S.; Sarkar, O., Chapter 11 - Acidogenic Biohydrogen Production From Wastewater. In *Biohydrogen (Second Edition)*, Pandey, A.; Mohan, S. V.; Chang, J.-S.; Hallenbeck, P. C.; Larroche, C., Eds. Elsevier: 2019; pp 279-320.
257. Cho, M.; Chung, H.; Choi, W.; Yoon, J., Linear correlation between inactivation of E. coli and OH radical concentration in TiO2 photocatalytic disinfection. *Water Res.* **2004,** *38* (4), 1069-1077.

258. Bayoudh, S.; Othmane, A.; Mora, L.; Ben Ouada, H., Assessing bacterial adhesion using DLVO and XDLVO theories and the jet impingement technique. *Colloids Surf. B. Biointerfaces* **2009,** *73* (1), 1-9.
259. Nel, A. E.; Mädler, L.; Velegol, D.; Xia, T.; Hoek, E. M. V.; Somasundaran, P.; Klaessig, F.; Castranova, V.; Thompson, M., Understanding biophysicochemical interactions at the nano–bio interface. *Nat. Mater.* **2009,** *8* (7), 543-557.
260. Wang, L.; Zhang, X.; Yu, X.; Gao, F.; Shen, Z.; Zhang, X.; Ge, S.; Liu, J.; Gu, Z.; Chen, C., An All-Organic Semiconductor C3N4/PDINH Heterostructure with Advanced Antibacterial Photocatalytic Therapy Activity. *Adv. Mater.* **2019,** *31* (33), 1901965.
261. He, X.; Nguyen, V.; Jiang, Z.; Wang, D.; Zhu, Z.; Wang, W.-N., Highly-oriented one-dimensional MOF-semiconductor nanoarrays for efficient photodegradation of antibiotics. *Catalysis Science & Technology* **2018,** *8* (8), 2117-2123.
262. Heo, K. J.; Jeong, S. B.; Shin, J.; Hwang, G. B.; Ko, H. S.; Kim, Y.; Choi, D. Y.; Jung, J. H., Water-Repellent TiO2-Organic Dye-Based Air Filters for Efficient Visible-Light-Activated Photochemical Inactivation against Bioaerosols. *Nano Lett.* **2021,** *21* (4), 1576-1583.
263. Wang, D.; Zhu, B.; He, X.; Zhu, Z.; Hutchins, G.; Xu, P.; Wang, W.-N., Iron oxide nanowire-based filter for inactivation of airborne bacteria. *Environmental Science: Nano* **2018,** *5* (5), 1096-1106.
264. Gavara, N., A beginner's guide to atomic force microscopy probing for cell mechanics. *Microsc. Res. Tech.* **2017,** *80* (1), 75-84.
265. Xiao, X.; Qian, L., Investigation of Humidity-Dependent Capillary Force. *Langmuir* **2000,** *16* (21), 8153-8158.
266. Wang, H.; Yuan, X.; Wu, Y.; Zeng, G.; Chen, X.; Leng, L.; Li, H., Synthesis and applications of novel graphitic carbon nitride/metal-organic frameworks mesoporous photocatalyst for dyes removal. *Applied Catalysis B: Environmental* **2015,** *174-175*, 445-454.
267. Ong, W.-J.; Tan, L.-L.; Ng, Y. H.; Yong, S.-T.; Chai, S.-P., Graphitic Carbon Nitride (g-C3N4)-Based Photocatalysts for Artificial Photosynthesis and Environmental Remediation: Are We a Step Closer To Achieving Sustainability? *Chem. Rev.* **2016,** *116* (12), 7159-7329.
268. Habibi-Yangjeh, A.; Asadzadeh-Khaneghah, S.; Feizpoor, S.; Rouhi, A., Review on heterogeneous photocatalytic disinfection of waterborne, airborne, and foodborne viruses: Can we win against pathogenic viruses? *J. Colloid Interface Sci.* **2020,** *580*, 503-514.
269. He, X.; Wang, W.-N., MOF-based ternary nanocomposites for better CO2 photoreduction: roles of heterojunctions and coordinatively unsaturated metal sites. *Journal of Materials Chemistry A* **2018,** *6* (3), 932-940.
270. Chen, K.; Nikam, S. P.; Zander, Z. K.; Hsu, Y.-H.; Dreger, N. Z.; Cakmak, M.; Becker, M. L., Continuous Fabrication of Antimicrobial Nanofiber Mats Using Post-Electrospinning Functionalization for Roll-to-Roll Scale-Up. *ACS Applied Polymer Materials* **2020,** *2* (2), 304-316.
271. Zhao, Y.; Cai, W.; Chen, J.; Miao, Y.; Bu, Y., A Highly Efficient Composite Catalyst Constructed From NH2-MIL-125(Ti) and Reduced Graphene Oxide for CO2 Photoreduction. *Frontiers in Chemistry* **2019,** *7*, 789.
272. He, X.; Gan, Z.; Fisenko, S.; Wang, D.; El-Kaderi, H. M.; Wang, W. N., Rapid Formation of Metal-Organic Frameworks (MOFs) Based Nanocomposites in Microdroplets and Their Applications for CO2 Photoreduction. *ACS Appl. Mater. Interfaces* **2017,** *9* (11), 9688-9698.

273. Chen, Y.; Ng, T. W.; Lu, A.; Li, Y.; Yip, H. Y.; An, T.; Li, G.; Zhao, H.; Gao, M.; Wong, P. K., Comparative study of visible-light-driven photocatalytic inactivation of two different wastewater bacteria by natural sphalerite. *Chem. Eng. J.* **2013,** *234*, 43-48.
274. Kraut, E. A.; Grant, R. W.; Waldrop, J. R.; Kowalczyk, S. P., Precise Determination of the Valence-Band Edge in X-Ray Photoemission Spectra: Application to Measurement of Semiconductor Interface Potentials. *Phys. Rev. Lett.* **1980,** *44* (24), 1620-1623.
275. Liga, M. V.; Maguire-Boyle, S. J.; Jafry, H. R.; Barron, A. R.; Li, Q., Silica Decorated TiO2 for Virus Inactivation in Drinking Water – Simple Synthesis Method and Mechanisms of Enhanced Inactivation Kinetics. *Environ. Sci. Technol.* **2013,** *47* (12), 6463-6470.
276. Carcamo-Noriega Edson, N.; Sathyamoorthi, S.; Banerjee, S.; Gnanamani, E.; Mendoza-Trujillo, M.; Mata-Espinosa, D.; Hernández-Pando, R.; Veytia-Bucheli José, I.; Possani Lourival, D.; Zare Richard, N., 1,4-Benzoquinone antimicrobial agents against Staphylococcus aureus and Mycobacterium tuberculosis derived from scorpion venom. *Proceedings of the National Academy of Sciences* **2019,** *116* (26), 12642-12647.
277. Yan, S. C.; Li, Z. S.; Zou, Z. G., Photodegradation of Rhodamine B and Methyl Orange over Boron-Doped g-C3N4 under Visible Light Irradiation. *Langmuir* **2010,** *26* (6), 3894-3901.
278. Sun, Y.; Li, C.; Xu, Y.; Bai, H.; Yao, Z.; Shi, G., Chemically converted graphene as substrate for immobilizing and enhancing the activity of a polymeric catalyst. *Chem. Commun.* **2010,** *46* (26), 4740-4742.
279. Pate, K.; Safier, P., 12 - Chemical metrology methods for CMP quality. In *Advances in Chemical Mechanical Planarization (CMP)*, Babu, S., Ed. Woodhead Publishing: 2016; pp 299-325.
280. Amrein, M. W.; Stamov, D., Atomic Force Microscopy in the Life Sciences. In *Springer Handbook of Microscopy*, Hawkes, P. W.; Spence, J. C. H., Eds. Springer International Publishing: Cham, 2019; pp 1469-1505.
281. Dorobantu, L. S.; Bhattacharjee, S.; Foght, J. M.; Gray, M. R., Analysis of Force Interactions between AFM Tips and Hydrophobic Bacteria Using DLVO Theory. *Langmuir* **2009,** *25* (12), 6968-6976.
282. Sainis, S. K.; Merrill, J. W.; Dufresne, E. R., Electrostatic Interactions of Colloidal Particles at Vanishing Ionic Strength. *Langmuir* **2008,** *24* (23), 13334-13337.
283. Liu, D.; Johnson, P. R.; Elimelech, M., Colloid Deposition Dynamics in Flow-Through Porous Media: Role of Electrolyte Concentration. *Environ. Sci. Technol.* **1995,** *29* (12), 2963-2973.
284. Asri, L. A. T. W.; Crismaru, M.; Roest, S.; Chen, Y.; Ivashenko, O.; Rudolf, P.; Tiller, J. C.; van der Mei, H. C.; Loontjens, T. J. A.; Busscher, H. J., A Shape-Adaptive, Antibacterial-Coating of Immobilized Quaternary-Ammonium Compounds Tethered on Hyperbranched Polyurea and its Mechanism of Action. *Adv. Funct. Mater.* **2014,** *24* (3), 346-355.
285. Hoogenboom, B. W., AFM in Liquids. In *Encyclopedia of Nanotechnology*, Bhushan, B., Ed. Springer Netherlands: Dordrecht, 2012; pp 83-89.
286. Romero-Vargas Castrillón, S.; Perreault, F.; de Faria, A. F.; Elimelech, M., Interaction of Graphene Oxide with Bacterial Cell Membranes: Insights from Force Spectroscopy. *Environmental Science & Technology Letters* **2015,** *2* (4), 112-117.